UNIVERSITY OF LIVERPOOL

GAMBE

GAMma Blind neutron Efficient detector

Thesis submitted in accordance with the requirements of
the University of Liverpool for the degree of Doctor in Philosophy
by

Ahmed Ahmed

July 2018

Acknowledgments

First of all, my greatest gratitude to **ALLAH**, who supports us over the whole aspects of the life. Then I would like to take this opportunity to thank everyone who has supported me throughout my PhD.

A great big thanks and my sincere gratitude go to my supervisors **Dr Harm van Zalinge**, **Dr Sergey Burdin** and **Prof Gianluigi Casse** for giving me the encouragement, motivation, immense knowledge and support needed to do and finish this work. Their guidance helped me in all the time of research and writing of this thesis. I could not have imagined having better advisers and mentors for my PhD study than them. I am also grateful for the help I received from **Sam Powell, Joe Rees** and **Stephen Chappell** with my timing measurements. In particular, I would also like to thank **Dr Andy Boston** for helping me during the first year of this research. My sincere thanks also go to the **University of Liverpool**, which gave me the opportunity to join a wide range of researcher community and giving me the access to the laboratory and research facilities.

I have enjoyed working and living in Liverpool for the last three years. So, I would like to thank **Kevin Tree, Otobong Thomas, Will Turner, Christopher Barry, Karlis Dreimanis, Adam Roberts and David Igwesi** in the department of physics who have made it a great three years.

Finally, I must thank **my parents and my family** for their continued support in everything that I do. Especially, **my wife** for everything that she has done for me and the support, which she gives to me in my life in general. This thesis is dedicated to her.

Scientific contributions

Conferences

- SPIE Optical Engineering and Applications, 2016, San Diego, California, United States. GAMBE: multipurpose sandwich detector for neutrons and photons. Proceedings Volume 9969, Radiation Detectors: Systems and Applications XVII; 99690E (2016); doi: 10.1117/12.2236752.
- 27th International Conference on Nuclear Tracks and Radiation Measurements Strasbourg, August 28th to September 1st, 2017. GAMBE: thermal neutron detection system based on a sandwich configuration of silicon semiconductor detector coupled with neutron reactive material.
- The 2017 Nuclear Science Symposium and Medical Imaging Conference, 24th Symposium on Room-Temperature X- and Gamma-Ray Detectors, Hyatt Regency in Atlanta, Georgia, from October 21st to October 28th. GAMBE: Thermal Neutron Detector for Directional Measurement of Neutron Flux.

Publication under review

- Radiation Measurements (RADMEAS-2018-107, Research paper). GAMBE: Thermal Neutron Detection System Based on a Sandwich Configuration of Silicon Semiconductor Detector Coupled with Neutron Reactive Material.
- Nuclear Instruments & Methods in Physics Research: Section A. Development of a gamma-blind neutron-efficient detector (GAMBE) as a handheld thermal neutron detector using stacked silicon sensors coated with ^{6}LiF films.

Contents

List of Figures

List of Tables

Abstract

Thermal neutron detectors, which are based on semiconductor material such as silicon coated with neutron reactive material like ^{10}B and ^{6}Li have been discussed for many decades. The performance of the thermal neutron detector system, GAMBE, which is based on two silicon sensors in a sandwich configuration is investigated. The results show that a single sandwich design with ^{6}LiF film of (1.5 ± 0.6) mg/cm^2 thick can achieve a total (ε_{tn}) and a coincidence (ε_{cn}) detection efficiency of 4% and ∼1% respectively. While, ^{6}Li foil of (40 ± 10) μm thick is able to attain a (ε_{cn}) of (1.5 ± 0.9)% and a (ε_{tn}) of (9.2 ± 1.4)%. The coincidence that defines a true neutron hit is the simultaneous signal recorded by the two sensors facing the conversion layer. These coincidences provide a very good method for rejecting spurious hits coming from gamma-rays, which are usually present in the neutron field under measurement. This methodology results in a high gamma-ray rejection factor of 10^8. However, the price to pay is a reduction of the detection efficiency of the single sandwich detector. The thermal neutron detection efficiency of the detector is enhanced by using a stacked detector configuration and high-density polyethylene (HDPE) sheets, as neutron moderators and reflectors. The GAMBE detector is positioned inside a box of HDPE with a lead window in the direction of the neutron flux for neutron moderation and a reduction of the effect of gamma-rays on the detector. The experimental layout was modeled in MCNP4C to investigate the contribution of HDPE to the thermal neutron flux (n/s/cm^2). In this research a stack of 4 silicon semiconductor sensors with two ^{6}LiF films of an average thickness of (2.8 ± 0.6) mg/cm^2 in a configuration of two sandwiches is shown to achieve a total and a coincidence detection efficiency of (27 ± 3)% and (4 ± 1)% respectively. This represents a significant improvement compared to a single detector. The effect of these stacked detectors for the development of a handheld thermal neutron detector, using 4 coated Si detectors is shown to have a 22% efficiency. Finally, this information is used to inform the optimised design of the handheld detector. The results based on GEANT4 and MCNP4C simulations indicate that the total detection efficiency of this portable detector with a stack of 7 sandwich detectors will increase up to 52% by using an optimal thickness of a ^{6}LiF film of 17 μm (3.95 mg/cm^2). This handheld detector has a highest total detection efficiency of 69% when using a ^{6}Li foil of 36 μm thick.

***K*eywords:** Neutron detector, Semiconductor detector, Neutron detection, Neutron conversion, Neutron directional detector.

Chapter 1

Introduction

NEUTRON detection has become a prime importance in today's world owing to the huge destruction capabilities and security threats of nuclear devices [1]. In the last decade an increasing risk has arisen at world level coming from the unknown location of special nuclear material (SNM) such as plutonium (^{239}Pu), which has been used within the nuclear weapons that were fabricated in the former Soviet Union and that have not been strictly controlled since its disintegration. This type of material may be sought by terrorist groups to build a nuclear explosive device or 'dirty bombs', which are conventional explosive mixed with a radioactive source [2]. Neutron detectors can indicate the presence of these materials, since they are mainly emitters of fission neutrons. They can also be used for monitoring another type of radioactive threat, which is the loss or abandonment of equipment containing radioactive materials corresponding to nuclear waste characterisation, material safeguards, facility decontamination and decommissioning [3].

In addition, neutron detection systems are important for radiation safety, due to the neutron radiation hazard, which is associated with neutron sources, accelerators and nuclear reactors. These hazardous radiation sources require monitoring because of their biological effect, which depends on the neutron energy [4]. Therefore, neutron dosimetry continues to be an active area of research and motivates the development of detection technologies for the personal protection applications.

There are three main types of neutron detectors (see fig. 1.1), which are based on the ionisation of the detection medium. These types are gaseous detectors, semiconductors and scintillators, which are dependent on the fact that secondary radiation products ionise the sensitive volume of the detector, inducing a pulse of small charge [5]. Alternatively, neutrons are not charged particles (neutral), and thus they cannot cause direct ionisation to the detection medium by Coulomb interaction. Therefore, neutrons can be detected by means of two basic methods.

The first one is the absorption within a material, which emits charged particles or photons and the second way is the scattering with light nuclei that can release recoiled ions. The interaction cross-section for each process depends on the energy of the neutron and the material that the neutron interacts with. The reaction products can subsequently be detected by an ionisation based detector. Normally, an isotope which captures neutrons to produce secondary charged particles is used for the detection of slow neutrons. On the other hand fast neutrons are detected via protons produced by elastic scattering with the hydrogen nuclei of light material such as water or polyethylene [5].

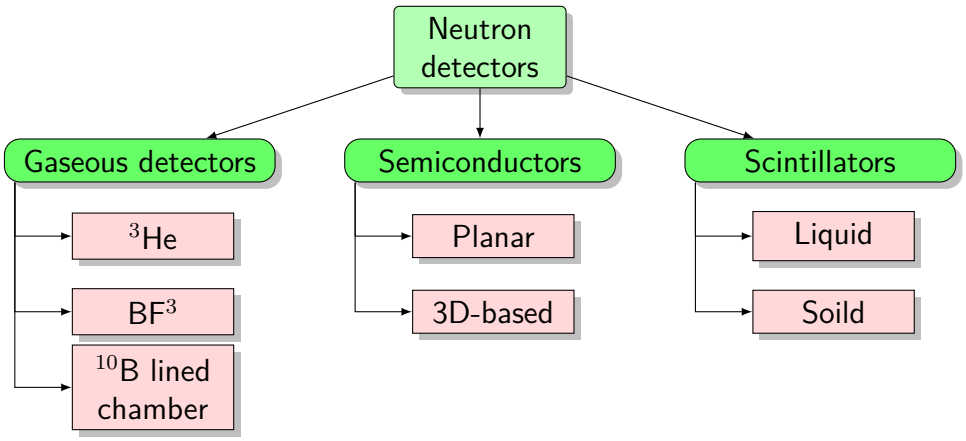

Figure 1.1: Block diagram of the most common neutron detectors. The focus of this work is the planar semiconductor neutron detector.

In the past, ^{3}He-gas filled proportional counters were most commonly used as a thermal neutron detector. They were utilised in different applications due to their high thermal neutron detection efficiency ($> 60\%$) and their low sensitivity to gamma radiation. In recent years, there is a shortage of this rare ^{3}He isotope, which exists only at about 1 ppm of natural helium. Moreover, the ^{3}He detectors operating conditions are costly, where they operate at high pressure and bias voltage. Hence, there has been a great interest in the development of alternative thermal neutron detectors. These alternative detectors should have the ability to deal with the challenge of differentiation between gamma-rays and neutron events with high thermal neutron detection efficiency in order to be considered as a replacement of ^{3}He detectors.

Solid state neutron detectors, which incorporate semiconductor materials such as silicon in their design are one of these alternative thermal neutron detectors. In contrast to ^{3}He detectors, semiconductor-based detectors offer valuable additional features, such as compactness and robustness, low weight, bias voltage, and high count rate capability [6, 7]. These favourable characteristics make them ideal for

portable systems, which depend on integrated signal acquisition and low power. Although, the high density of the semiconductor material allows a short range of the nuclear reaction products, which results in the compactness of the detector. It also increases the probability of gamma-ray interaction with the detector. Therefore, silicon is as an optimum choice for thermal neutron detection system due to the relatively low atomic number (Z = 14), which has a low probability of gamma-rays interaction with the sensitive part of the detector [8].

Finally, silicon semiconductor-based detectors must be adapted in order to be used for thermal neutron detection. They have to be coupled with a suitable neutron converter, preferably a converter whose capture products emit charged particles, that are able to reach the sensitive volume of the detector. This converter should have a high neutron absorption cross section and low atomic density, which allows a higher range of the reaction products through the converter film or foil.

1.1 Aim of research

The research aims to develop a state of the art portable silicon detector for particle physics producing high efficiency neutron detectors with low background contamination, i.e. very low rates of spurious signals. These detectors would be suitable for a wide range of applications, replacing ^{3}He detectors, and also offering significant additional capabilities.

In the present work a portable thermal neutron detector based on a single neutron conversion layer and sandwich of silicon sensors having an active area of 1×1 cm^2 is investigated. This sandwich configuration will allow the collection of reaction products emitted in opposite directions leading to a high gamma-ray rejection factor of 10^8. This high gamma rejection factor enhances the ability of this developed thermal neutron detector to be used in a high background gamma-ray field. Furthermore, this research will investigate the use of a ^{6}LiF film or a ^{6}Li foil as a neutron sensitive material, where their thicknesses are optimised to reduce the average self-absorption of the primary reaction products.

This dissertation also studies the impact of detector/moderator stacking to increase the total capability to capture neutrons and increase the detection efficiency. This contribution improves the capability of the detector to determine the direction of neutron flux from neutron source. Moreover, this stacking allows the detection of incident neutrons over a large energy range (i.e. for both thermal and fast neutrons).

Ultimately, a portable handheld thermal neutron detector has been developed in order to detect the illicit movement of radioactive material. This developed

detector is able to perform neutron measurements with a high gamma rejection factor and to determine the direction of the source of neutrons. In addition, the detection efficiency of this neutron detector has been improved using different techniques, where a high thermal neutron detection efficiency has been incrementally demanded. Hence, the detector can be used by police and fire departments, hazardous materials team, customs inspectors, border patrol agents, and for personal and site security in critical infrastructures.

1.2 Thesis layout

The thesis consists of seven Chapters. In the first Chapter, a brief introduction about the importance of neutron detection, especially for the homeland security and identification of a nuclear threat is given. In addition, this Chapter gives an overview of different types of neutron detectors and presents the goal of the study. Chapter two discusses the neutron detection concepts using different detection techniques with various neutron converter materials. The Chapter also describes the theory supporting of the research.

In order to guide the design of new thermal neutron detector, it is necessary to develop simulations optimising the parameters. Therefore, Chapter three presents two Monte Carlo simulation software packages, GEANT4 and MCNP4C, used for this study. Moreover, the simulations allow to verify the experimental results to reduce systematic errors in the measurements.

Chapter four begins by the demonstrating optimisation of using GEANT4 simulation, achieving the highest thermal neutron detection efficiency. Furthermore, a new method to suppress fake hits from gamma-rays will be introduced and discussed. The second part of Chapter four is to validate the simulation results experientially by testing the detector prototype with a single sandwich configuration in front of both neutron and gamma-ray sources.

Chapter five highlights the enhancement of the detector performance by using neutron moderators and reflectors such as high density polyethylene (HDPE) and lead. A full depiction of the neutron flux through the detector is made using MCNP4C simulations. The detection efficiency of the detector is affected due to the neutron flux variation corresponding to different experimental layouts. A novel approach is also presented in this Chapter, which describes the ability of the detector to determine the direction of neutron flux from a source of neutrons.

Another method to improve the detection efficiency of the detector by using a stacked detector of multiple layers is described in Chapter six. In this chapter, the effects of HDPE and stacking sandwich configuration detectors on the efficiency

of the GAMBE detection system is estimated. Furthermore, a new configuration of a small HDPE detector is discussed.

The final Chapter draws upon the entire thesis to suggest the optimum design of the handheld thermal neutron detector. This design can achieve a high thermal neutron detection efficiency and a high gamma-ray rejection factor. The Chapter will also summarise the main findings of this project, where the GAMBE detection system has shown to be a promising approach to neutron detection. This approach leads to the design of semiconductor based neutron detectors, which can be used not only for nuclear security purposes, but also in other physical application such as medical physics, where the accurate detection and dosimetry of neutrons is a key concern. Hence, a future study investigating the designed thermal neutron detector in the field of medical physics would be essential.

Chapter 2

Neutron detectors

2.1 Neutron characteristics

A neutron is a subatomic neutral hadronic particle, which consists of two down quarks (d), with an electric charge of -1/3, and 1 up quark (u), with charge +2/3. Neutrons and protons are the constituents of the nuclei that make up the matter by the means of a strong force. The number of protons in the nucleus is the atomic number, which defines the type of element formed by atoms, while the number of neutrons determines the isotope of this element. Neutrons were discovered by Chadwick in 1932 [9]. Since this time, they have occupied an important role in nuclear physics research.

Neutrons are classified according to their kinetic energy into relativistic, fast, slow, epithermal, thermal, cold, very cold and ultra-cold neutrons as presented in table 2.1 [10]. To simplify the situation even further, neutrons can be divided into two main groups depending on their energies. The first group is slow neutrons, which have an energy less than 0.5 eV, and the second group is fast neutrons, which have an energy higher than this value [5].

Table 2.1: Neutrons classification as a function of their kinetic energy.

Neutron type	Energy range
Relativistic	≥ 1 MeV
Fast	0.1 MeV $-$ 1 MeV
Intermediate	1 keV $-$ 0.1 MeV
Epithermal	1 eV $-$ 1 keV
Thermal	≈ 0.025 eV
Cold	$5 \times 10^{-5}-$ 0.025 eV
Very cold	$2 \times 10^{-7}- 5 \times 10^{-5}$ eV
Ultracold	$\leq 2 \times 10^{-7}$ eV

2.1.1 Neutron source

The source of neutrons used for all experiments is a 1 Ci ^{241}Am-^{9}Be neutron source. Neutrons are emitted as part of the reaction:

$$^{9}_{3}\mathrm{Be} + ^{4}_{2}\mathrm{He} \longrightarrow ^{12}_{6}\mathrm{C} + ^{1}_{0}\mathrm{n} + \gamma$$

the total neutron emission rate of a 1 Ci ^{241}Am-^{9}Be neutron source is 2.5×10^{6} neutrons per second (n/s). The reaction Be(α,n)C* will often lead to the emission of 4.43 MeV γ-rays from the excited carbon nucleus. These γ-rays are produced at a ratio of 0.6:1 γ/n [11]. Moreover, ^{241}Am is not only an α emitter but it also emits γ-rays of 26, 33 and 60 keV as a part of the following decay reaction.

$$^{241}\mathrm{Am} \longrightarrow ^{237}\mathrm{Np}^{*} + \alpha$$

$$^{237}\mathrm{Np}^{*} \longrightarrow ^{237}\mathrm{Np} + \gamma$$

In addition, 2.26 MeV γ-rays are emitted as a result of a radiative capture reaction where neutrons interact with hydrogenous moderating materials (water in this case).

$$^{1}_{0}\mathrm{n} + ^{1}_{1}\mathrm{H} \longrightarrow ^{2}_{1}\mathrm{H} + \gamma$$

Therefore, it is necessary for all experimental measurements to take into consideration the deposited energy related to γ-rays in the silicon sensors of the thermal neutron detector.

2.2 Neutron interactions

Neutrons are neutral particles and carry no charge, similar to gamma-rays. They can travel through many centimetres of matter without any interaction and, thus, can be totally unseen by a conventional detector. In addition, neutrons cannot interact with matter by means of the Coulomb force with the orbital electrons of the medium, which forms an energy loss mechanism for charged particles. Consequently, neutrons do not produce primary ionisation directly, but they can interact via nuclear forces. This means neutrons can interact with atomic nuclei by the strong nuclear force mainly via scattering, both elastic and inelastic or capture (absorption) mechanisms as presented in fig. 2.1 . The cross-section of each interaction relies on the target type and on the kinetic energy of the incident neutrons [12].

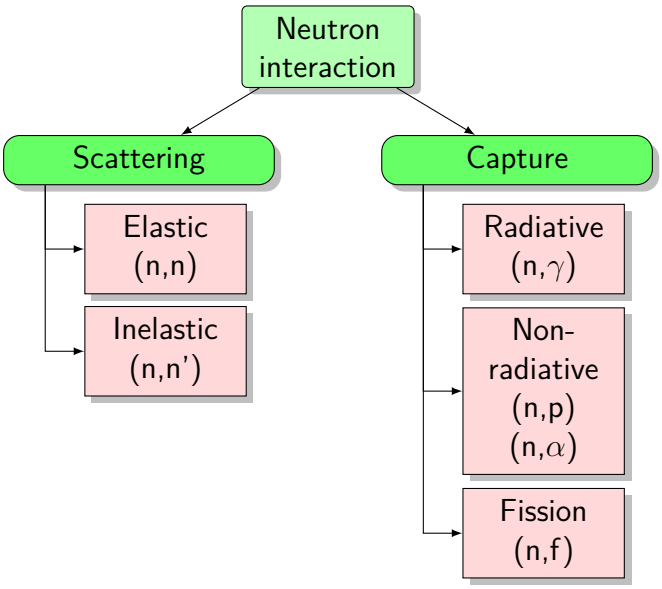

Figure 2.1: Block diagram of neutron interaction with matter.

As a result of these interactions, the neutron may either totally disappear and produce one or more secondary radiation products, or else the energy and/or direction of the neutron is changed significantly. In contrast to gamma-rays, the secondary radiation arising from neutron interactions are mainly heavy charged particles. These particles may be produced as a result of neutron-induced nuclear reactions, or they may be the nuclei of the absorbing material itself, which gained energy due to neutron collisions. Consequently, neutron detection depends on these secondary radiation products. Most of the neutron detectors utilise some type of conversion material with a large absorption cross section (σ) to convert the incident neutron into secondary charged particles, which can be detected directly using an appropriate detector [13].

2.2.1 Neutron scattering

Neutron scattering interaction involves changing the energy and/or the direction of the incident neutron, but the target nucleus remains intact with the same number of protons and neutrons. The importance of the scattering interaction will be greater, when the neutron is highly energetic. In this case, a neutron can transfer a significant amount of energy in one collision producing a recoil nucleus. This recoil nucleus is considered as a secondary radiation product, which has gained a detectable amount of energy from the neutron collision [5]. Hence, scattering/recoil mechanism is typically the only useful interaction for fast neutron detectors. The scattering interactions can be subdivided into elastic and inelastic scattering as shown in fig. 2.2.

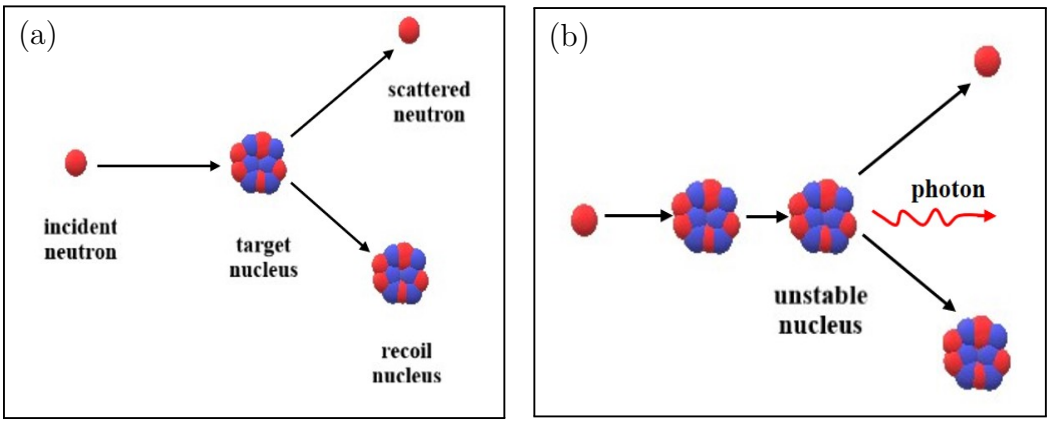

Figure 2.2: Scattering interaction of fast neutron with a nucleus of the target material, a) elastic scattering, b) inelastic scattering.

Elastic scattering is the most likely interaction between lower energy fast neutrons and low Z materials, where the total kinetic energy of the incident neutron and target nucleus is conserved. This means a neutron collides with a nucleus and transfers a part of its kinetic energy to it. The nucleus remains stable in its ground state and the neutron bounces off in a different direction as presented in fig. 2.2a. The fraction of neutron energy transferred to the stationary nucleus will depend on the mass of the recoiled nucleus and the angle through which the neutron is scattered. If the transferred energy is enough, this recoiled nucleus will have a detectable amount of energy, which could be detected directly by creating electron-hole (e-h) pairs in a semiconductor detector or by producing light in a scintillation detector [14–21]. After a sufficient number of these elastic collisions, the neutrons will effectively be in thermal equilibrium with the atoms of the scattering medium. Consequently, these neutrons are now thermal neutrons.

Inelastic scattering is a phenomenon, where a fast neutron with kinetic energy higher than 1 MeV undergoes scattering by a target nucleus of high atomic number, Z, or alternatively, it may be captured by the target nucleus to form a transient compound nucleus, which then emits a neutron of lower kinetic energy. In both cases, the target nucleus is elevated to one of its excited states during the collision, where some of the neutron kinetic energy is converted into excitation energy, which is subsequently emitted as a gamma-ray photon (see fig. 2.2b). Hence, the total kinetic energy of the outgoing neutron and nucleus is less than the kinetic energy of the incoming neutron. This is due to the fact that part of the original kinetic energy is used to place the nucleus into the excited state. However, inelastic scattering and the secondary gamma-ray have an important role in the shielding of high-energy neutrons. They are an undesired complexity in the response of most fast neutron detectors, which depend on the elastic scattering mechanism.

2.2.2 Neutron absorption (or capture)

Instead of being scattered by a nucleus, the neutron may be absorbed or captured. This is a particular interaction for slow neutrons, which are also defined as thermal neutrons with an average energy of about 0.025 eV [22]. Much of the population of these thermal neutrons will exist at this energy range due to the elastic collisions between the neutrons and the nuclei of the absorbing material prior to a neutron-induced nuclear reaction. These nuclear reactions are important in the detection of thermal neutrons, because they create the secondary radiation products (mainly charged particles) with sufficient energy, which can be detected directly. There are two categories of neutron absorption, which are radiative capture, (n,γ), and non-radiative capture such as (n, p), (n, α), (n ,t).

In the radiative capture process, the neutron is captured by the target nucleus, producing a compound nucleus in an exited state, which decays by emitting a gamma-ray. However, radiative capture is the most likely process, which can occur for a wide range of neutron energies. This type of neutron interaction is not widely applied in active neutron detectors. This is due to the fact that the secondary radiation products of radiative capture interaction take the form of gamma-rays. These gamma-rays are difficult to be separated from the background gamma radiation.

On the other hand, non-radiative capture reactions result in the ejection of more than one neutron or charged particles such as proton, alpha or triton. The emission reactions such as (n, p), (n, α) and (n, t) are much more attractive for neutron detection because the secondary radiation products are charged particles. Most of these reactions are endothermic reactions. However, there are some atoms that can undergo an exothermic reaction, where energy is released. These atoms are ^{3}He, ^{6}Li and ^{10}B, which have high neutron absorption cross-section, making them a good choice for neutron detection.

2.3 Neutron detection method

There are different neutron detection methods depending on the neutron energy, where the neutron interaction cross-section is strongly based on the neutron energy. If the neutrons have low kinetic energy (< 0.5 eV), they can undergo nuclear reactions with a converter, which has a large neutron capture cross-section. Thus, neutrons can be detected through the emitted secondary reaction products. In contrast, if the neutrons have an energy higher than 0.5 eV, they perform elastic scattering in a hydrogenous material such as water or high density polyethylene,

where a neutron can be detected via the detection of the recoil nucleus.

Selection of an appropriate type of neutron detection method depends on the applications, where it will be used. These applications range from a simple monitoring of neutron fluxes to neutron radiography. The following sections will give a brief overview about slow and fast neutron detection methods.

2.3.1 Slow neutron detection

Slow neutrons have low kinetic energy, and they cannot transfer a detectable amount of energy to the nucleus through elastic scattering interactions. Consequently, this is not the type of interaction on which the detectors of slow neutrons can be based, however, these interactions bring the slow neutrons into thermal equilibrium with the medium. Once neutrons have been thermalised, they can be captured by a neutron converter material, then neutrons are detected indirectly via the ionisation produced by the secondary radiation reaction. Hence, all slow neutron detectors rely heavily on neutron-induced nuclear reactions that can create secondary radiation of sufficient energy, which can be detected directly. This induced reaction is known as an absorption interaction, which should have a positive Q-value (the amount of energy released) to be as energetic as possible.

There are various factors, which should be considered regarding the detection of these thermal neutrons. First, the thermal neutron absorption cross-section (σ) should be high so that an efficient detector can have small dimensions and the probability of neutron capture is high. Second, the target nuclei should have a considerable isotopic abundance as a natural element or instead artificially enriched samples should be available for the fabrication of the detector. Third, in numerous applications, large amounts of gamma-rays are found in combination with neutrons, therefore, the choice of the nuclear reaction affects the ability to discriminate against these gamma-rays in the detection process [5].

2.3.2 Fast neutron detection

The slow neutron detection method can also be applied to detect fast neutrons, however, the efficiency of this method is limited because the reaction probability reduces rapidly with increasing neutron energy. Therefore, the detection of fast neutron is based either on using neutron moderation or elastic scattering [23].

In neutron moderation, firstly neutrons are slowed down to low energies through elastic and inelastic scattering by using suitable moderators, then a slow neutron detection method is applied. In the second case, the incoming neutron is in the keV range or higher, thus, it is possible to detect this neutron by the recoil nu-

cleus coming from an elastic scattering interaction. This is due to the elastic cross-section for fast neutron being higher than the absorption cross-section, especially for a hydrogen-rich material such as polyethylene, which can deliver a recoil proton through the (n, p) elastic reaction. This reaction is a directional reaction, where the recoil proton has the same direction as the incident neutron. Moreover, the neutrons energy can be measured via the energy of the recoil protons. This is due to the fact that the fraction of energy transferred per neutron collision with the target nucleus increases as the mass of nucleus decreases.

It is clear that there are important differences between the detection process of the neutron in fast and slow neutron detectors. Fast neutron detectors can be designed to record both the presence of the neutron and measure its energy. On the other hand, slow neutron detectors can only indicate the existence of the neutron through the exothermic (+Q-value) nuclear reaction with a neutron reactive material.

2.4 State of the art in slow neutron detectors

Generally, radiation detectors can be divided into active and passive detectors based on the time needed for their response to radiation. In this work, the focus will be on active detectors, which have an immediate response to the radiation. This is in contrast to the passive detectors, which need to be read at a later stage in order to ascertain the level of radiation exposure recorded.

Active detectors can be categorised into three main types. These types are gaseous and semiconductor detectors, which depend on ionisation, and scintillation detectors, which rely on excitation. Each of them is briefly reviewed in the following sections.

2.4.1 Gaseous detectors

A gaseous detector is a devices, which consists of a volume of gas between two electrodes, with an applied electrical potential difference among these electrodes. The gas is ionised when a charged particle or photon passes through it. This ionising radiation loses energy in the gas by generating electron-ion pairs. Hence, the amount of ionisation in the gas volume is a measure of the amount of radiation present. Moreover, the measured charge or current in these detectors is proportional to the applied voltage and their sensitivity depends on the volume and the pressure of the gas. The gas-filled detectors can also be used in the detection of fast neutrons, where they are surrounded by neutron moderators such as

high density polyethylene to slow down the fast neutrons. Gaseous detectors have the ability to cover large areas as they have a high geometric detection efficiency. However, they are bulky detectors, which need to be operated at high voltages and high pressures. Figure 2.3 represents a simple schematic of gaseous detectors configuration.

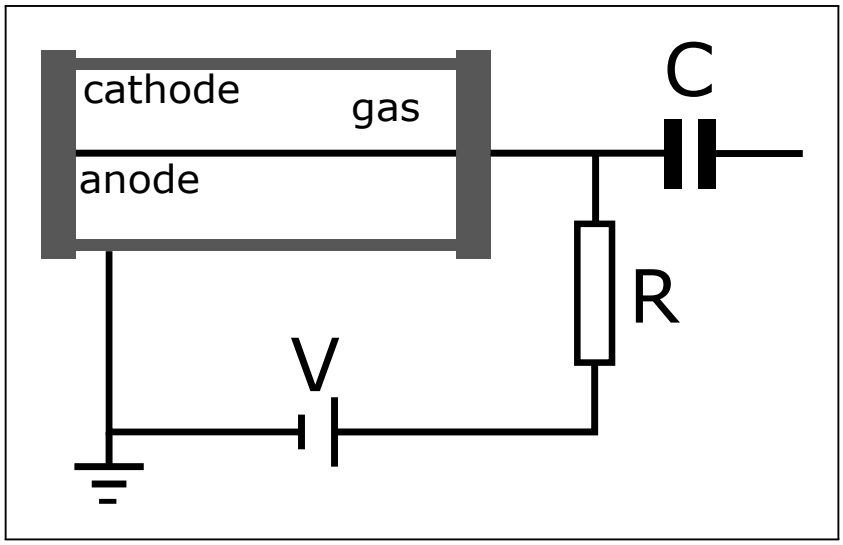

Figure 2.3: Schematic diagram of the gas filled detectors.

There are three different types of gaseous detectors, which can be used in the detection of thermal neutrons. These detectors are ^{3}He-filled gas proportional counters, boron trifluoride (BF^3) proportional tubes and boron-lined proportional counters [5]. These devices are only able to detect and count neutrons, but they cannot indicate their energy. They also offer high thermal neutron detection efficiency with good gamma discrimination [22]. As a part of this PhD work, a ^{3}He-filled gas proportional counter has been used in the characterisation of the thermal neutron flux from the neutron source. Therefore the following subsection is going to outline this type of gaseous thermal neutron detector.

2.4.2 ^{3}He-filled gas proportional counters

^{3}He gas is an isotope widely used for thermal neutron detection in gas detectors, since it has a large thermal neutron absorption cross-section (5330 b). In these counters the thermal neutron interacts with the ^{3}He nucleus, where it can be captured ejecting a tritium, $^3_1$H, at 0.191 MeV and a proton, p, at 0.574 MeV with a total amount of energy, Q-value, of 0.765MeV, according to the following reaction.

$$^3\mathrm{He} + {}^1_0\mathrm{n} \longrightarrow {}^3\mathrm{H} + {}^1\mathrm{H} + 765\,\mathrm{keV}$$

The charged particles are ejected in opposite directions, where the whole energy of the reaction (Q-value) is shared between them. This is due to the fact that the kinetic energy of the incident neutron is small and has no effect on the energy and the direction of the emitted secondary reaction products [24].

^{3}He tubes are usually operated in a proportional mode with a potential range of $1200-1800$ V, such that the produced ionisation by the reaction products initiates the multiplication process. This charge amplification improves the signal to noise ratio and reduces the required electronic amplification. ^{3}He-filled gas detectors can achieve intrinsic detection efficiency of up to 77% [25]. Furthermore, they work in pulse readout mode, where neutron and gamma-ray signals are distinguished by their amplitude [26].

One of the main issue of ^{3}He-filled gas detectors is that the amount of ^{3}He available for use in gas neutron detectors has become more restricted. This is due to the fact that the world wide ^{3}He reserves are foreseen to be consumed in the coming decades [27]. In addition, the supply of ^{3}He is limited to the production as a by-product from the decay of tritium, which is produced as a by-product of nuclear reactor operation [28]. Consequently, alternative detection technologies need to be investigated, which are based on solid state detectors such as scintillators and semiconductors.

2.4.3 Scintillation detectors

Scintillators are a subdivision of the solid-state detectors. They are considered as one of the largest class of detectors for neutron detection [29–34]. The purpose of these detectors is to achieve faster detection of neutrons than what is possible with gas-filled detectors. The scintillation detector consists of a scintillator material connected to an electronic light sensor such as a photomultiplier tube (PMT).

Scintillation materials operate by absorbing the incident radiation, which raises the energy level of the electrons into their excited states. Subsequently, these exited electrons lose their energy via de-excitation process, where the scintillator material emits photons in the visible light range. The PMT absorbs the photons emitted from the scintillator by the photocathode, where primary electrons are produced via the photoelectric effect. These electrons are guided towards the dynodes by the applied electric field, where the secondary electrons are produced. The subsequent multiplication of these secondary electrons results in an electrical pulse, which holds information about the initial incident radiation. Figure 2.4 describes the working principles of an scintillator detector.

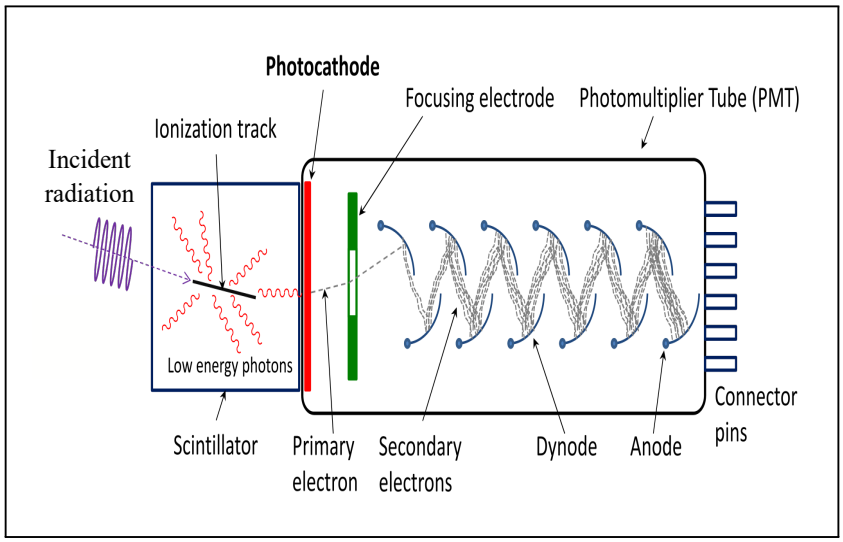

Figure 2.4: Schematic diagram of a scintillation detector [35]. The sketch shows a scintillation material coupled to a PMT.

Scintillators are typically categorised as organic or inorganic, where the scintillation mechanism is different. Organic scintillators depend on fluorescence, which results from molecular transition, while the production of light in inorganic scintillators relies on electronic transitions.

Organic scintillators (plastic or liquid) are often used for fast neutron detection. The neutrons interact in these scintillators through elastic scattering with the nuclei present (mostly carbon and hydrogen). The most useful scintillation light comes from the recoiling hydrogen nuclei as the neutron can transfer 100% of its energy to the recoiling proton. The kinetic energy of the scattered proton is absorbed by the scintillator, then it will be converted into heat and visible light. The visible light can be collected in a PMT optically coupled to the scintillation material, where it is converted into an electronic pulse. The magnitude of this electronic pulse is related to the kinetic energy of the recoiling proton. A good organic scintillation material has a high efficiency for converting the recoil particle energy to fluorescent radiation and it should be transparent to its own radiation.

Inorganic scintillators are quite commonly used as slow neutron detectors. They are manufactured by loading a typical neutron active material such as ^{10}B and ^{6}Li into the inorganic scintillation material. These neutron active materials initiate the production of light based on the energetic charged particles or gamma-rays, which are created by capturing thermal neutron.

Both organic and inorganic scintillators are much less effective for background gamma-ray discrimination compared to the gas-filled detectors. This is due to the fact that the detection process of the secondary radiation product is the same as if light was produced by a gamma-ray interaction. In addition, the secondary

electrons from these gamma-ray interactions tend to deposit all of their energy in these solid scintillators, but they can only deposit a small fraction of their energy in the gaseous detectors.

2.4.4 Semiconductor detectors

Semiconductors are another class of solid-state radiation detectors, which in general offer better energy resolution and faster response than the sintillators and gaseous detectors. Since the density of semiconductors is high, they have a greater stopping power. As a result, a semiconductor can collect the charge carriers generated by the incident radiation in a much smaller volume than those needed by gas or scintillation detectors. Therefore, semiconductors can provide more compact configurations than the other two types of radiation detectors. The general drawbacks of semiconductor detectors are the high cost, the low efficiency and the need for high purity materials, which are defect free crystals to promote a charge transport through the semiconductor detector [34].

A semiconductor detector is usually a silicon or germanium of p-n junction, which is formed when an n-type (donor) material is fused together with a p-type (acceptor) material creating a semiconductor diode, which operates in a reverse bias mode. Figure 2.5 presents the basic configuration of the semiconductor diode, which can be used as a radiation detector. This configuration has the structure of lightly doped (intrinsic semiconductor) region in between p-type and n-type extrinsic semiconductor to form p-intrinsic-n (PIN) junction (see appendix A.2). These highly doped regions are used to create Ohmic contacts with the use of metallisation in order to be able to collect the charges produced by radiation [36].

The charge carriers that comprise the signal are the negative electrons and positive holes (e-h pairs). These pairs are directly produced as a result of the deposited energy by the incident radiation via a cascade of collisions or interactions with electrons and atomic nuclei of the sensitive part of the diode (depleted region as presented in fig. 2.5). The average energy necessary to create an e-h pair in silicon is 3.62 eV at 300 K, this value is 10 and 100 times lower than that required for gaseous and scintillation detectors respectively [13]. The total number of e-h pairs is proportional to the amount of energy that has been deposited by the incident radiation particle or photon into the semiconductor. These pairs are separated by an applied reverse bias, where they can be collected by their respective electrodes and an electronic pulse is produced. This pulse will be processed in the attached readout electronics, and thus the energy of the incident radiation can be found (see appendix A.3 and figs. A.4 and A.5).

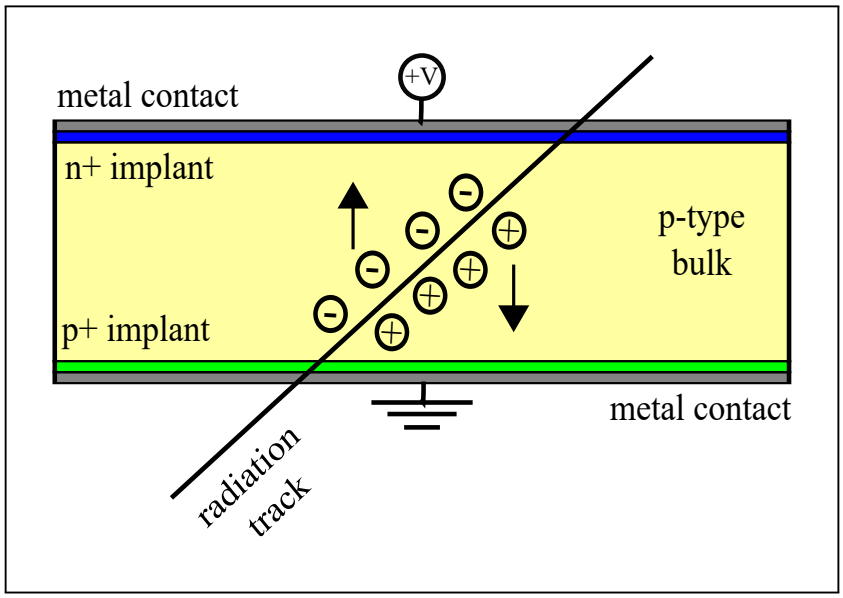

Figure 2.5: Schematic diagram of a semiconductor sensor, which is traversed by the incident radiation that creates e-h pairs inside the diode bulk. The diode is reversely biased to separate these e-h pairs and drift them to their respective electrode.

2.4.4.1 Semiconductor neutron detector

Development in semiconductor fabrication technologies has improved detectors, which are applied nowadays in a variety of neutron detection systems. These detectors can be divided in two groups, which are determined by the implementation of the neutron converter material in the detector, as can be seen in fig. 2.6 [37].

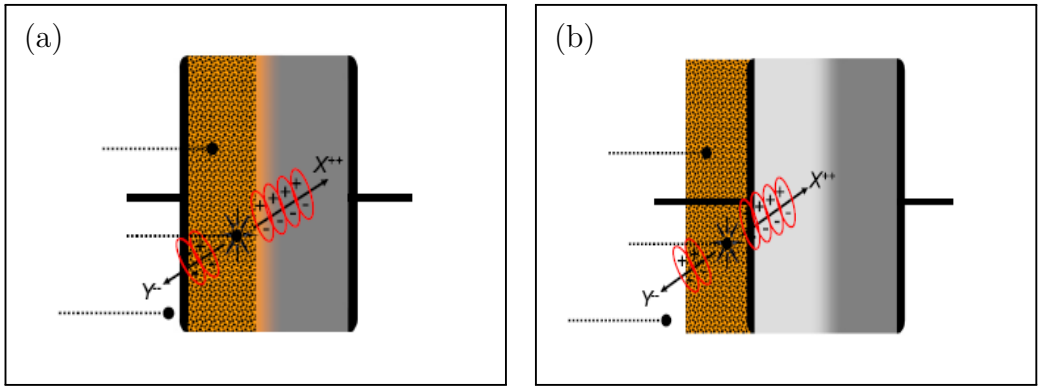

Figure 2.6: Configuration of both (a) direct and (b) indirect conversion semiconductor detector [37].

The first group is direct conversion semiconductors, where the semiconductor material is neutron sensitive, such as BP, BAs, BN, HgI_2, CdTe, CdZnTe and GdAs [38–41]. This type of material is able to capture a neutron resulting in charged particle reaction products, which create e-h pairs inside the sensitive part

of the detector (see fig. 2.6a). This means almost all of the energy of the charged particle is available for e-h pairs creation, while loss of their energy is minimised.

The neutron sensitive materials which are incorporated in such devices should have a high neutron capture cross-section that yield charged particles with moderate energy and are capable of producing and separating e-h pairs. Thus, the problem of these direct conversion semiconductor devices is that they are thick, and require high voltage bias (300-1000 V). Moreover, the charge carrier transport properties of this material are poor due to the trapping which severely limits the detector signal. As a result, the collected charge is very low, which needs to be differentiated from the electronic noise by increasing the threshold level. Hence, the detection efficiency is dramatically reduced.

The second group is an indirect conversion semiconductor, where the semiconductor and the neutron converter materials are not the same. The geometry of these devices consists of a semiconductor sensor coated with a neutron converter material that strongly absorbs neutrons (see fig. 2.6b). The thickness of this converter layer should allow the primary reaction products (mainly charged particles) to reach the sensitive volume of the detector. In this case only the charged particles that enter the sensitive part of the semiconductor detector can create e-h pairs and produce a signal. However, indirect conversion devices are based on well understood semiconductor processing technology. They are limited in their total detection efficiency due to the unavoidable effect of the primary charged particles self-absorption inside the conversion layer [42].

Ultimately, the thickness of neutron sensitive materials for the indirect conversion neutron detector should be optimised. This optimisation allows the reaction products of sufficient energy to interact with the sensitive part of the detector and produce the electronic signal. In addition, this thickness should have a high neutron capture probability to improve the detection efficiency. The general design consideration and challenges associated with indirect conversion semiconductor neutron detector will be addressed in the next section.

2.5 System design

The general design considerations for choosing the material and the geometry that maximise the detection efficiency and the performance of semiconductor thermal neutron detectors will be discussed. The device plane should be perpendicular to the direction of the incident neutron flux, in this configuration the largest amount of neutrons can pass through the sensitive neutron converter. As a result, the probability to capture a neutron increases [43]. The thermal neutron absorption

cross-section of the converter should also be high to increase the probability of the interaction [44].

In addition, the lateral dimension of this semiconductor diode should be larger than the maximum range of the charged particles emitted from the adjacent neutron converter layer. Hence, the depleted region of the detector can fully stop these charged particles and absorb their energy. The absorbed energy in the detector is the total energy of the charged particle minus the energy lost in the neutron converter layer. Therefore, the maximum energy deposited in the detector will be when a charged particle enters the detector in an orthogonal trajectory. This is due to the fact that the energy retained by a particle when it reaches the detector active volume decreases as the entrance angle changes from orthogonal [45].

Overall, the studies highlight the general design aspects regarding the semiconductor thermal neutron detectors. They indicate that the principle is to optimise the thickness of both the neutron converter material and the semiconductor sensor to maximise the detection efficiency and gamma-ray rejection factor. Thus, the optimum thickness of the neutron converter layer should have high neutron capture efficiency, while the generated charged particles are able to enter the sensitive volume of the detector with sufficient energy. In addition, this volume should be able to stop the charged particles and absorbs their energy to create e-h pairs and produces an electronic signal.

2.5.1 Choice of neutron reactive materials

Most thermal neutron detectors are based on the induced reaction with a neutron converter material [24]. The different reaction types, products and converter materials are summarised in table 2.2. The optimal converter should have a large absorption cross section (σ) for high detection efficiency. Moreover, the range of the induced charged particles should be large compared with the converter thickness and they should be energetic enough for the differentiation from the gamma radiation [46]. Prior studies have identified that the isotopes ^{6}Li, ^{10}B, and ^{157}Gd have these features and they are the most studied materials to be used as the converter of thermal neutrons into the secondary radiation products [47–52].

Gadolinium has two isotopes with a high microscopic thermal neutron absorption cross-section compared to the other stable nuclides; those are ^{157}Gd (255000 barns, natural abundance 15.65%) and ^{155}Gd (61000 barns, natural abundance 14.8%) [53]. It is well known from a variety of studies [54–57], that the detection of thermal neutrons relies upon the reaction ^{157}Gd(n,γ)^{158}Gd, which results in the emission of several small energy gamma-rays and energetic conversion

Table 2.2: Thermal neutron nuclear reaction types and products.

Reaction Types	Reaction Products	Nuclei of Interest
Radiative capture (n, γ)	γ-rays	^{155}Gd, ^{157}Gd
Charged particle production (n,p), (n,α), (n,t)	^{7}Li, α, ^{3}H or other light nuclei fission products	^{10}B, ^{6}Li, ^{3}He
Neutron-capture induced fission	fission products of U or Pu	^{235}U, ^{239}Pu

electrons ranging in energy from 29 keV up to 246 keV. Only 60% of neutron absorption results in the emission of conversion electrons, where 88.5% of these electrons have an energy less than 100 keV. Although natural gadolinium (^{157}Gd) has a very large thermal neutron absorption cross-section, the emitted gamma-ray and conversion electron are difficult to be separated from the background gamma radiation in the measurement field. For this reason, gadolinium coating is not preferred to be used as a thermal neutron converter in semiconductor neutron detectors.

The other two neutron interactions used for thermal neutron detection are the ^{10}B(n,α)^{7}Li and ^{6}Li(n,α)^{3}H reaction. In these reactions, the emitted charged particles can be detected by a charged particle detector, for instance a silicon semiconductor detector. The advantage is that the energy deposited by these reaction products is higher than the energy of the background gamma-rays [58]. Hence, the neutron events can easily be distinguished from the other events including the background gamma radiation.

The thermal neutron (0.0259 eV) absorption cross-section (σ) of ^{10}B is 3840 b, which is a relatively high value. However, this value is inversely proportional to the neutron velocity over much of the energy range. It was reported that there are two different reactions, which can occur with distinct Q-values (the amount of energy released and shared by the reaction products) due to the interaction of a neutron with ^{10}B. The first is ^{10}B(n,α)^{7}Li with a total Q-value of 2.792 MeV and the reaction products are a ^{7}Li ion (at 1.015 MeV) and an alpha-particle (at 1.777 MeV). The other is ^{10}B(n,α)^{7}Li* with a total Q-value of 2.31 MeV, producing a ^{7}Li ion in its first excited state (at 1.472 MeV) which decays rapidly to the ground state by the emission of a 480 keV γ-ray and an α-particle (at 0.84 MeV) [59, 60].

^{6}Li has a thermal neutron absorption cross section (σ) 940 b, which is also inversely proportional to the neutron kinetic energy. The primary reaction of a neutron interacting with ^{6}Li is shown according to the following equation [61]:

$$^{6}\mathrm{Li} + {}^{1}_{0}\mathrm{n} \longrightarrow {}^{3}\mathrm{H} + \alpha.$$

This reaction produces an alpha particle (at 2.05 MeV) and a triton (at 2.73 MeV) in opposite directions, where the total amount of energy released per reaction is 4.78 MeV [62–64]. Although ^{6}Li has a smaller thermal neutron absorption cross section than ^{10}B, the higher energy reaction products and lower atomic mass density of ^{6}Li make it attractive to be used as a converter film/foil for thermal neutron detectors. This is due to the higher range of reaction products through a ^{6}Li converter than that inside a ^{10}B. The efficient range of the triton (L_t) and the alpha-particle (L_α) from a ^{6}Li converter layer is 126.77 μm and 19.05 μm respectively [65]. The chemical reactivity of pure ^{6}Li and its degradation require a complicated handling procedure in a protective environment [66]. Therefore, ^{6}Li is more commonly used as ^{6}LiF, which is more stable. However, the range of the reaction products will be affected with L_t becoming 29.25 μm, while L_α changes to 4.64 μm [65].

In conclusion, these studies show that the detection of thermal neutrons principally require the presence of a converter material that has a high neutron capture probability and a strategy for differentiation from gamma-ray interaction. Also, it has been shown that the type and the energy of the released reaction products will depend on the chosen neutron reactive material. The primary materials, which are used with the semiconductor detectors to convert the neutron into charged particles radiation are ^{10}B and ^{6}Li. This is due to their high absorption cross-section (σ) and suitability for incorporation into a solid medium. However, ^{6}Li is preferred in this work due to the relatively large energy released and the higher range of reaction products through the converter film/foil.

2.5.2 Planar silicon neutron detectors

Planar semiconductor detectors coated with a neutron converter are considered as the simplest design used to adapt semiconductor devices for the detection of thermal neutrons, which has been reported since the 1960s [67–70]. The detector configuration consists of a planar semiconductor sensor such as Si, and a layer of neutron converter deposited on its surface [71], as presented in fig. 2.7. The planar diode with thin contact layers is preferred to reduce the energy loss of the reaction products coming from the neutron converter [72]. In this configuration, neutrons can be captured in the converter layer, such that if their reaction products reach the sensitive detector volume, these neutrons will be detected [73].

The planar design has unavoidable geometric limitation due to the fact that the neutron interaction probability depends strongly on the neutron converter thickness. The probability of neutron capture in the converter increases with the

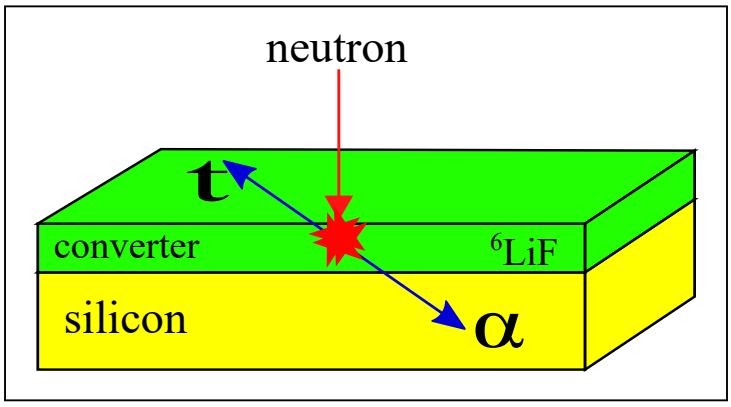

Figure 2.7: Principle of neutron detection using planar Si semiconductor configuration. As an example is shown the reaction of thermal neutrons on ^{6}Li (which is in the form of ^{6}LiF compound).

growth of the converter layer thickness. On the other hand, the chance that the neutron capture reaction products will reach the detector's sensitive part decreases with the increment of the neutron converter thickness. This is due the fact that the reaction products lose their energy within the converter itself. Therefore, an optimal converter material thickness has to be found.

Furthermore, only those charged particles which are ejected in the direction of the diode interface can be detected. This is known as the 2π geometry, which allows up to half of the primary reaction products to generate (e-h) pairs inside the depletion region of semiconductor detector. For instance, a thin layer of ^{6}LiF was attached to a reversely biased Si diode, where 50% of the released energy was deposited in the depletion region of this diode [74].

It was found that the maximum detection efficiency of this planar configuration cannot exceed 5% for both ^{10}B and ^{6}LiF converter materials [75, 76]. This detection efficiency can be enhanced up to 11% by using pure ^{6}Li metal, however, the chemical reactivity of ^{6}Li complicates the fabrication process of the detector. In addition, the thermal neutron detection efficiency can be improved via various methods such as stacking a sandwich configuration of Si-converter-Si [77].

The direction of neutron flux should also be taken into the consideration of the planar design principles. This is because thermal neutrons follow the exponential attenuation law when they are passing through the converter material. If the detector is irradiated from the front-side more neutrons will be captured on the surface of the converter nearest the neutron flux. The reaction products, which are created close to the outer surface must move through the converter layer to reach the charged particle detector. Therefore, many of them will be lost inside the converter material. This effect increases for a thick converter, which has thickness

similar to or higher than range of reaction products. Front side irradiation of coated neutron detectors would result in a detection efficiency range of $4\% - 11.6\%$ based on type of converter material [77].

Most conventional semiconductor materials have a very low probability of interacting with free neutrons. For example, microscopic thermal neutron cross-section for naturally occurring silicon is 2.24 barns, this means a thermal neutron would have to travel an average distance of 8.6 cm (mean free path) before a scattering or capture event would occur [78]. Consequently, whole detector structure could be irradiated from backside where neutrons will be captured closer to boundary between converter and semiconductor detector. In this case, probability that neutron capture reaction products reach detector sensitive volume is higher and detection efficiency increases. In addition, converter thickness does not have to be optimised and can be thicker than range of charged particle reaction products. However, neutrons, which will be captured on surface of converter film, are less likely to be detected for same reason as for front side irradiation. Therefore, sandwich detector configuration can be used to detect reaction products emitted in opposite direction. Moreover, this sandwich detector with optimised converter thickness can also be used to detect coincidence events for a higher rejection factor of gamma-ray as discussed later in this work.

2.5.3 Medipix-1 and Medipix-2 neutron imaging detectors

The radiation detection and imaging systems have been developed, where imaging detectors have achieved high spatial resolution, high sensitivity and low noise. Examples of such detectors are Medipix-1 and Medipix-2 X-ray imaging detectors. These devices were originally designed at CERN for position sensitive single X-ray photon detection.

Medipix-1 is a silicon pixel detector. This pixel detector consists of a semiconductor chip which is bump-bonded to a readout chip. One side of silicon detector is fully coated by metal to form a common backside electrode with readout chip. Front side is divided into a matrix of square pixels. This matrix consists of 64×64 pixels, where each one has a dimension of 170 μm $\times$ 170 μm and the total sensitive area is 1 cm^2. In addition, each pixel in the matrix is connected to its respective preamplifier, discriminator and digital counter integrated on the readout chip [79].

Medipix-2 is the advanced version of Medipix-1. The pixel area in Medipix-2 has been reduced to 55 μm $\times$ 55 μm, however, number of pixels in the matrix increased to 256×256 pixels. Therefore, the sensitive area of the detector increased up to 2 cm^2. Furthermore, the readout electronics of Medipix-2 has the ability to

use two discriminators to set an energy window for selecting the measured energy of radiation [80].

These Medipix devices cannot detect thermal neutrons directly by their silicon pixel detectors. Therefore, they must be combined with a neutron converter, which is deposited on their surfaces [81]. Thermal neutrons are converted in this converter to secondary radiation products, which are subsequently detected by the pixel detector. The created signal by these charged particles in each pixel is high enough to set a discriminator threshold against the electronic noise and the possible background gamma-rays.

It was shown that the optimised converter layer thickness on both Medipix-1 and Medipix-2 has a limited detection efficiency of 3% with the planar detector geometry [82]. For instance, a ^{6}LiF film of 3 mg/cm^2 surface density on silicon pixel detector would be capable of achieving 3% thermal neutron detection efficiency. In addition, the maximum detection efficiency has been estimated using Monte Carlo simulation to be 5% for ^{6}LiF film with a surface density of 7 mg/cm^2 [83, 84]. Therefore, it was suggested that the detection efficiency of Medipix-2 could be increased by creating dips or pores in the silicon sensor body, which are filled with ^{6}LiF as a neutron converter material.

It was found that using a chip of 5×5 mm^2, thickness of 300 μm and an array of inverted pyramids with base of 60×60 μm^2 and 28 μm deep inside the chip could increase the detection efficiency from 4.9% to 6.3%. Hence, it has been noted that the detection efficiency could be increased by using 3D structures in semiconductor detectors [85].

2.5.4 3D thermal neutron detectors

The main reason behind constructing 3D structure in semiconductors is to overcome the limited thermal neutron detection efficiency of the silicon planar detector geometry, when coupled with a neutron converter material. This 3D structure can increase the surface between the neutron converter material and the detector diode. In addition, 3D structures provide a larger volume of the neutron converter, therefore, the neutron capture probability increases. Although, the neutron converter volume increases, the charged particle reaction products still retain a high probability to be detected and, thus, the thermal neutron detection efficiency increases. Therefore, it was suggested that the incorporation of trenches in a semiconductor diode subsequently filled with a neutron reactive material would increase the thermal neutron detection efficiency [86]. In recent years, there has been an increasing amount of literature on perforated semiconductor neutron detectors, where the in-

trinsic thermal neutron detection efficiency depends on the perforation geometry, size and depth [87–90].

The thermal neutron detection efficiency of the circular hole and parallel trench perforations in Si diode was investigated theoretically [91, 92]. These perforations are filled with a neutron converter material. It was indicated that 25% thermal neutron detection efficiency could be achieved for a single coated device. Also, it was expected that the detection efficiency could be doubled to 50% for a compact sandwich device. Furthermore, optimised microstructured designs are theoretically predicted to reach 70% thermal neutron detection efficiency [93, 94].

In view of all that has been mentioned so far, one may hypothesise that solid state neutron detectors traditionally do not have the sensitivity of ^{3}He tubes because they are such small devices. Therefore, newly developed perforated semiconductor neutron detectors can be designed to achieve high thermal neutron detection efficiency. Theoretically these perforated designs might be considered as possible, however, most of them are not technologically realistic, since they are not manufacturable with standard Micro-Electro-Mechanical System (MEMS). MEMS allows both electronic circuits and mechanical devices to be manufactured on silicon chips in the clean room facility. In addition, filling perforations with a neutron converter material is still an unresolved issue.

In summary, an efficient solid-state thermal neutron detector can achieve high detection efficiency by increasing the surface area between the neutron converter material and the semiconductor sensor. Therefore, planar semiconductor neutron detector can reach high thermal neutron capture probability by using multilayer configuration and thus, the neutron detection efficiency increases. For instance, using a planar array of five detector elements which encompassed 0.43 m^2 can achieve thermal neutron detection efficiency up to 60% [95].

2.6 Response of neutron detectors to gamma-rays

Insensitivity to background gamma-rays is considered to be a basic criterium of thermal neutron detectors. Therefore, rejection of gamma-ray is an important factor in the design of these detectors. Like neutrons, gamma-rays have no charge and interact with matter via elastic and inelastic interactions. These interactions with matter will lead to excitation and ionisation in the detection medium (Si diode for this project). As discussed by Knoll [5], Leo [36], and Turner [96], the interaction of gamma-ray photons with matter is classified based on the energy of

gamma-ray (E_γ) and the atomic number (Z) of the material. Therefore, there are three possible interaction mechanisms.

The first interaction mechanism is the photoelectric effect. It involves the absorption of all energy of the incident photon (E_γ) by an atomic electron with subsequent ejection of this electron (photoelectron) from the atom, as shown in fig. 2.8. The energy of the ejected electron is $E_e = E_\gamma - E_b$, where E_b is the atomic electron binding energy. In addition to the photoelectron, the interaction also creates an ionised absorber atom with a vacancy in one of its bound shells. This vacancy is filled through the capture of a free electron from the medium and/or via a rearrangement of electrons from other shells of the atom. The photoelectric effect is the predominant interaction mechanism for low energy gamma-rays in a range typically from 1 to a few hundred keV and the process is enhanced by a material, which has high atomic number (Z).

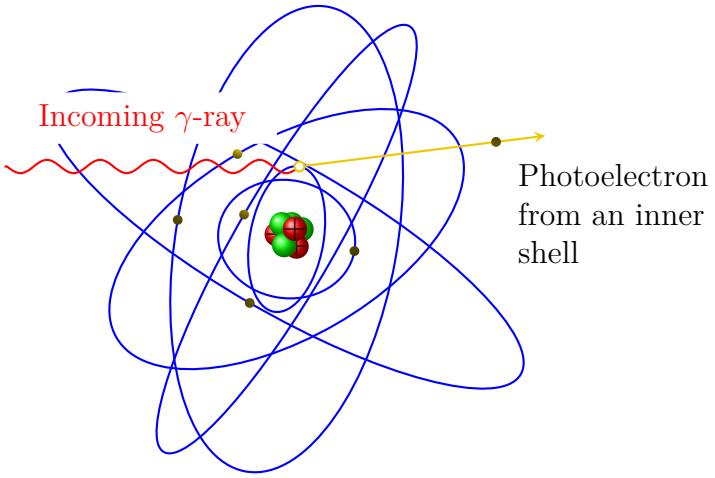

Figure 2.8: Interaction of gamma-ray with matter via photoelectric absorption process.

The second type of interactions is Compton scattering, where the incoming photon of energy (E_γ) is scattered with an energy of (E'_γ) through an angle (θ) with respect to its original direction of travel. Figure 2.9 presents the Compton scattering interaction mechanism, where the incoming photon transfers a portion of its energy to an electron which will be known as the recoil electron. The atomic electron binding energy is neglected due to the higher energy of the incident gamma-ray. Therefore, this recoil electron has an energy of $E_{r,e} = E_\gamma - E'_\gamma$, which induces ionisation in the detection medium. Compton scattering is the dominant interaction of photon with matter for photon energy larger than a few hundred keV up to a few MeV. However, beyond a few MeV the pair production mechanism becomes increasingly significant.

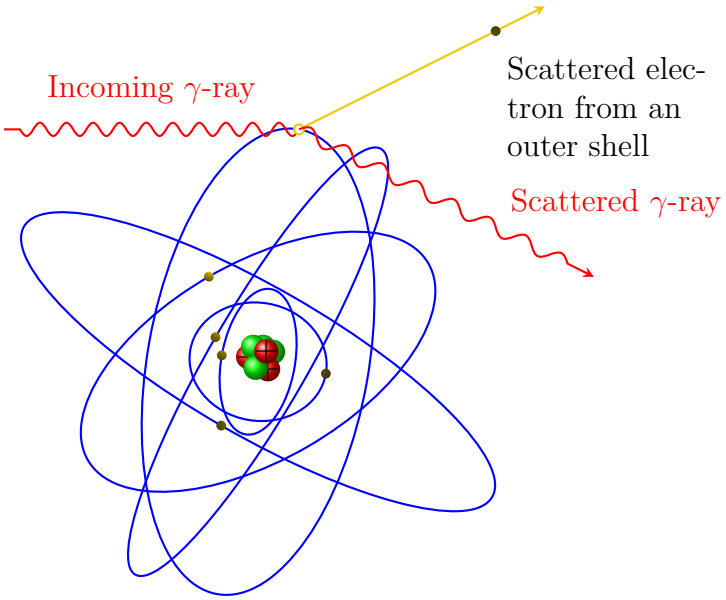

Figure 2.9: Compton scattering interaction mechanism.

Pair production is the last type of interaction of a photon with matter, where a high energy photon near a nucleus can be transformed into an electron-positron pair, as it can be seen in fig. 2.10. The photon energy goes into the rest-mass and the kinetic energy of the electron-positron pair. Therefore, the minimum energy necessary for this effect to take place is 1.022 MeV, which is equivalent to two electron rest masses (2×0.511 MeV). The probability of this interaction remains very low until the gamma-ray energy approaches several MeV and, thus, the pair production interaction mechanism is predominantly confined to high energy gamma-ray.

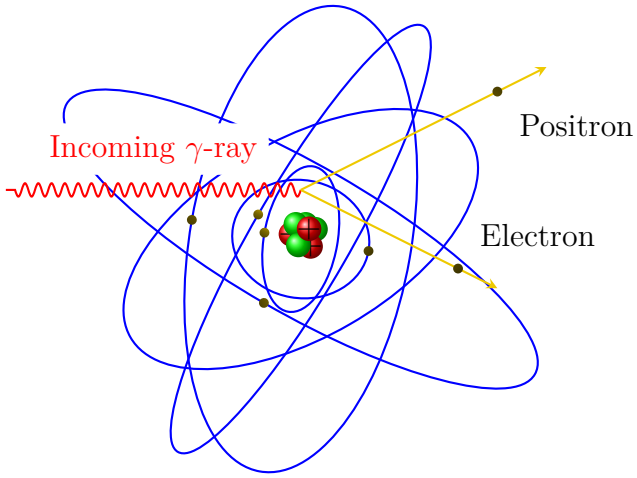

Figure 2.10: Electron-positron pair production due to the interaction of high energy gamma-ray.

Since the probability of interaction of photons with a particle in a given ma-

terial increases with the distance travelled, the sensitivity to gamma-ray can be reduced by decreasing the thickness of the semiconductor detector. In addition, the response of neutron detectors to different gamma-ray energy can be minimised by choosing a semiconductor detection medium with a relatively low atomic number (Z), such as silicon.

2.6.1 Neutron detection efficiency and purity in mixed radiation fields

It is important for any neutron detection system to have a pure neutron detection efficiency in a mixed radiation field with gamma-rays [97]. The problems produced by photons interacting in the neutron detectors arise mostly from pile-up, which is a combination of the interaction rate (number of photon per second) and the deposited energy per interaction (energy deposited mostly through Compton scattering). Therefore, some criteria have been proposed to determine the gamma-ray sensitivity and to specify the acceptable performance of different neutron detection systems [98]. These criteria are the absolute neutron detection efficiency ($\varepsilon_{abs,n}$), the intrinsic gamma-neutron detection efficiency ($\varepsilon_{int,\gamma n}$) and gamma absolute rejection ratio for neutron (GARRn).

The first criterion is the absolute neutron detection efficiency ($\varepsilon_{abs,n}$). It is defined as the ratio of pulses recorded by the detector to the total number of neutrons emitted by a source corresponding to the source-detector geometry (experimental setup). The absolute detection efficiency defines the performance of the neutron detector based on its properties and the geometrical positioning with respect to the neutron source. Therefore, it allows direct comparison of different neutron detectors. It was mentioned that the required absolute detection efficiency for neutron detectors is equivalent to $\varepsilon_{abs,n} \geq 0.11\%$ for 2 m distance between the source and the detector [98]. Moreover, the $\varepsilon_{abs,n}$ can be used to determine the intrinsic detection efficiency ($\varepsilon_{int,n}$) of a neutron detector based on the knowledge of the detector size and experimental geometry. The intrinsic efficiency ($\varepsilon_{int,n}$) is the number of counted events per number of neutrons hitting the detector. The intrinsic detection efficiency is not tied to the source-detector geometry and, thus, it can reduce the geometric dependence of the efficiency measurement [43]. As a result, both intrinsic and absolute detection efficiency are significant for specifying the response of a neutron detector.

The second criterion is the intrinsic gamma-neutron detection efficiency ($\varepsilon_{int,\gamma n}$), which is the number of photons that produce counts divided by the number of photons incident upon the detector. It measures the response of a neutron detector to

the presence of a pure gamma radiation field without any neutrons. Ideally, the $\varepsilon_{int,\gamma n}$ should be equal zero, which ensures that no gamma exposure will trigger a false neutron count. However, the standard specification for radiation portal monitor (RPM) systems, which are the largest neutron detection applications requires $\varepsilon_{int,\gamma n} \leq 10^{-6}$. This value can be achieved by setting an energy threshold of 1.4 MeV, where gamma radiation up to that energy is completely rejected [98].

The last criterion is the gamma absolute rejection ratio for neutron (GARRn), where it represents the neutron detector response in the presence of both gamma-ray and neutron sources. The GARRn is defined as the absolute neutron detection efficiency in a mixed radiation field ($\varepsilon_{abs,\gamma n}$) divided by the absolute neutron detection efficiency ($\varepsilon_{abs,n}$) of the neutron detector (GARRn = $\varepsilon_{abs,\gamma n}/\varepsilon_{abs,n}$). If gamma radiation has no impact on the neutron detector, the value of GARRn would be equal 1. With respect to the standard specification of radiation portal monitor (RPM) systems, the proposed GARRn is: 0.9<GARRn<1.1 at an exposure rate of gamma-rays of 10 mR/h.

Finally, it has been stated by Kouzes [97] that the GARRn requirements are more powerful than the requirements for intrinsic gamma ray detection efficiency. Therefore, the only requirements that need to be met for any neutron detector are those for $\varepsilon_{abs,n}$ and GARRn.

Chapter 3

Monte Carlo methods

3.1 Introduction

The Monte Carlo (MC) method was developed in the 1940s [99] by John von Neumann and Stanislaw Ulam. It is defined as a technique of numerical analysis that uses random sampling to construct the solution of a mathematical or physical problem [96]. Due to the advances in computer technology and power, where computers are able to perform millions of simulations quickly, this MC method has become widely used to simulate problems with a large number of coupled degrees of freedom which are difficult to be resolved by classic analytic method.

Monte Carlo methods are implemented as computational algorithms based on random sampling to determine their results. This technique of random sampling was first used to solve the mathematical problems in quantum mechanics, later it was applied to nuclear and ionising radiation physics. The large computational capacity of this MC method allows to sample a large system in a number of random configurations, where, it is possible to describe the whole system. Hence, there has been a huge increase and interest in using MC techniques in different aspects of medical physics such as radio-protection, ionising radiation dosimetry, radiotherapy and nuclear medicine.

3.2 Monte Carlo codes for nuclear and particle physics

The interaction of particles with matter is a random phenomenon with a probabilistic distribution depending on the type and energy of the interacting particles, where different physical processes can happen such as absorption, scattering or capture. Therefore, Monte Carlo codes are used to study the propagation of the radiation through matter in nuclear and particle physics. In addition, it is very useful to simulate the whole experimental setups, where it allows to optimise the experimental conditions to save computing time, cost of design, setting up and assembly of the experiment.

In general, the history of transported particle starts by creating the particle with position and energy coordinates according to a specified source distribution. After that the created particle travels a certain distance before undergoing an interaction with the media through which it passes. The types of interaction and the resulting secondary particles are determined by the interaction cross-section at that point, then these secondary particles will be also transported. The particle history ends when all particles have either deposited their energy in the medium or have left the geometry borders.

Specifically, in neutron processes, it is difficult to determine the transportation of the neutron due to the large number of interactions possible in material, which can change frequently along the path of the neutron. Therefore, it is possible to predict the behaviour of a large number of neutrons, which will undergo each type of interaction using MC methods, rather than trying to anticipate what a single neutron will do. Millions of simulated neutrons can be started with certain energies and directions, where they can travel distances according to their mean free path lengths, which depend on the material [100]. The implemented MC method will simulate the interaction of neutrons as a function of the required interaction, material and neutron energy. Such that if a specific interaction is selected, it will be followed by its consequential results. For instance, secondary particles are produced or changes in the direction and energy of the primary interacted particles. This simulation process will be iterated until the neutrons and the generated secondary particles are absorbed, escape from the simulation boundaries, or their energies are lower than the energy cut-off. There are several MC codes, which could be used in nuclear and particle physics. The method which will be used in this work is Monte Carlo N-Particle (MCNP). It represents a stochastic code which was originally developed by Los Alamos National Laboratory (LANL) [101],

for the transport of neutrons, photon and electrons. Also, Monte Carlo N-Particle transport code (MCNP) is considered as one of the most popular particle transport codes used in nuclear physics research [102]. Therefore, MCNP version 4C is used to model and determine the average neutron flux nv (nv is thermal neutron flux, neutrons/cm^2/s) associated with the different geometry configurations which will be discussed later.

3.2.1 MCNP4C simulation code

MCNP code is used for studying the interaction and transport of neutrons, photons or electrons. The code also deals with the transport of secondary gamma rays resulting from neutron interaction and treats the transport of both primary source electron and secondary electrons created in gamma-ray interactions. It uses continuous energy nuclear and atomic data libraries.

For neutrons, all reaction data given in a particular cross-section evaluation are included in the ENDF (Evaluated Nuclear Data File) library, which is periodically evaluated by the LANL research organisation. There are several types of ENDFs such as the ENDF/B-VI data library which accounts for the reaction of neutron with 90 materials in the energy range from 10^{-5} eV to 20 MeV. Moreover, the thermal neutrons are described by both free gas and S(α, β) models. In case of photons, the code takes account of photons scattering, the possibility of fluorescent emission after photo-electric absorption, absorption in pair production with local emission of annihilation radiation and bremsstrahlung. In addition, a continuous slowing down model is used for electron transport which includes positron, x-ray and bremsstrahlung. In the following sections the basic components of MCNP program are outlined. Note that the main units of measurements used in MCNP code are: centimeters for length, MeV for energy, barns for cross-section and g/cm^3 for mass density.

3.2.1.1 Geometry, material and source

The geometry of the simulated system in MCNP is defined by a 3-dimensional configuration consisting of cells. The cells are volumes which are defined by means of the intersection or union of surfaces, which are defined by supplying coefficients to the analytical surface equations. A material has to be assigned to each cell. Moreover, the particle source identifies the type of incident particle, its energy, position, direction and the area distribution. Simulated geometries, materials and source are described by specific cards as presented bellow.

- **Surfaces**

There are different types of surfaces in MCNP such as plane, sphere, cylinder, cone, etc. These surfaces are specified by the surface number (ID) and the value of the parameters that define the analytic equation of the surface. For instance, a plane (py) with an ID = 1 and normal to the y-axis at y = 3, implemented as following:

1 py 3

- **Cells**

Objects in MCNP are defined by using cells. They must be made up by a material, which is defined by its density and composition. Therefore, the cell-card should have a cell identifier (cell number), the identifier of the material of such cell (m), the material density (d) and the surface numbers that form this cell. Thus, the cell card in the input file is implemented as following:

cell-number m d surface number

- **Materials**

The material cards are used to define the isotopic composition of the materials in the cells and which cross-section libraries are to be used. Note that the density is not specified here. Instead, the density is specified on the cell definition card. This permits one material to appear at different densities in different cells. Hence, the material card specification is:

m ZZZ.AAA.nnX Mass or Atomic fraction

where m corresponds to the material number on the cell card, ZZZ is the atomic number, AAA is atomic mass and X is the class of data.

- **Source**

The most straightforward way to define a source in MCNP is by using the SDEF command. The simulated source implements the type of particles that interact with the geometry as well as its position, direction, shapes and energy spectra. For example, an isotropic point neutron source position at (x,y,z) with direction $\vec{r} = (1,0,0)$ is implemented with the following source-card:

SDEF pos=x y z dir=1 vec=1 0 0 par=1 erg=d1

mode n

3.2.1.2 MCNP input file

To run a MCNP simulation, an input file has to be provided by the user, in which the whole simulation is described. The input file consists of 4 main blocks as presented in fig. 3.1. These blocks are the message block (optional), where the program can be described. The second is a cell block, where the cell-cards are defined and the geometry of the setup is constructed. The third one is for the definition of surface cards which constitute the implemented cells. The last block is for the specification of other data such as material, type of source, physical models, cross-section libraries, tallies, number of histories and any other conditions which could be used to run the simulation.

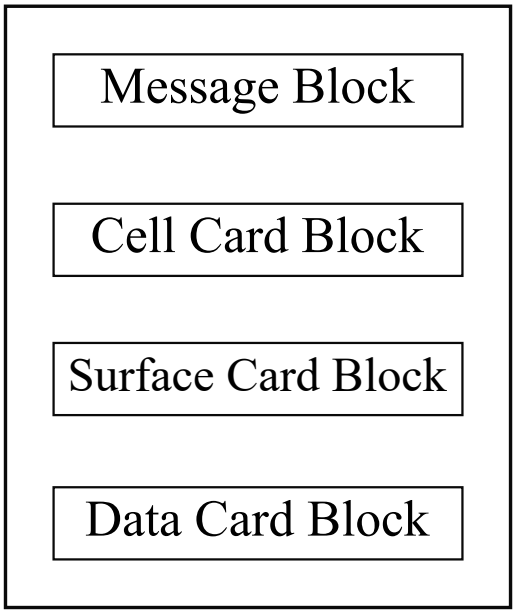

Figure 3.1: Structure of the input file to run MCNP simulation

3.2.1.3 MCNP output file

The estimation of the magnitudes evaluated by the MCNP code is obtained by means of the tally cards, which are built-in calculations. The tallies are out-files specifying the type of information to be gained from the simulation. Therefore, there are 8 different types of tally depending on the required information. For instance, tally F2 and F4 which have been used in the framework of this research for the determination of the average neutron flux over the surface and the cell of the converter material respectively. The unit of both F2 and F4 tallies is particles/cm^2. Tallies are normalised per unit source emitted particle. Hence, a tally estimate a mean value ($\bar{x}$) of scored quantity (x), with a relative standard

uncertainty (< 0.1) to be considered as a reliable results. In addition, MCNP provides a valuable tool for assessing the reliability of the results by performing 10 statistical tests on the tally, which must pass all tests. These 10 statistical tests are summarised below.

- **Tally Mean, $\bar{x}$:**

  1. The mean must exhibit, for the last half of the simulation, only the random fluctuations as N increases. No up or down trends must be exhibited.

- **Relative Error, R:**

  2. R must be less than 0.1.
  3. R must decrease monotonically with N for the last half of the problem.
  4. R must decrease as $1/\sqrt{N}$ for the last half of the problem.

- Variance of the Variance, VOV:

  5. The magnitude of the VOV must be less than 0.1 for all types of tallies.
  6. VOV must decrease monotonically for the last half of the problem.
  7. VOV must decrease as $1/\sqrt{N}$ for the last half of the problem.

- Figure of Merit, FOM:

  8. FOM must remain statistically constant for the last half of the problem.
  9. FOM must exhibit no monotonic up or down trends in the last half of the problem.

- Tally PDF, $f(x)$:

  10. The slope determined from the 201 largest scoring events must be greater than 3.

In conclusion, MCNP4 has been used to model different experimental geometries to determine the average neutron flux through the neutron converter as a function of the neutron energy. In the next section, GEANT4 simulation will be presented. This simulation toolkit has been used to determine the optimal thickness of the neutron converter material which results in the maximum thermal neutron detection efficiency.

3.3 GEANT4 simulation

GEANT4 (GEometry ANd Tracking) is an application programming interface, which was designed and developed at CERN by an international collaboration, formed by individuals from a number of cooperating institutes, HEP (High Energy Physics) experiments and universities [103, 104]. The first version of GEANT4 appeared at the end of 1998 and from that time it has been continuously improved into updated versions. It has been created exploiting software engineering and object-oriented technology and implemented in the C++ programming language. The software is freely available at source code level at the website of the project, http://geant4.cern.ch/. GEANT4 is not an executable program, but it is a set of predefined C++ classes, therefore, the users have to write their own code and compile it to generate an executable file.

GEANT4 was built on the accumulated experience of many contributors to the field of Monte Carlo simulation of physics detectors and physical processes. It studies in depth the interaction and the passage of radiation in matter, where it has a complete range of functionality including tracking, geometry, physics models, hits and provides a large amount of data to be analysed. GEANT4 also has the ability to handle complex geometries efficiently and allows the visualisations of these geometries and particle tracks through different interfaces. Initially, GEANT4 was designed to develop simulations of processes in high energy ranges, then it implemented physical models for the low energy range. Now, GEANT4 covers a wide energy range from processes at low energy (meV) like the interactions of optical photons and thermal neutrons, up to the high energy reactions (TeV), such as the collisions of heavy ions, and it includes all types of particles. GEANT4 is a powerful toolkit, which is applicable in different fields, such as nuclear and particle physics, high energy physics, accelerator design, space engineering, medical physics, radiation protection, dosimetry and radiobiology.

3.3.1 General specification of GEANT4

GEANT4 simulations can be divided into the following steps:

- Geometry of the system and the materials which compose this geometry.
- Response of the system through the sensitive detector, which can consist of one or several volumes, where the data is extracted.
- Generation of the particles of interest or the source of radiation.

- Physical process and models, which control and manage the interaction of the generated particles.
- Particles trajectory through the materials.
- Storage and trace of events.
- Setting the run.
- Visualisation of the detector and trajectories of particles.
- Data analysis and user interfaces.

These steps will give a chance to the users (i) to design their own systems of complex geometry with any type of materials and compounds; (ii) to choose the incident particles and to monitor the trajectory of these particles in their interactions with the system; (iii) to identify the processes that each particle undergoes in the matter and the energy deposited in it; (iv) to create radioactive sources specifying their position and energy distribution; (v) to create electromagnetic fields; (vi) to extract information (hits), which are the detector response. Finally, the users can visualise the geometry, the particles traces and analyse the whole simulation through the graphical interfaces.

The execution of GEANT4 simulation consists of four components. Firstly, 'the step', which is the minimum path of the particle between two subsequent interactions. Secondly, 'the track' or the sum of all steps, which have been taken by the particle. Thirdly, 'the event', which is the track history of a single incident particle. Finally, 'the run', which is the collection of all events that share the same geometry, physics list and primary particle generator.

Subsequently, GEANT4 divides the particle trajectories into series of steps with a certain mean free path, λ. This mean free path represents the average distance, which will be travelled by the particle before undergoing an interaction. The mean free path depends on the cross-section of the physical process that takes place and the atomic density (N) of the material. Hence, to achieve a simulation as real as possible, it is important to have accurate cross-sections.

GEANT4 determines the cross-section by formulas, parametrisations, or interpolation of database depending on the particle type, material and energy. Along the particle trajectory, the program will define the effective cross-section from the corresponding libraries as a function of the particle energy in each step and depending on the material in which it is located. Therefore, the code performs the radiation transport by choosing the process with the smallest interaction distance, where a step is executed. At the end of each step, which involves changes in the

particle energy and trajectory, the state of the particle is updated and a new step is calculated. As a result, the particle is transported step by step. This chain is iterated until the particle is absorbed, escapes from the simulation boundaries, or its energy goes below the energy cut-off. Since the cross-sections change by the continued loss of energy, the size of step should be small, where all relevant cross-sections are approximately constant during the step. However, this will increase the computation time.

Finally, it is important to emphasise that GEANT4 is a toolkit, where the users must create their own code using the libraries supplied and the tools distributed with the source code. Therefore, the users must set up a main() programme, which includes all outstanding classes, this is known as the main file, where the simulation starts. This main file is compulsory and it is the file from which all other classes are called and used. GEANT4 consists of several classes, three of them are mandatory and the users must include these classes in the code. The compulsory classes are the detector construction class (G4VUserDetectorConstruction), the primary generation action (G4UserPrimaryGenerationAction) and the physics list class (G4UserPhysicsList). In addition to these three classes, there are another five optional classes, which allow the users to modify the default behaviour of GEANT4. These classes are the run action class (G4UserRunAction), the event action class (G4UserEventAction), the stacking action class (G4UserStackingAction), the tracking action class (G4UserTrackingAction) and the stepping action class (G4UserSteppingAction).

3.3.2 GEANT4 classes

3.3.2.1 Mandatory classes

1. **Detector construction**

   The G4UserDetectorConstruction class is used to specify the geometry of the setup (shape, size and position) and to define the material composition of all components in this simulated setup. The materials are defined as a function of different elements, which are identified by their atomic number (Z), mass (A) and density. Moreover, isotopes can also be defined and it is also possible to assign a temperature, pressure, and state (solid, liquid or gaseous) to each material. It should be taken into consideration that, though any material can be defined in GEANT4, the users have to ensure that both cross-section data and physics models are updated with a correct performance of the simulated elements over the energy range of interest.

2. **Primary generator action**

   The G4UserPrimaryGeneratorAction class determines the particle source, where it requires the user to define the initial event state or the radiation source via an event generator. The radiation source has to be modeled as realistic as possible since the results from simulations depend strongly on the irradiation configuration. Also, in this class a source with different shapes can be defined by the general particle source (GPS) component, including 2D and 3D surfaces such as disks, spheres or boxes. The angular distribution of the particles can also be defined. The energy of the radiation source can be defined as mono-energetic or with an energy spectrum.

3. **Physics list**

   The G4UserPhysicsList allows the users to assign physical processes and to define all the physical models, which will take place in the simulation as well as the energy cut-off and the associated cross-sections. The process in GEANT4, is a class which illustrates how and when a specific type of physical interaction takes place along the particle track, while the model is another class whose methods execute the details of this interaction. GEANT4 describes the physical interactions with complementary and alternative physics models in an energy range that could be from thermal neutron interactions to high energy for cosmic rays physics. Therefore, GEANT4 gives the flexibility to the users to choose the appropriate set of models for a given process depending on the simulated setup, the particle type and the energy range.

3.3.2.2 Optional classes

1. **Run action**

   The G4UserRunAction controls the actions in the beginning and end of each run. It has three virtual methods that are called through the G4RunManager class for each run. These methods are GenerateRun(), BeginOfRunAction() and EndOfRunAction().

2. **Event action**

   The G4UserEventAction is for the beginning and end of each event. Its virtual methods are BeginOfEventAction() and EndOfEventAction(), which are invoked through G4EventManager class for each event. It is normally used to initialise and fill the generated histograms.

3. **Stacking action**

   The G4UserStackingAction is for customising access to the track stacks, where it allows giving the priority to the selected secondary particles in which the user is interested.

4. **Tracking action**

   The G4UserTrackingAction is for actions at the creation and completion of every track.

5. **Stepping action**

   The G4UserSteppingAction is for customising the behaviour at every step and to control the progress of each step. It is also useful to control the physical processes which take place in specific positions (surfaces, volumes or regions).

In order to carry out the whole GEANT4 simulations, there are some technical requirements which are necessary to run the simulations. These requirements are a Linux operating system with g++ to compile C++ codes, the CLHEP library that contains the basic physics class which are derived from events generated by Monte Carlo in C++, the STL library for general purpose which contains generic algorithms and data structures, a GNU-make system which is a software that builds executable programs and libraries from the source code by reading the makefiles, where it is indicated how to carry out the main program and the source code of GEANT4 with the input files of the user's code. It is also important to note that although GEANT4 is a powerful toolkit with a lot of advantage, it has some disadvantages. For instance, the GEANT4 complex structure, where there is a huge quantity of G4-options which affect the learning time of the user. In addition, GEANT4 requires more computational resources than other codes, which were particularly designed for some specific application. Therefore, MCNP simulations are much more simpler than GEANT4 simulations.

Overall, GEANT4 and MCNP simulation packages have been utilised in this work (i) to study the optimum thermal neutron converter thickness and its effect on the detection efficiency of the detector, (ii) to investigate different experimental setups, which affect the neutron flux through the converter volume. The simulations setup and their results will be addressed in the following chapters, where they will be compared with the experimental measurements.

Chapter 4

Simulation & validation of single sandwich detector configuration

4.1 Introduction

A series of GEANT4 simulations were performed to predict the properties of a planar converter layer in a sandwich detector configuration, which consists of two silicon sensors. This planar converter geometry has an optimal thickness when the thermal neutron detection efficiency is the highest. The determination of this thickness is the main aim of these simulations depending on the range of the neutron capture products in both ^{6}LiF film and ^{6}Li foil, which are used as neutron converter materials in this study. The simulations are carried out using GEANT4 codes. These codes are described in appendix C "GEANT4 codes".

Furthermore, this Chapter describes the experiments, where the sandwich detector configuration was tested in order to validate the simulation results. The experimental measurements are carried out in front of an isotropic ^{241}Am-^{9}Be neutron source to examine the thermal neutron detection efficiency of a single sandwich detector. The gamma-ray rejection factor of the detector is determined based on the measurements, which have been taken in front of ^{60}Co gamma-ray source. A method is proposed to differentiate neutron events from the background gamma radiation. This method depends on both the Pulse Height Discrimination (PHD) and the detection of coincidence. The results show that the neutron detection system, GAMBE, is capable to function as an effective thermal neutron detector.

4.2 Detector performance

4.2.1 Sandwich detector configuration

The sandwich detector configuration has been chosen to overcome the geometric limitations of the planar detector design, which have been discussed in section 2.5.2. The sandwich design leads to almost 4π collection of the primary reaction products in both directions, as fig. 4.1 shows. As a result, this sandwich configuration enhances the thermal neutron detection efficiency of the detector. Moreover, the charged particle reaction products such as alpha and triton particles can be detected in coincidence and this improves the discrimination against the background gamma radiation. It was noted that the maximum thermal neutron detection efficiency was 13% for a sandwich of double inward coated device using 4 μm thick of ^{10}B and 30 μm thick ^{6}LiF [77].

The thermal neutron detection efficiency of the sandwich configuration will be investigated using GEANT4 simulations. In these simulations, ^{6}Li will be examined as a neutron converter material in the form of a ^{6}LiF film or a ^{6}Li foil. There are four factors which will influence the detection efficiency of the thermal neutron detector, GAMBE. These factors are the neutron capture probability, the range of the emitted charged particles through the converter film/foil, the density and thickness of the converter layer.

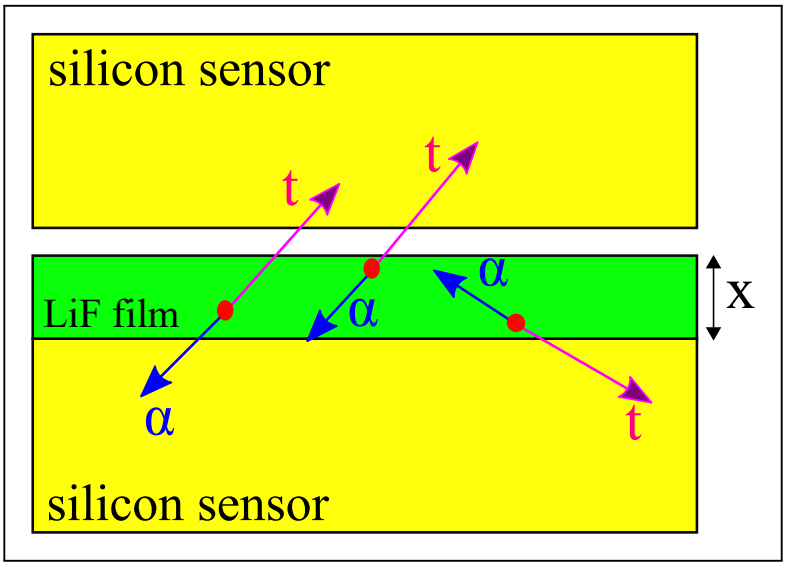

Figure 4.1: Principle of neutron detection using sandwich detector configuration of two silicon sensors. As an example is shown the reaction of thermal neutrons on ^{6}LiF film.

4.2.2 Simulation parameters

The geometric structure of the sandwich detector configuration consists of two silicon sensors. Each of them has a thickness of 300 μm and an area of 1 $\times$ 1 cm^2. There is also a 100 nm Al contact, which covers the surface area of both silicon sensors. The variable parameters in the simulations are the thickness of the converter layer and its composition (^{6}LiF or ^{6}Li). Figure 4.2 shows a sketch of the simulated geometry. The geometry started by setting the world, which is centred around (0,0,0) and contains everything else. In this world, the volumes and the materials of the diodes, contacts and converter film/foil are defined. In order to simulate the real sandwich detector design, an air gap 300 μm thick is assigned between the converter ^{6}LiF film and the silicon sensor B (see fig. 4.2b). In case of pure ^{6}Li metal as a neutron sensitive material, the foil is suspended between both silicon sensors, where there is an argon gap 300 μm thick between the ^{6}Li foil and both sensors (see fig. 4.2a). The thickness of the neutron converter film/foil will be changed in the direction of x-axis as specified in appendix C.1 "the detector construction class".

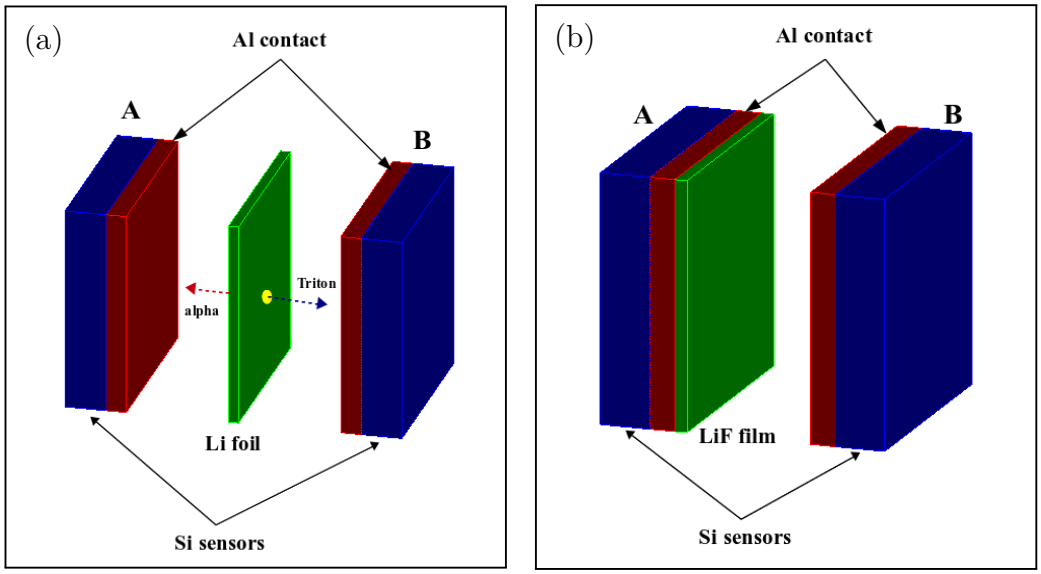

Figure 4.2: GAMBE, thermal neutron detector consisting of two Si sensors in a sandwich configuration with (a) ^{6}Li foil and (b) ^{6}LiF film.

The simulation starts by assigning a position randomly within the converter volume, where a thermal neutron can be captured. From this position, one alpha is assigned an arbitrary direction with an energy of 2.05 MeV and a triton is assigned the opposite direction with an energy of 2.73 MeV (see appendix C.2 "the primary generator action class" and fig. 4.2a). This model assumes that neutron capture is distributed uniformly within the ^{6}LiF film or the ^{6}Li foil. This

is a good approximation to study the effect of the converter layer thickness on the range of the charged particle reaction products through the whole area and volume of the neutron sensitive material. The probability of the thermal neutron absorption is assumed to be constant over the entire area of the converter film/foil. The energy deposited by each charged particle reaction product (alpha or triton) in each of the two silicon sensors is measured as specified in appendix C.3 "the stepping action class".

4.2.3 Thermal neutron detection efficiency

The thermal neutron detection efficiency, ε_n, of the sandwich detector configuration with a planar converter layer can be derived from the product of two probabilities as shown in eq. (4.1). The first is the detection probability of the charged particle reaction products, $\varepsilon_{det} = \frac{n}{N}$, which is defined as the ratio of the detected charged particles (n) by the Si sensors to the number of captured neutrons (N) within the converter volume. This ratio is affected by the solid angles of these charged particles via the converter layer towards the silicon sensors and the converter thickness, x (see fig. 4.1). The second is the neutron capture probability, $\varepsilon_{abs} = 1 - P(x)$, within the converter film/foil as a function of its thickness, where $P(x)$ is the neutron escape probability [13].

$$\varepsilon_n = \varepsilon_{det} \times \varepsilon_{abs} = \frac{n}{N} \times \{1 - P(x)\} \tag{4.1}$$

The absorption probability ε_{abs} is proportional to the initial neutron flux ($I_\circ$) through the thickness of the neutron converter. The transmitted neutron flux (I_x) through thickness, x, is described by

$$I_x = I_\circ \times P(x) = I_\circ \times exp(-\frac{N_A}{w_A} \times \rho \times \sigma \times x), \tag{4.2}$$

where N_A is Avogadro's number, w_A the atomic or molecular weight of the reactive film/foil, ρ the density of the reactive film/foil and σ is the thermal-neutron absorption cross-section of ^{6}Li, 940 b. It is clear that the fraction of neutrons passing through the converter layer of thickness, x, without any interaction is

$$P(x) = \frac{I_x}{I_\circ} = exp(-\frac{N_A}{w_A} \times \rho \times \sigma \times x). \tag{4.3}$$

Therefore, the second term in eq. (4.1) of the thermal neutron detection efficiency, which represents the absorption probability, ε_{abs}, as a function of the converter

thickness, x, is defined as following

$$\varepsilon_{abs} = 1 - P(x) = 1 - exp(-\frac{N_A}{w_A} \times \rho \times \sigma \times x). \tag{4.4}$$

Finally, the thermal neutron detection efficiency, ε_n, of the detector is determined using eq. (4.5), as defined in appendix C.4 "the run action class".

$$\varepsilon_n = \frac{n}{N} \times \{1 - exp(-\frac{N_A}{w_A} \times \rho \times \sigma \times x)\} \tag{4.5}$$

A neutron is counted by detecting either an alpha or a triton as a single or/and a coincident event. This is defined as the total detection efficiency of the detector (ε_{tn}). Detecting neutron capture products in coincidence is a method based on detection of both reaction products (alpha and triton) by two Si sensors and, thus, the coincidence detection efficiency (ε_{cn}) of the detector can be defined. These coincidences provide a very good method for rejecting the spurious hits coming from gamma-ray, which are usually present in a neutron field. However, the price to pay is a reduction of the thermal neutron detection efficiency of the detector.

As illustrated, the detection efficiency depends on both the probability that a neutron is captured and the chance that secondary particles created in the ^{6}LiF film or the ^{6}Li foil are capable of reaching the sensitive detector volume, where they can leave a detectable amount of energy. Therefore, the total (ε_{tn}) and coincidence (ε_{cn}) detection efficiency increases up to a certain value of the converter film/foil thickness after which it will decrease as the secondary particles are stopped and lost inside the converter layer. The results obtained from the simulations indicate that the optimal ^{6}LiF film thicknesses for the highest total and coincidence detection efficiency of 7.5% and 1.1% are 35 and 5 μm respectively as presented in fig. 4.3.

In the case of using ^{6}Li foil as a neutron converter material, the simulations show that the range of ^{6}Li foil thicknesses, which affect the thermal neutron detection efficiency of the detector surpasses that of ^{6}LiF film as can be seen in fig. 4.4. This figure illustrates the influence of the converter density on the total and coincidence detection efficiencies of the detector. As discussed in section 2.5.1, the lower the converter density is, the higher the range of the charged particle reaction products will be. For ^{6}Li foil as a neutron converter material, the sandwich detector configuration will be able to achieve the highest total (ε_{tn}) and coincidence (ε_{cn}) detection efficiencies of 19% and 3.1% corresponding to a higher converter thickness of 120 and 20 μm respectively. However, the chemical degradation of ^{6}Li remains a major problem which will limit its usage as a neutron sensitive material

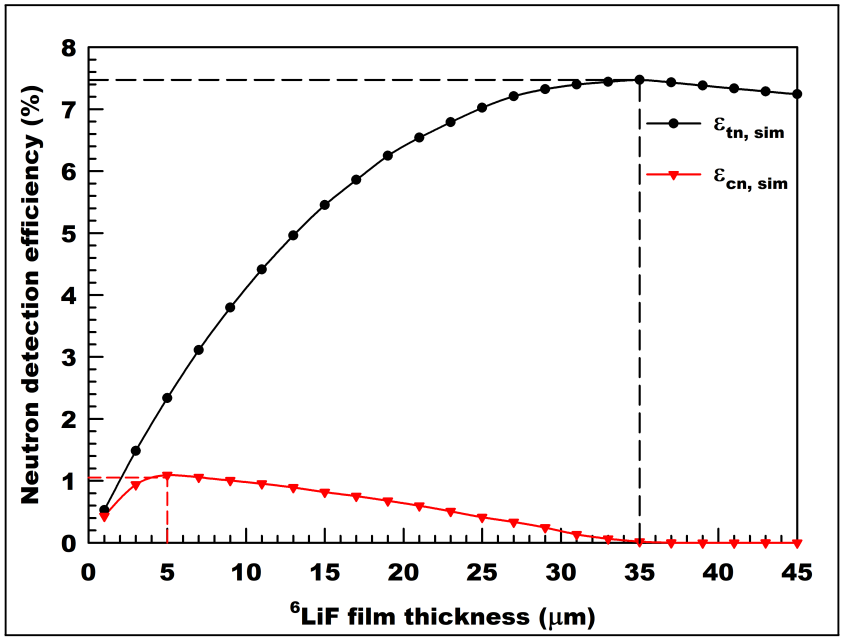

Figure 4.3: Dependencies of the total (ε_{tn}) and coincidence (ε_{cn}) detection efficiencies as a function of the neutron converter ^{6}LiF film thickness. The chart shows an optimal thickness at which ε_{tn} and ε_{cn} are highest.

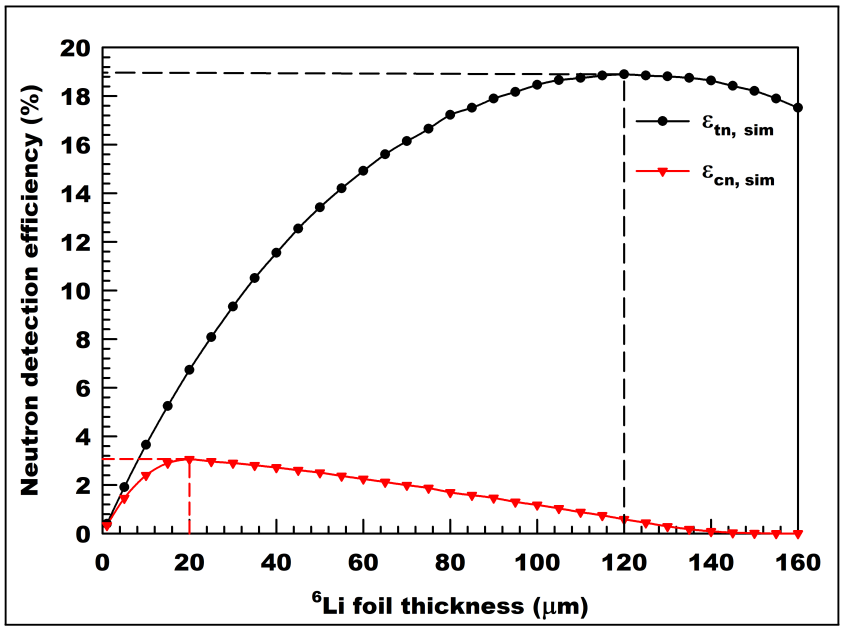

Figure 4.4: Variation of the total (ε_{tn}) and coincidence (ε_{cn}) detection efficiencies as a function of the neutron converter ^{6}Li foil thickness. The highest ε_{tn} and ε_{cn} are presented corresponding to the optimal pure ^{6}Li foil thickness.

for the purpose of the detection of thermal neutrons. This problem can be resolved by maintaining an inert environment to protect the ^{6}Li foil from corrosion as will be discussed later in the experimental work.

Finally, it has been observed that for both ^{6}LiF film and pure ^{6}Li foil, there is an optimal thickness where the detector can achieve the highest total (ε_{tn}) and coincidence (ε_{cn}) detection efficiencies. Hence, if the thickness of the converter film/foil increases beyond the optimum value, the detection efficiency of the detector decreases. As the charged particles interaction probability in the sensitive silicon sensors declines due to the energy loss in the converter film/foil itself. In addition, there is another factor, which can affect the optimal thickness of the neutron converter film/foil and as a result the detection efficiency will also be affected. This factor is the PHD, which defines the minimum detectable amount of energy by both silicon sensors of the detector. If this PHD is lowered, then the minimum detectable energy is less, which allows for longer effective ranges for both alpha and triton particles via the converter film/foil. Hence, a thicker layer of the converter can be used and, thus, the detection efficiency increases. Since the range of the charged particle reaction products is a function of the applied PHD the optimal neutron converter thickness will also change as a function of the PHD setting.

Figure 4.5 shows the expected total and coincidence detection efficiencies both for ^{6}LiF and ^{6}Li coated devices as a function of the applied PHD. As can be seen simply reducing the PHD value to 100 keV can increase the detection efficiency. However, the risk of including background gamma radiation events increases as the PHD is lowered [105]. Also, it is important to note that the optimal ^{6}LiF film and ^{6}Li foil thickness will change as a function of the PHD as well. Therefore, prior knowledge of the radiation environment, where the detector will be used is important to design the optimum film/foil thickness for the detector.

4.2.3.1 Pulse height spectra of reaction products

The energy released from the neutron capture in ^{6}Li is several orders of magnitude (MeV) larger than the energy of the incident thermal neutron (meV). Hence, the thermal neutron detector with a ^{6}Li based neutron converter cannot measure the energy of the incident neutron. However, the pulse height spectrum of the energy deposited in the silicon sensors by the heavy charged particle reaction products is important, as it can be used to distinguish the thermal neutrons from background signals. The signals created by the neutron capture reaction products should be higher than the signals caused by the background gamma-ray which are frequently present in the neutron radiation field.

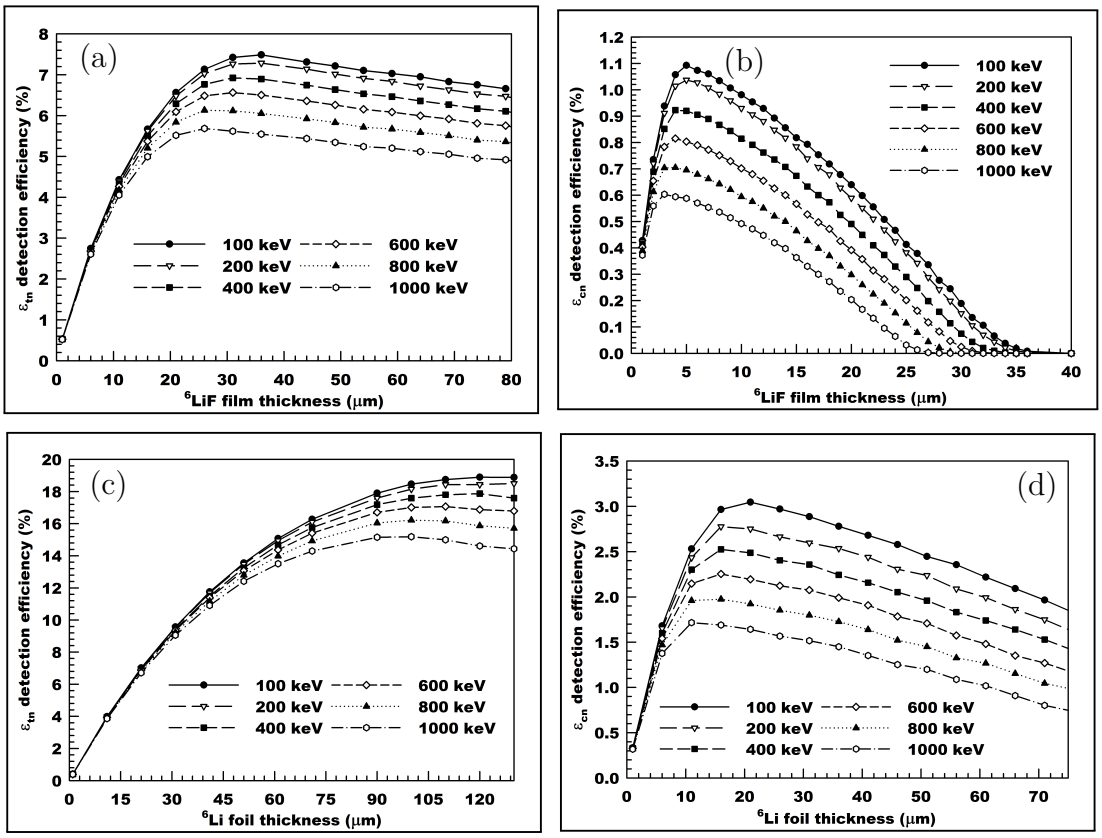

Figure 4.5: Dependency of the thermal neutron detection efficiency on the converter film/foil thickness as a function of the applied pulse height discriminator: (a) and (b) presents the total and coincidence detection efficiency of the detector using ^{6}LiF as a neutron converter film, as well as (c) and (d) for ^{6}Li as a neutron converter foil.

The charged particle reaction products created by the neutron capture in the converter volume have to travel through the converter and the detector metallic contacts until they reach the sensitive volume of the silicon semiconductor detector (depletion region). The charged particles lose part of their energy during their passage through these layers, the rest of their energy is deposited in the depleted region of the silicon sensors. The amount of energy deposited in the silicon sensors depends on the depth where the neutron capture takes place as well as the angle under which the charged particle travels towards the sensors. Therefore, the pulse height distribution of the deposited energy is a continuous spectrum.

Figure 4.6 presents the spectra of the deposited energy in both silicon sensors of the thermal neutron detector in a sandwich configuration (see fig. 4.2b) for two different ^{6}LiF film thicknesses, 5 and 1 μm. There are two main edges that corresponded to the energy deposited by the charged particles if the converter film is thick (fig. 4.6a) and two peaks if the converter film is thin (fig. 4.6b). One edge/peak corresponds to alpha particles with energy of 2.05 MeV and the second

is for the triton particles with energy of 2.72 MeV. Thus, the resolution of the detector depends on the thickness of the converter film. The thinner the converter film is, the better the resolution of the peak is, due to a lower energy straggling of the reaction products, when they reach the sensitive silicon sensors.

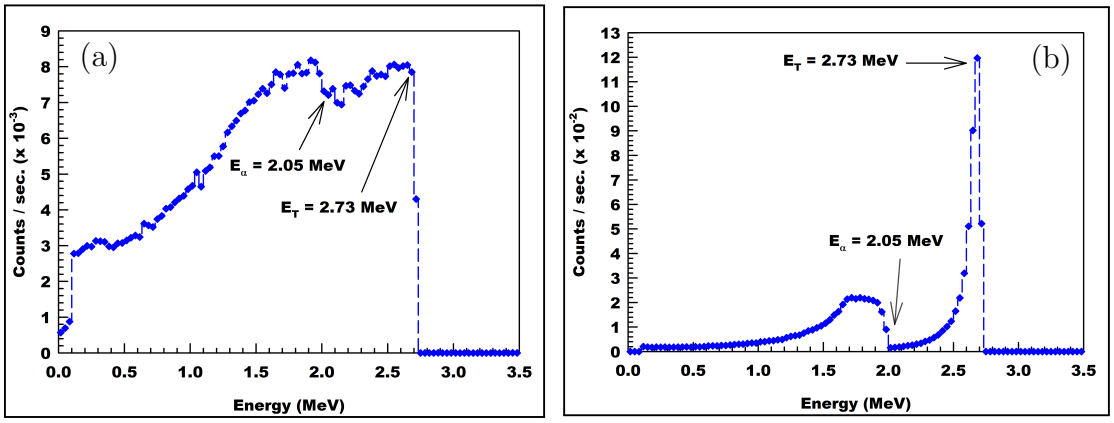

Figure 4.6: Spectrum of energy deposited in both sensitive silicon sensors of the detector with a ^{6}LiF film in a sandwich configuration: (a) the ^{6}LiF is 5 μm thick, (b) the ^{6}LiF is 1 μm thick.

Figure 4.7 shows the distribution of the energy deposited in sensor A with respect to the energy in sensor B for coincidence events. This figure can discriminate the true neutron events against the random spurious signals from background gamma radiation by defining a window, where the charged particle reaction products will release their energy. This window is defined by the dotted line which represents the energy from 1.5 MeV to 2.8 MeV, where any event in that region is classed as a good event, typical of a neutron induced alpha-triton pair. Moreover, the region below 1 MeV is to present the area, where there is an interference between events due to the interaction of the reaction products and gamma-ray with the silicon sensors. The advantage of this coincidence feature of the detector is also affected by the thickness of the converter film as can be seen in figs. 4.7a and 4.7b for 5 and 1 μm thick converter film, respectively. In a thin converter film, the energy deposited in both silicon sensors for coincidence events will be higher, and hence the discrimination against the background radiation is better.

The result of the same simulation, but for a neutron converter made out of pure ^{6}Li is shown in fig. 4.8. This figure shows the advantage of using a ^{6}Li foil of 20 μm thick, which can achieve the maximum coincidence detection efficiency of 3.1% (see fig. 4.4). This specific thickness of the ^{6}Li foil also has a better peaks resolution (see fig. 4.8a) such as a ^{6}LiF film of 1 μm thick. This is due to the lower atomic density of pure ^{6}Li compared to that of the ^{6}LiF compound, which results in a larger reaction products range than that within the ^{6}LiF film.

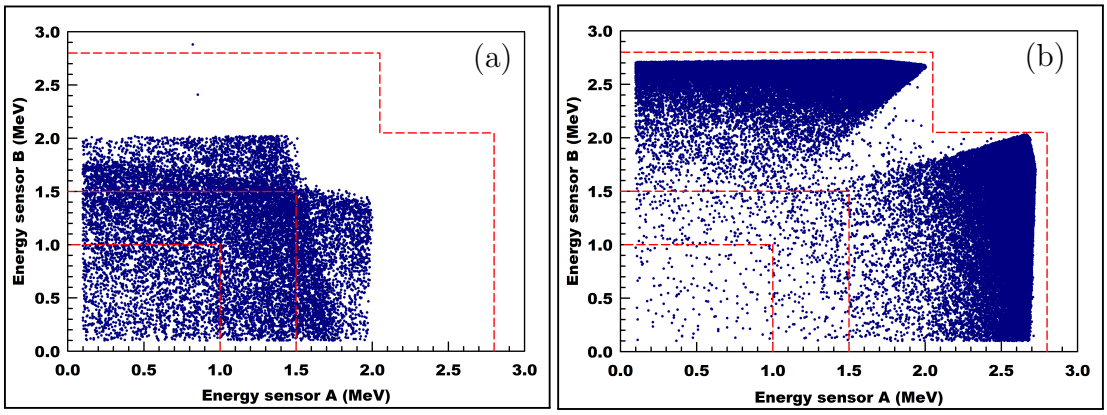

Figure 4.7: Detected events in both silicon sensors of the detector as coincidences corresponding to a ^{6}LiF film as a neutron converter of (a) 5 μm thick and (b) 1 μm thick.

Interestingly, this ^{6}Li foil of 20 μm approximately allows half of those charged particle reaction products (48%) to be detected in coincidence, with 90% of the generated alpha-triton pairs having an energy higher than the discrimination limit of 1.5 MeV, as can be seen in fig. 4.8b. Therefore, recent developments are aimed at developing pure ^{6}Li as a neutron converter material. For instance, a foil of 100 μm thickness has the ability to capture nearly 43% of the incident thermal neutron flux. Moreover, they can still release charged particle reaction products, which are capable of depositing an average energy of 1 MeV in the adjacent semiconductor detector [66].

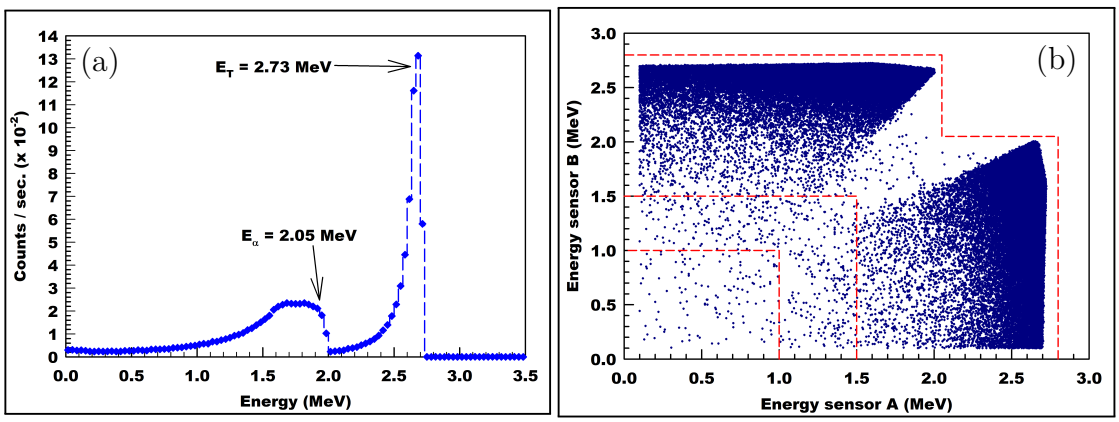

Figure 4.8: Pure ^{6}Li foil as a neutron converter in the detector: (a) the deposited energy spectrum in both silicon sensors of the detector for a converter foil thickness of 20 μm, (b) the detected charged particle reaction products as coincidences.

In conclusion the developed neutron detection system, GAMBE, in a sandwich configuration using two silicon sensors of 300 μm thick and an active area of 1×1 cm^2 can be efficiently used for the detection of thermal neutrons by using

^{6}LiF or ^{6}Li as a neutron converter layer. The aim of the simulation was to find the optimal converter thickness, where the detector can achieve the highest total (ε_{tn}) and coincidence (ε_{cn}) detection efficiencies. It has been shown that a ^{6}LiF film of 35 μm thick allows to achieve the highest total detection efficiency of 7.5%. On the other hand a ^{6}Li foil of 120 μm improves the detection efficiency of the detector up to 19%.

The coincidence detection efficiency is a developed feature of the detector to identify a thermal neutron through the detection of the induced reaction products (alpha and triton) at the same time by the silicon sensors. This method enhances the rejection factor of the detector against the electronic noise and the background gamma radiation, which usually exists in the neutron radiation field. It has been found that the maximum coincidence detection efficiency that can be achieved by the detector are 1.1% and 3.1% corresponding to an optimal converter thickness of 5 μm for ^{6}LiF film and 20 μm for ^{6}Li foil respectively. In addition, the theoretical investigation indicates that, ^{6}Li is more efficient as a neutron converter material than the stable ^{6}LiF. This is due to the enhancement of the resolution and the thermal neutron detection efficiency of GAMBE. However, the chemical reactivity of pure lithium-6 is still an issue, which limits it as a neutron converter material. Therefore, a protective design has been provided to the detector to protect the pure metallic foil from corrosion.

In the following section GAMBE in a sandwich detector configuration will be tested experimentally in order to validate the results of this theoretical study.

4.3 Experimental validation

4.3.1 Neutron flux characterisation and measurement

For characterisation purposes, the thermal neutron flux has been measured using a ^{3}He detector tube. The tube is placed 50 cm away from the end of the neutron tank, and the 1 Ci ^{241}Am-^{9}Be neutron source is 25 cm inside the water tank. This position is referred to as the calibration position, where GAMBE will be tested, and the whole setup is defined as the "Basic" layout, as presented in fig. 4.9. The ^{3}He detector tubes are industry standard 2 in. (5 cm) diameter, 36 in. active length tubes (90 cm), a pressure of 2 atm, and operating at a voltage of 1100 V. The typical thermal neutron detection efficiency of these ^{3}He detector tubes is $> 60\%$. Furthermore, the neutron sensitivity of these detectors is 236 cps/nv (nv is thermal neutron flux, neutrons/cm^{2}/s). This equals to approximately 3 cps/nv per cm of active tube length assuming there has been no degradation of the performance

over the lifetime of the detector.

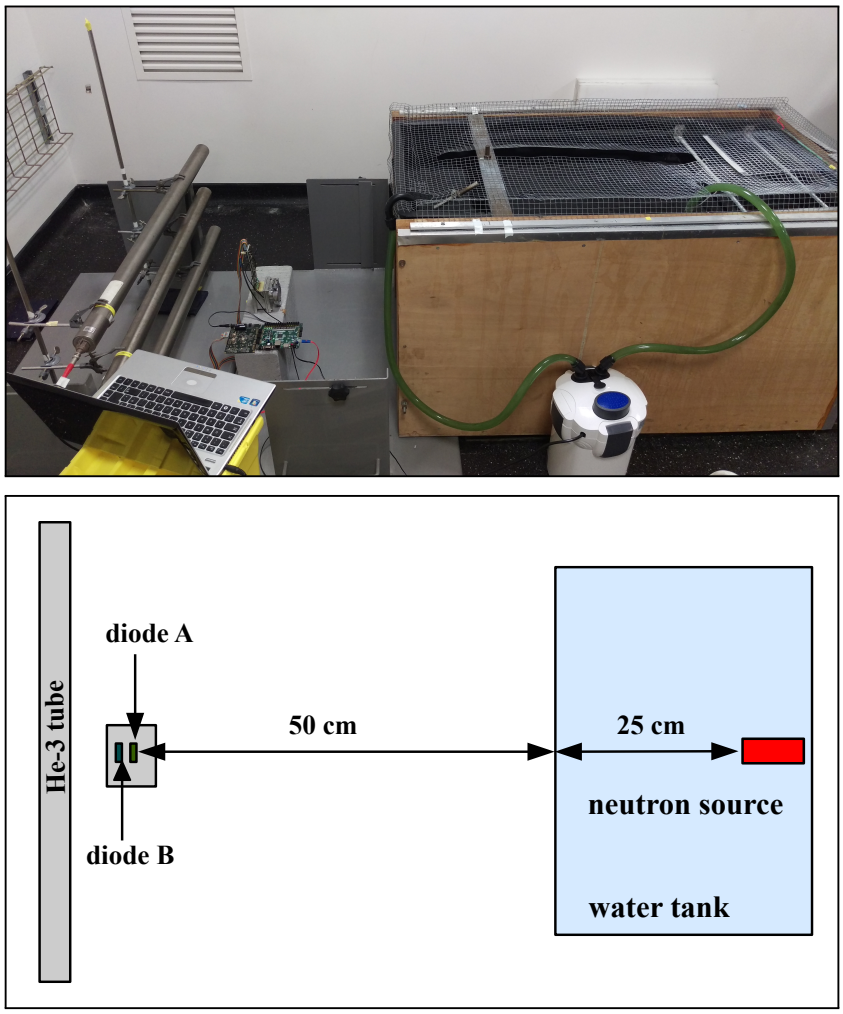

Figure 4.9: The calibration position with respect to the detector and ^{3}He detector tube, which refers to the "Basic" experiment layout.

Another detector, the NMS017NG3, John Caunt Scientific Ltd, neutron survey monitor, has been used to characterise the variation in the neutron flux along the length of the ^{3}He detector tube. This is a neutron survey monitor that provides ambient dose equivalent measurement from thermal to 14 MeV neutrons. The NMS017NG3 uses a SP9 ^{3}He neutron detector at its core. Moreover, it has various measurement modes, which include dose rate, accumulated dose, count rate and various count and time modes for integrated measurements. The sensitivity of this detector is 0.72 cps/μSvh^{-1} and its gamma rejection factor is 3000:1. The measurements of the thermal neutron flux along the length of the ^{3}He detector tube prove that the detector at the calibration position will be exposed to the maximum neutron flux which is 1.4 times greater than the average over the entire pipe as shown in fig. 4.10.

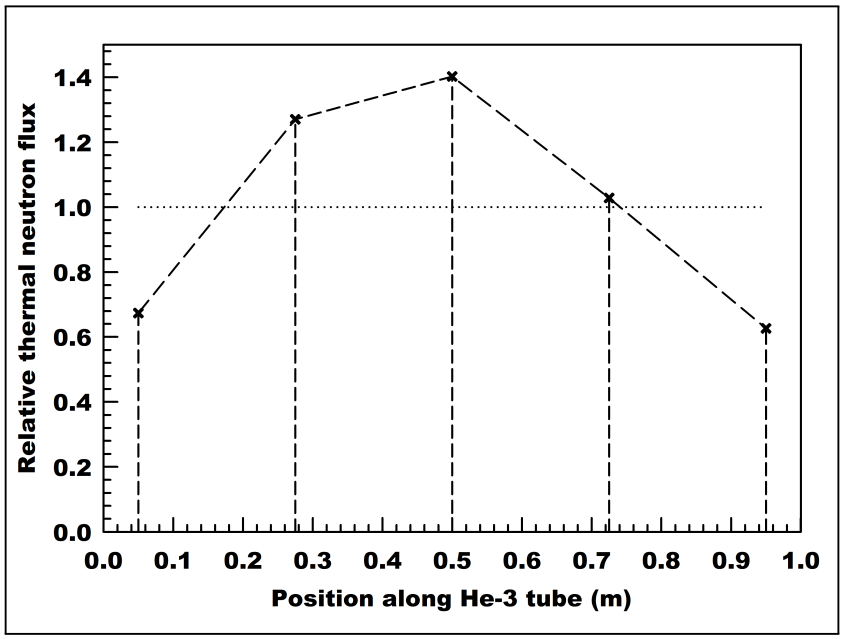

Figure 4.10: Variation of the thermal neutron flux along the ^{3}He detector tube.

4.3.2 Response to gamma-rays

The sensitivity of Si wafers to gamma-ray is expected to be low for thickness range of $30 - 300$ μm, although the detection efficiency is close to 100% for γ-ray energy of 10 keV, it falls to approximately 1% for 150 keV [106]. In addition, it has been reported that for γ-ray energies between 150 keV and 5 MeV, Compton scattering is the most probable mechanism for γ-ray interaction in that thickness range of Si sensors [106]. For instance, gamma quantum of 1 MeV can transfer maximum energy of 0.8 MeV to recoil electron which deposits 200 keV in 300 μm thick depletion region [70].

Therefore, silicon thickness should be kept to minimum to reduce the interaction probability of gamma-ray and to ensure good n/γ discrimination. The ideal active thickness should match the range of the reaction products in silicon, which is in the order of few microns. However, this will result in higher electronic noise due to the elevated capacitance. Consequently, the thickness of 300 μm is an optimal thickness to reduce the generated electronic noise, when fully depleted.

Two bare silicon sensors with an active area of 1 $\times$ 1 cm^2 have been used in sandwich configuration without any neutron converter material to count events from gamma-ray interactions with the sensors. Two different gamma-ray sources have been used to characterise the sensitivity and the efficiency to detect gamma radiation ($\varepsilon_{t\gamma}$), which is needed to estimate the gamma-ray rejection factor (γ_{rf}). The gamma-ray detection efficiency (ε_γ) is defined as the ratio of registered gamma events in either of the sensitive silicon volumes, $\sum n_{det}$, divided by the number of

incident gamma-ray (Φ_γ) on the detector as follows:

$$\varepsilon_\gamma = \frac{\sum n_{det}}{\Phi_\gamma} \times 100\% \tag{4.6}$$

Firstly, the bare detector has been examined using the ^{241}Am-^{9}Be neutron source where the detector was placed in the calibration position (see fig. 4.9). The exposure rate of the γ-ray in front of this 1 Ci neutron source is 1 mR/h per 10^6 n/sec. The neutron source produces gamma radiation of 60 keV, 2.26 MeV and 4.43 MeV, as discussed in section 2.1.1. The flux of the gamma rays (photon/cm^2/s) of 4.43 MeV and 60 keV was computed as a function of the thickness of the moderating water spheres [11]. Hence, the total gamma-ray flux corresponding to the "Basic" experimental setup is 10.5 γ/cm^2/s, where 1.85×10^6 photons penetrate the silicon sensors of the detector . Secondly, the detector has been tested by placing it 2 cm in front of a ^{60}Co gamma-ray source with an activity of 30 kBq. Based on the strength of the source and the source-detector geometry, $((1.51 \times 10^8) \pm (1.2 \times 10^4))$ photons were incident on the sensitive silicon sensors of the detector, over the entire run.

Figure 4.11 presents the deposited energy spectra as a function of the energy of the gamma-ray as observed from both the ^{241}Am-^{9}Be neutron source and the ^{60}Co gamma-ray source. All the detected gamma-ray have deposited an amount of their energy lower than 1 MeV in the silicon sensors of the detector. Therefore, the deposited energy is low relative to the energy which is deposited by a neutron induced triton of 2.75 MeV. This is particularly true for the ^{60}Co source which emits two gamma-ray of 1.17 and 1.33 MeV and even for the high energy gamma-ray of 4.4 MeV from the ^{241}Am-^{9}Be neutron source. Due to the fact that the high energy gamma-ray cannot fully be stopped through Compton scattering interaction (see section 2.6) in a 300 μm thick silicon sensor which has a low atomic number, Z = 14.

According to the PHD method, which is presented in fig. 4.12, no gamma radiation from either the ^{241}Am-^{9}Be neutron source or the ^{60}Co gamma-ray source will result in a neutron-like measurement for the observed coincidence events with energy higher than 1.5 MeV. Consequently, whatever gamma radiation energy hits the detector it will deposit a small fraction of its energy or it could be fully absorbed in the detector after having lost the majority of its energy through collisions with the surrounding medium. However, it has been observed in fig. 4.12 that there are few coincidence events, which have an energy more than 1.5 MeV. A possible explanation for this might be that the p-type silicon sensors are doped with boron, as described in appendix A.2. Therefore, there is a possibility that thermal

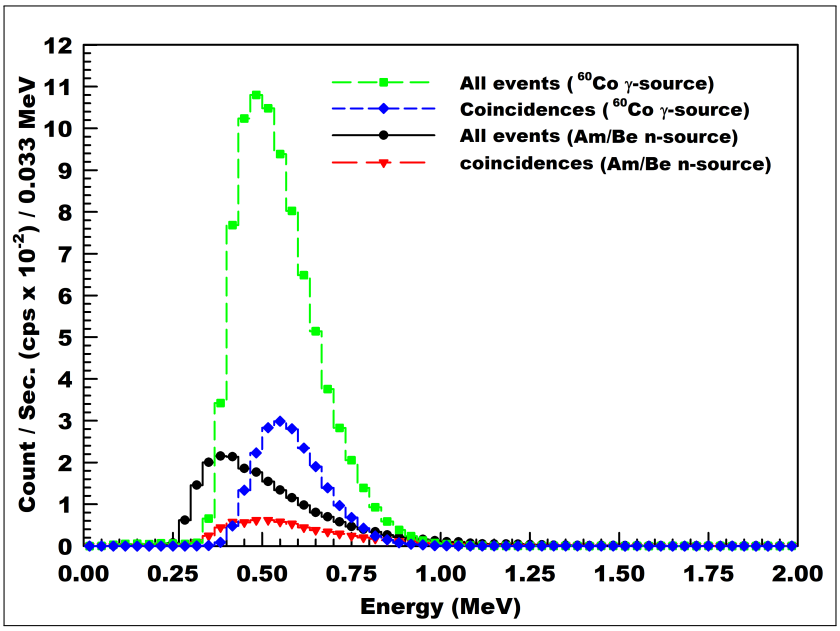

Figure 4.11: The spectrum of the deposited energy in both bare Si sensors of the detector, which has been used for the detection of gamma radiation emitted by ^{241}Am-^{9}Be neutron source and ^{60}Co gamma source.

neutrons can induce reactions with boron nuclei (see section 2.5.1) according to the following reactions:

$$^{10}\mathrm{B} + {}^{1}_{0}\mathrm{n} \longrightarrow {}^{7}\mathrm{Li}^{*}\,(\mathrm{at}\,1.015\,\mathrm{MeV}) + \alpha(\mathrm{at}\,1.777\,\mathrm{MeV})\;\mathrm{Q-value} = 2.792\,\mathrm{MeV},$$

$$^{10}\mathrm{B} + {}^{1}_{0}\mathrm{n} \longrightarrow {}^{7}\mathrm{Li}^{*}\,(\mathrm{at}\,0.84\,\mathrm{MeV}) + \alpha(\mathrm{at}\,1.47\,\mathrm{MeV})\;\mathrm{Q-value} = 2.31\,\mathrm{MeV}.$$

These reactions show that the amount of energy (Q-value) released in the silicon sensors is higher than the PHD of 1.5 MeV.

The gamma-ray rejection factor of the detector is determined based on the measurements using a ^{60}Co gamma-ray source, where 597 photons hit the detector per second, according to the geometrical efficiency. The rejection of background gamma-ray depends on the deposited energy in the detector due to the interaction of gamma-ray with the sensitive volume of the Si sensors of GAMBE. From fig. 4.13, it is apparent that the rejection factor of background gamma radiation (γ_{rf}) and the detection efficiency ($\varepsilon_{t\gamma}$ or $\varepsilon_{c\gamma}$) are affected by the variation of the applied PHD method. As can be seen in fig. 4.13 that gamma-ray detection efficiency of is severely reduced, as any contribution from gamma-ray will be rejected, when the PHD energy is greater than 0.75 MeV. As a result, GAMBE can achieve a high gamma-ray rejection factor of 10^{8}, so it could be used efficiently for the detection of thermal neutrons in a high background gamma radiation field.

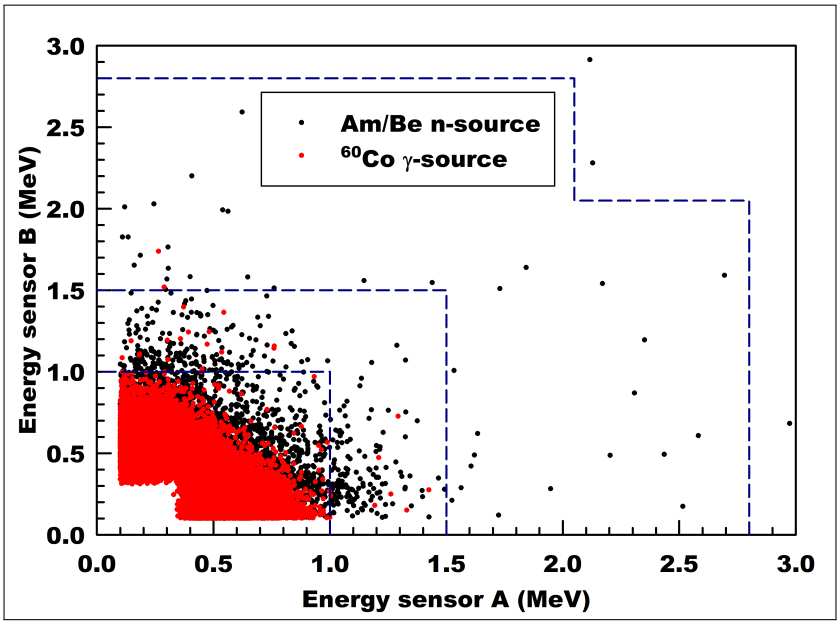

Figure 4.12: The observed coincidence events in both bare Si sensors due the interaction of gamma radiation, which emitted by an ^{241}Am-^{9}Be neutron source at the calibration position and a ^{60}Co gamma source 2 cm away from the detector.

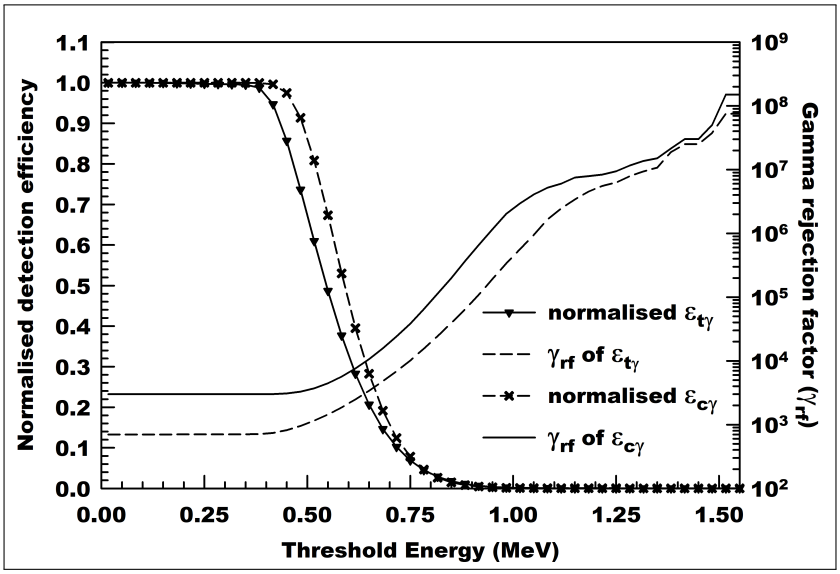

Figure 4.13: The effect of PHD method on both total ($\varepsilon_{t\gamma}$) and coincidence ($\varepsilon_{c\gamma}$) gamma-ray detection efficiency and the corresponding gamma-ray rejection factor.

4.3.3 Si semiconductor modification as a neutron detector

4.3.3.1 Coating with ^{6}LiF film

A 6 mol/l ^{6}LiF solution was prepared by dissolving 3 g of ball milled ^{6}LiF powder (Sigma-Aldrich 95% enriched ^{6}Li) in 20 cc ethanol. The ^{6}LiF solution was mixed with a ratio of 1:1 with a solution of 1 w/v% polyvinylpyrrolidone (Sigma-Aldrich PVP, MW 700000) in ethanol with a molar concentration of 1.43×10^{-4} mol/l, which is used as an adhesive material. This mixture of ^{6}LiF/PVP was precipitated on the surface of the Si sensor (total area of 1.25 × 1.25 cm^2). The mass of ^{6}LiF/PVP solution to be poured on Si sensor substrate is estimated as a function of the required ^{6}LiF film thickness as depicted in the following procedures.

1. The volume, V_f (cm^3), of the deposited ^{6}LiF/PVP film is determined as a function of the required film thickness, x (cm) and total area, A (cm^2), of the silicon sensor.

$$V_f = x \times A$$

$$V_f = \frac{M_f}{\rho_f}$$

   where M_f and ρ are the poured mass [g] and the combined density [g/cm^3] of the ^{6}LiF/PVP film respectively.

2. The mass, M_f, of the deposited film in grams as a function of its thickness, x, is determined by:

$$M_f = A \times x \times \rho_f$$

$$M_f = \frac{A \times x \times R \times \rho_{(LiF)} \times \rho_{(PVP)}}{(\rho_{(PVP)} \times R) + \rho_{(LiF)}}$$

3. The ratio, R, is wt/wt%, which is the weight of the ^{6}LiF/PVP after solvent evaporation to the precipitated ^{6}LiF/PVP solution:

$$R = \frac{W_2}{W_1}$$

   where W_1 & W_2 are the weights of deposited film before and after evaporation respectively.

4. The mass of ^{6}LiF/PVP solution in grams which should be applied to the sensor to achieve the required thickness, x, of the ^{6}LiF/PVP film is

$$W_3 = \frac{M_f}{R}$$

The mass of the poured solution was measured with a scale, where (2.4 ± 0.1) mg of the mixture was applied to the Si sensor to cover the whole surface area of 1.25×1.25 cm^2. This precipitated mixture was dried at room temperature to avoid cracks and to form a uniform film over the area of Si substrate. In order to characterise the surface roughness of the deposited film, an Atomic Force Microscope (AFM) and a scanning Keyence VHX5000 Digital Microscope (KVDM) were used. It was found by using the AFM that the precipitated ^{6}LiF film on the silicon sensor is not uniformly distributed and has a surface roughness of 2.5 μm. This results in an error in the mass distribution of ± 0.6 mg/cm^2 over the whole area of the formed ^{6}LiF film. Consequently, the determined thickness of the precipitated ^{6}LiF film is (1.5 ± 0.6) mg/cm^2. Furthermore, fig. 4.14 shows a 3D image of the precipitated film, which was taken by using the KVDM.

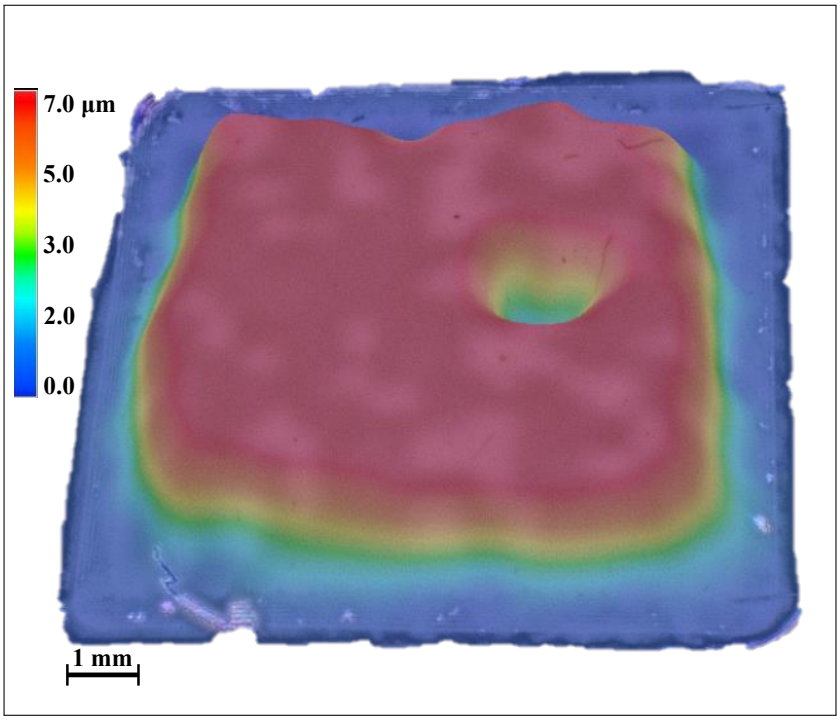

Figure 4.14: 3D image of the ^{6}LiF film thickness over the whole area of the silicon sensor by (KVDM), where the blue and red colours show the thinnest and the thickest part of the film respectively.

Experimental measurements have been performed using this precipitated ^{6}LiF film (1.5 ± 0.6) mg/cm^2 thick in the sandwich detector configuration. These measurements have been accomplished to examine the thermal neutron detection efficiency of the detector at the calibration position related to the "Basic" layout experiment (see fig. 4.9). The entire sensor-converter configuration was mounted in an aluminium box (inner dimension $60 \times 50 \times 30$ mm^3) designed to eliminate the pick-up noise. Since the semiconductor materials are in most cases transparent

to neutrons, which follow the exponential attenuation law when passing through the converter layer. It is possible to irradiate the whole detector structure from the backside, while neutrons pass through the silicon sensor first and are then captured using the converter film. Therefore, the coated Si sensor is facing the neutron source as it will be back irradiated. Indeed, a high proportion of neutrons are captured close to the boundary between the semiconductor detector and ^{6}LiF film. Consequently, the probability that charged particle reaction products will reach the sensitive silicon sensor is higher. Moreover, if the neutron is captured closer to the other side of the converter film, these charged particles will be detected by the other silicon sensor in the sandwich configuration. As a result, the total thermal neutron detection efficiency increases.

4.3.3.2 Coupling with pure ^{6}Li foil

Lithium metal (Sigma-Aldrich 92% enriched ^{6}Li) was cold-rolled into thin (40 ± 10) and (70 ± 10) μm foils, using a stainless steel rolling apparatus inside an argon glove-box. These thicknesses can be expressed in terms of the thickness unit as (1.8 ± 0.5) and (3.2 ± 0.5) mg/cm^2 respectively. The simulations indicate that the optimal thickness of a ^{6}Li foil for observing the reaction products (alpha-triton particles) in coincidence is 20 μm. However, it was not possible to achieve a foil with a thickness less than 40 μm as any attempts to create thinner foil resulted in tears in the foil.

Due to the highly reactive nature of the ^{6}Li metal, care has to be taken in order to maintain an inert environment for the foil to prevent corrosion. Therefore, the ^{6}Li foil was mounted between the two silicon sensors with a gap of 300 μm, while the whole structure remains inside the protective environment of the argon-filled enclosure of the glove-box. The entire lithium-sensor configuration was mounted and sealed within the airtight aluminium enclosure, which provided the detector with an inert environment to protect the neutron converter foil. The detector was tested in front of the neutron source according to the "Basic" experiment setup (see fig. 4.9).

4.3.4 GAMBE detection efficiency

The results presented here are all for measurements that have been taken in front of an isotropic ^{241}Am-^{9}Be neutron source at the calibration position as defined previously. The sandwich detector configuration has been tested using a ^{6}LiF film of (1.5 ± 0.6) mg/cm^2 thick as the neutron converter material. It also has been examined with a ^{6}Li foil of (40 ± 10) and (70 ± 10) μm thick as a

neutron converter layer. These experimental results are an essential step in order to validate the GEANT4 simulation results.

The thermal neutron detection efficiency of the sandwich detector configuration is assessed after subtracting all events belonging to gamma-ray interaction within the silicon sensor of the detector (see fig. 4.11). This contribution affects the count rate (counts/second (cps)) of the total (n_t) and coincidence (n_c) events related to thermal neutron, especially in the low energy range (< 1 MeV), as can be seen in figs. 4.15 and 4.16 for both ^{6}LiF film and ^{6}Li foil respectively. In this energy range there is a possibility of a convoluted signal due to α-particles and γ-rays. Therefore, the subtraction of the gamma-ray events ensures that the evaluated detection efficiency is an absolute thermal neutron detection efficiency.

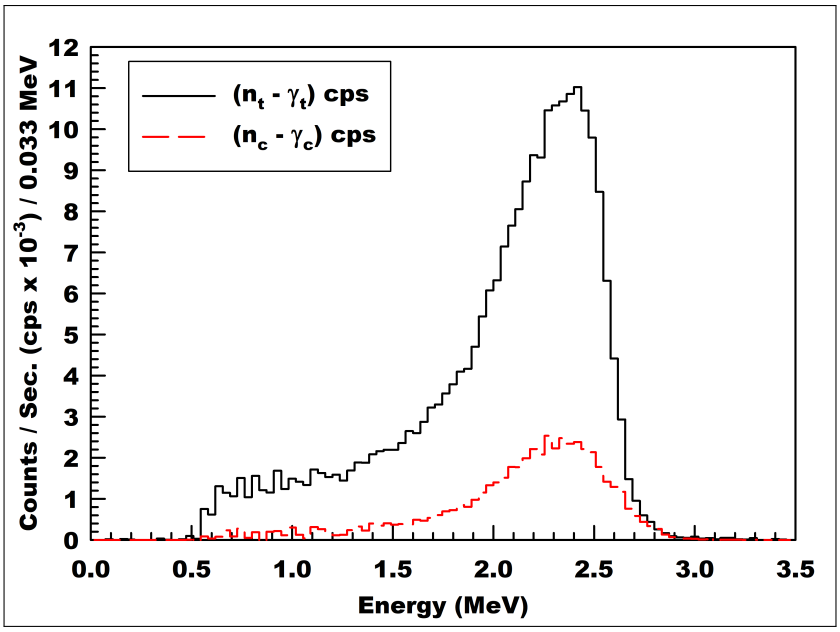

Figure 4.15: Spectra of energy deposited in both Si sensors of the detector as a function of a ^{6}LiF film (1.5 ± 0.6) mg/cm^2 thick.

In addition, these measured spectra show that the resolution behaviour of the detector is in accordance with the predicted behaviour as a function of the converter thickness. The spectra in figs. 4.16a and 4.16b show the effect of the converter thickness on the resolution of the detector. The thicker the foil, the worse the resolution due to the increased energy loss of the charged particle reaction products, which are transmitted through the converter foil in order to interact with the sensitive silicon sensors of the detector. However, the thicker foil has a higher count rate (cps). This is due to the triton particles, which have an energy of 2.73 MeV and are more likely to traverse through the neutron converter film/foil than the alpha particles of 2.05 MeV. Hence, the highest count rate is due to the triton particles, while the tail of the peak is related to the alpha particles.

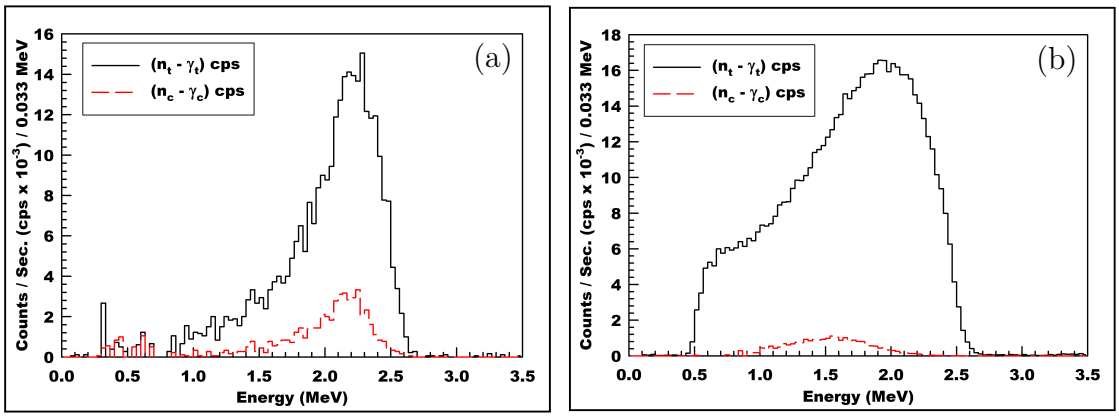

Figure 4.16: Spectra of energy deposited in both Si sensors of the detector as a function of a pure ^{6}Li foil of (a) (40 $\pm$ 10) μm thick, (b) (70 $\pm$ 10) μm thick.

The experimental results also show that a ^{6}LiF film of (1.5 $\pm$ 0.6) mg/cm^2 thick in the sandwich detector configuration can achieve a total and a coincidence detection efficiency of (4.1 $\pm$ 0.5)% and (0.9 $\pm$ 0.3)% respectively. The detection efficiency has been determined by integrating the area under the curve for both total and coincidence events and then dividing the results by the neutron flux (n/cm^2/s) through the converter film. The detection efficiency of the sandwich detector configuration was compared with the results of the theoretical investigation. As can be seen in fig. 4.17, the experimental total and coincidence detection efficiencies are in agreement with the predicted values.

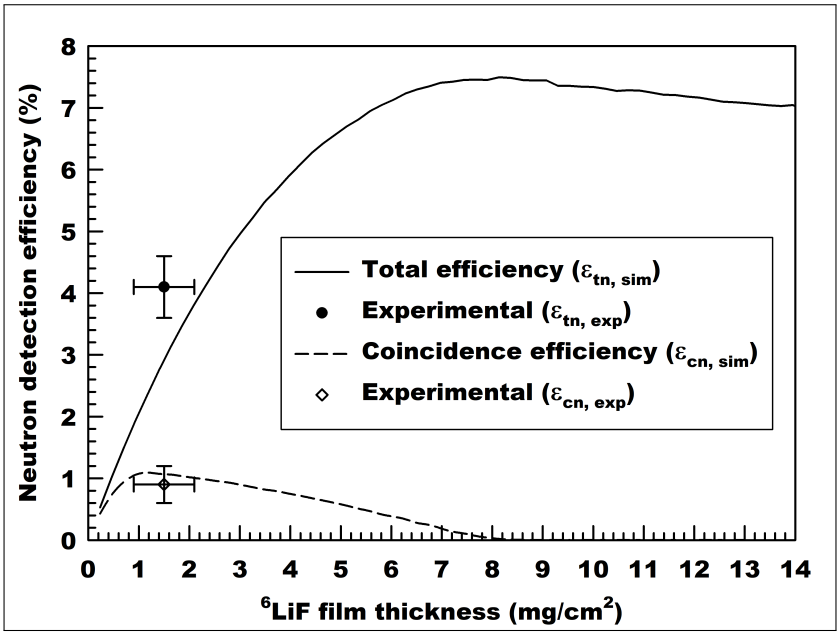

Figure 4.17: The experimental total and coincidence detection efficiency of a ^{6}LiF film (1.5 $\pm$ 0.6) mg/cm^2 thick compared to the predicted detection efficiency.

The results obtained from testing both ^{6}Li foils of (40 ± 10) and (70 ± 10) μm thick show that the total (ε_{tn}) and the coincidence (ε_{cn}) detection efficiency of the sandwich detector configuration are affected by the variation of the converter foil thickness, as expected and presented in fig. 4.18. The increase of the ^{6}Li foil thickness form 40 to 70 μm improves the total detection efficiency of the detector from (9.2 ± 1.4)% to (14.5 ± 2.2)% due to the increment of the neutron capture efficiency of the converter foil, whilst the charged particle reaction products are still capable of interaction with the silicon sensors. However, this change in thickness has a negative effect on the coincidence detection efficiency. The efficiency of the sandwich configuration to count a neutron based on the detection of the reaction products in coincidence reduces from (1.5 ± 0.9)% to (0.5 ± 0.3)%.

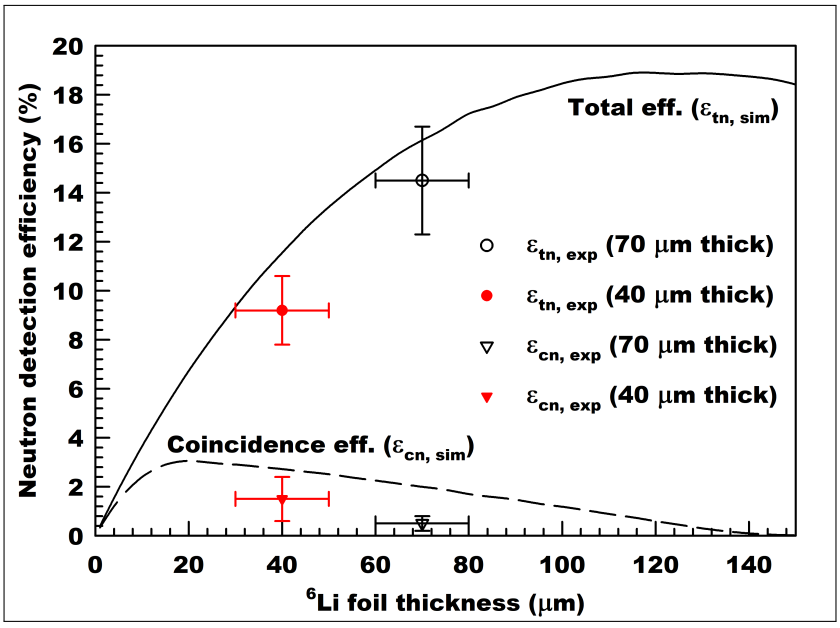

Figure 4.18: The experimental total and coincidence detection efficiency of a ^{6}Li foil ((40 ± 10) and (70 ± 10) μm) thick compared to the predicted thermal neutron detection efficiency as a function of the converter foil thickness.

Figures 4.19 and 4.20 present the observed coincidence events in both silicon sensors of the detector as a function of the energy deposited in sensor A against the energy stored in sensor B for different neutron converter materials. Experimental measurements illustrate that any background gamma radiation existing in the neutron radiation field is only capable of producing coincidence events in a defined region with an energy lower than 1 MeV, as can be observed in figs. 4.12 and 4.19. The energy of these coincidence events are independent of the energy of the background gamma radiation. Therefore, any event in the defined region from 1.5 MeV to 2.8 MeV is classed as a good event, typical of a neutron induced alpha-triton pair.

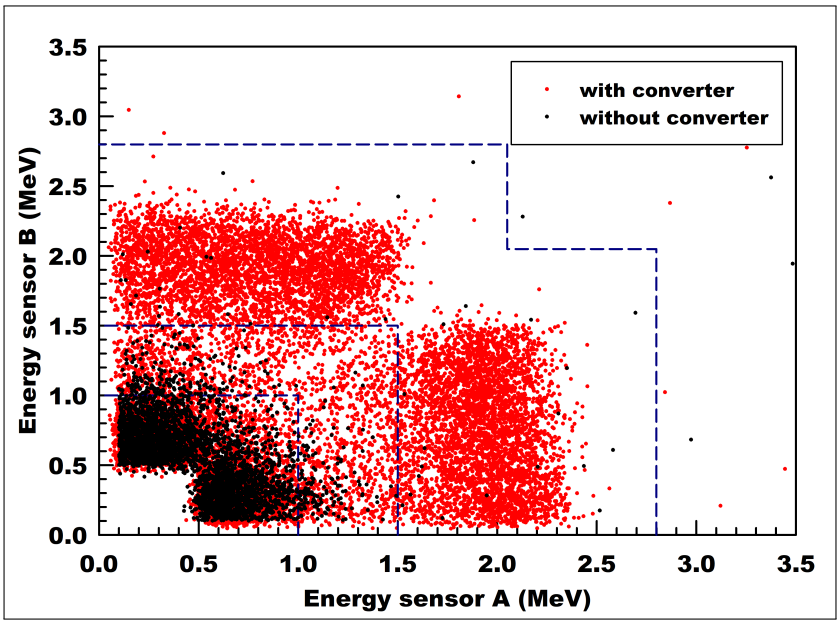

Figure 4.19: The pulse height of the observed coincidence events in both Si sensors of the detector as a function of a ^{6}LiF film (1.5 $\pm$ 0.6) mg/cm^2 thick.

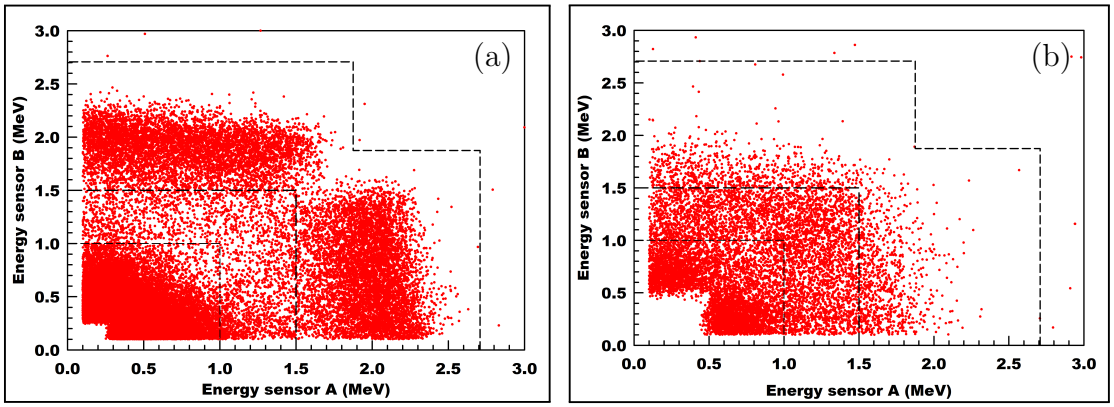

Figure 4.20: The pulse height of the observed coincidence events in both Si sensors of the detector as a function of a ^{6}Li foil: (a) (40 $\pm$ 10) μm thick, (b) (70 $\pm$ 10) μm thick.

The feature of the detection of alpha-triton pairs in coincidence is affected by the density of the material which is used to make the neutron converter layer. This is due to the loss of alpha particles inside the denser neutron converter material, which has a higher ability to stop them. This can be seen by comparing fig. 4.19 to fig. 4.20a, which present the coincidence detection capability of the detector using light material such as pure ^{6}Li (fig. 4.20a) instead of heavier one like ^{6}LiF (fig. 4.19). The coincidence detection characteristic of the detector is also affected by the thickness of the neutron converter layer, where the thicker the converter, the lower the performance of the detector is. This is clearly shown by comparing

fig. 4.20a and fig. 4.20b for the same neutron converter type (^{6}Li metal), but for different thicknesses. These figures show that the ^{6}Li foil (70 $\pm$ 10) μm thick has a great effect on the energy of the alpha-triton pairs, which are detected at the same time by both silicon sensors of the detector as coincidences. Consequently, the thinner the converter film thickness, the higher the energy deposited in both silicon sensors for a coincidence event, and hence the discrimination against the background radiation is better.

These results prove that using lithium-6 in its metallic form provides a better performance than the stable ^{6}LiF compound. This is due to the higher thermal neutron detection efficiency of the sandwich detector configuration, that can be achieved. In addition, the detector has a better resolution, where it is capable of discrimination between alpha and triton peaks. However, the main issue which will affect the performance of the sandwich detector configuration using a ^{6}Li foil, is the deterioration of the neutron count rate as shown in fig. 4.21 for both ^{6}Li foils of 40 and 70 μm thick. The neutron count rate decreases over time due to the corrosion effect on ^{6}Li foils, while it is constant over time in the case of using ^{6}LiF film as a neutron converter material in the sandwich detector configuration, as fig. 4.22 displays. Hence, using a ^{6}Li foil as a neutron sensitive material within the detector requires industrial manufacturing, where the ability exists to maintain the inert argon gas at a higher pressure than atmospheric pressure. Consequentially, the infusion of water vapour into the protective environment of the detector cannot happen and the ^{6}Li foil remains protected.

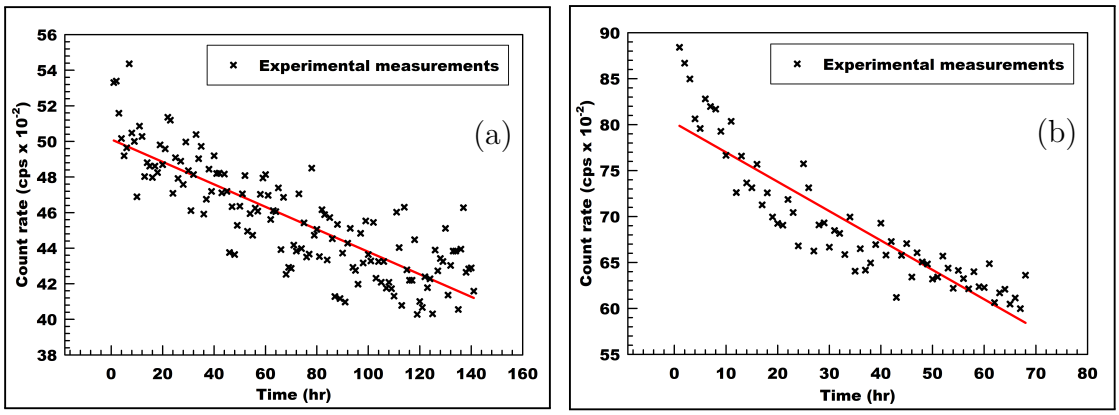

Figure 4.21: The observed neutron count rate of pure ^{6}Li foil:(a) (40 $\pm$ 10) μm thick, (b) (70 $\pm$ 10) μm thick. The lines drawn are a guide to the eye only.

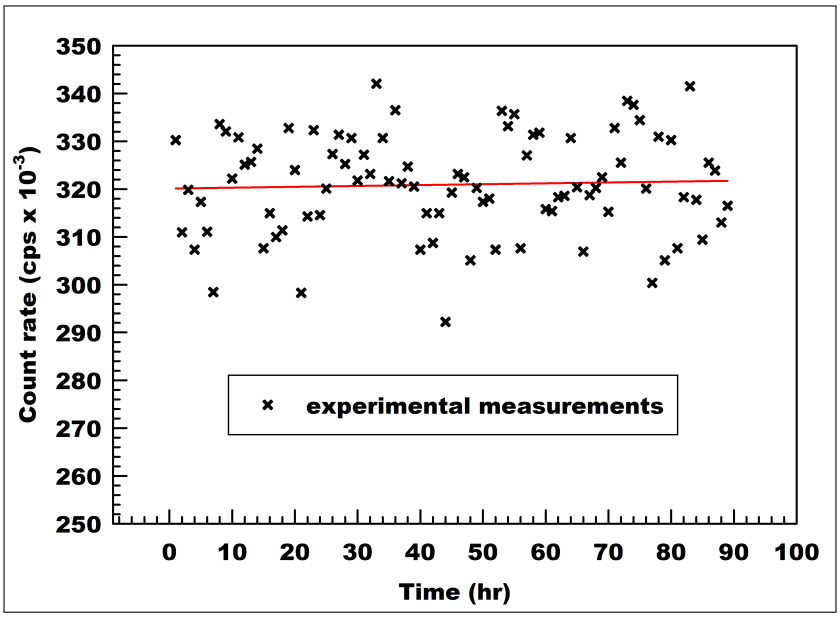

Figure 4.22: The observed neutron count rate of a ^{6}LiF film (1.5 $\pm$ 0.6) mg/cm^2 thick. The line drawn serves as a guide to the eye only.

4.4 Conclusion

The aim of the research presented in this chapter is to examine the use of enriched ^{6}Li as a neutron converter material with two silicon sensors with a 1×1 cm^2 active area in a sandwich detector configuration. Moreover, this Chapter set out to determine the optimal converter film/foil thickness, which can achieve the maximum detection efficiency of the single sandwich detector configuration. GEANT4 simulations have shown that the detector is capable of achieving the highest total detection efficiency of 7.5% by using a ^{6}LiF film of 35 μm thick. This efficiency can be enhanced up to 19% by using ^{6}Li foil of 120 μm thick instead of the ^{6}LiF film in the sandwich detector configuration. It has also been indicated that the highest coincidence detection efficiencies that can be achieved by the detector are 1.1% and 3.1% for ^{6}LiF film of 5 μm (1.2 mg/cm^2) thick and ^{6}Li foil of 20 μm thick respectively.

Tests have been done using ^{6}Li in a ^{6}LiF film and in its pure metallic form as a foil in order to validate the theoretical investigation, which has been performed via GEANT4 simulation. It has been shown that the experimental results are in good agreement with the predicted performance of the thermal neutron detector. Such detector in a sandwich design with ^{6}LiF film of (1.5 $\pm$ 0.6) mg/cm^2 thick is able to achieve a total (ε_{tn}) and coincidence (ε_{cn}) detection efficiency of (4.1 $\pm$ 0.5)% and (0.9 $\pm$ 0.3)% respectively. While, ^{6}Li foils of (40 $\pm$ 10) and (70 $\pm$ 10) μm thick are capable of attaining a total (ε_{tn}) detection efficiency of (9.2 $\pm$ 1.4)% and

(14.5 ± 2.2)% respectively, where the detection efficiency increased as a function of the converter foil thickness. However, the coincidence (ε_{cn}) detection efficiency decreased from (1.5 ± 0.9)% to (0.5 ± 0.3)% due to the increase in ^{6}Li foil thickness.

Finally, the developed neutron detection system was shown to function efficiently as a thermal neutron detector with its main feature of the differentiation between the neutron and the background gamma radiation. The detector can achieve a high gamma rejection factor up to 10^{8}, by using the coincidence methodology which has been discussed. This allows the detector to be used efficiently in a high gamma-ray environment, regardless of the energy of this radiation. In the next chapters, methods will be proposed to increase the thermal neutron detection efficiency of the detector and to enhance its performance to determine the direction of the thermal neutron flux.

Chapter 5

HDPE enhancement & directionality

5.1 Introduction

The performance of GAMBE has been investigated and discussed in chapter 4. This single sandwich detector configuration was combined with a ^{6}LiF film of thickness (1.5 ± 0.6) mg/cm^{2}, where a total (ε_{tn}) and a coincidence (ε_{cn}) detection efficiency of 4% and ∼1% was achieved respectively.

In this Chapter, the aim is to investigate a method to enhance the thermal neutron detection efficiency of this detector configuration. This method uses neutron moderators and reflectors such as HDPE sheets and lead blocks. The HDPE sheets are used to encase the detector to examine their effect on the thermal neutron flux through the neutron converter film. The increase in the flux will affect the detection efficiency of the single sandwich detector configuration. In addition, lead blocks have been used to create a window in the direction of the neutron flux for suppression of the background gamma radiation. MCNP-4C code has been used to perform an evaluation of the neutron flux distribution due to the effect of the HDPE sheets. These codes are described in the appendix D. These simulations have been verified experimentally by determining the enhancement of the total (ε_{tn}) and coincidence (ε_{cn}) detection efficiencies of the single sandwich detector.

This Chapter also presents a novel approach for finding the neutron flux direction. This approach is based on the combination of a solid-state neutron capture detector with the neutron moderators and reflectors, which have been used for the enhancement of the detection efficiency. The thermal neutron detection efficiency has been determined in different geometries where the whole system is rotated in

front of the ^{240}Am-^{9}Be neutron source. The variation of the thermal neutron detection rate due to the rotation provides a mean to determine the direction of the incoming neutron flux. Theoretical investigation using MCNP-4C code is used to verify the variation of the thermal neutron flux through the converter film based on the angle between the detector plane and neutron source.

5.2 Contribution of HDPE to detection efficiency

5.2.1 MCNP simulation of neutron flux

In order to determine the expected effect of the HDPE/lead confinement, Monte Carlo N-Particle transport code (MCNP) simulations were performed to determine the total ($\Phi_{t,sim}$) and the thermal ($\Phi_{th,sim}$) neutron fluxes (n/cm^2/s) through an area of 1×1 cm^2 of ^{6}LiF film. In these simulations, the geometry of two different experimental layouts are modeled, where an isotropic ^{241}Am-^{9}Be neutron source generating 1.5×10^9 particles with energies up to 12 MeV is assumed.

In the first simulation labeled as the "Basic" layout (see appendix D.1), the detector is in line with the neutron source, 75 cm away including 25 cm of water (see fig. 4.9 in section 4.3.1). In this layout there is no surrounding material, HDPE or lead around the detector. In the second simulation, "HDPE" layout (see appendix D.2), the detector is in the same position as the basic layout, but enclosed by 4 sheets of HDPE. Each sheet is 2 cm thick and has an area of 60 cm $\times$ 60 cm. The detector in the HDPE layout is also shielded by lead blocks of 5 cm thickness in the direction of the neutron flux as depicted in fig. 5.1.

The predicted value of the total ($\Phi_{t,sim}$) and thermal ($\Phi_{th,sim}$) neutron fluxes through the 1×1 cm^2 sensitive area of the detector (^{6}LiF film) according to different experimental setups are presented in table 5.1 and compared in fig. 5.2. Both the values of the total and thermal neutron fluxes are calculated and compared to the real ^{241}Am-^{9}Be neutron source, which emits 2.5×10^6 neutrons per second (n/s).

Table 5.1: Thermal ($\Phi_{th,sim}$) and total ($\Phi_{t,sim}$) neutron fluxes through the surface area of the ^{6}LiF film as a function of the different experimental layouts.

Layout (label)	$\Phi_{th,sim}$ (n/cm^2/s)	$\Phi_{t,sim}$ (n/cm^2/s)	% of $\Phi_{th,sim}$ (Normalised to $\Phi_{t,sim}$)
Basic	1.9 $\pm$ 0.1	8.03 $\pm$ 0.26	$\simeq$ 24%
HDPE	7.9 $\pm$ 0.2	13.1 $\pm$ 0.2	$\simeq$ 60%

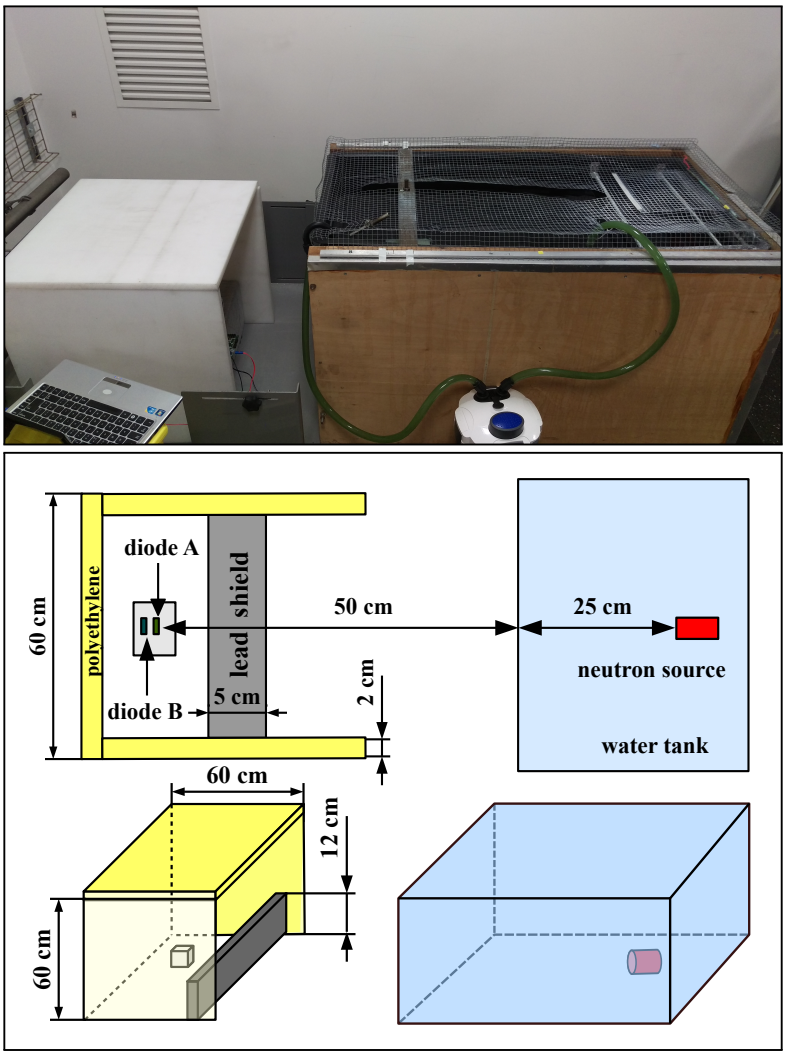

Figure 5.1: The "HDPE" experimental setup and its schematic layout.

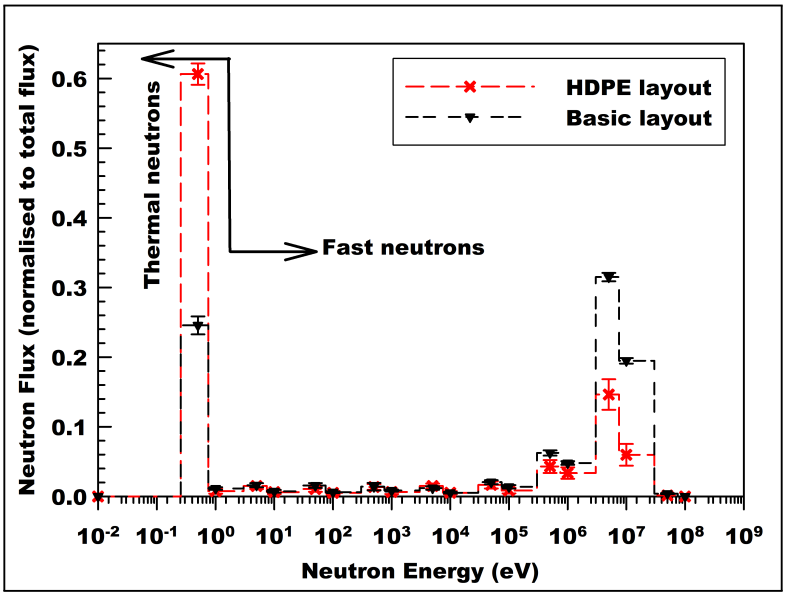

Figure 5.2: Variation of the neutron flux through an area of 1 cm^2 of ^{6}LiF film as a function of the neutron energy corresponding to the "Basic and HDPE" experimental layouts.

It is apparent from table 5.1 and fig. 5.2 that, the thermal neutron flux in the "Basic" layout is approximately 24% of the total neutron flux passing through the converter film. However, the "HDPE" layout experiment results in a higher proportion of thermal neutrons, which is up to 60% of the total neutron flux through the same converter layer. This is caused by the HDPE sheets facilitating fast neutron thermalisation via elastic collisions between neutrons and the hydrogen atoms in the sheets. The thermalisation process continues until the fast neutrons are in thermal equilibrium with the surrounding medium, a state where the neutrons cannot lose more energy and they have become thermal neutrons. Furthermore, the HDPE sheets scatter the thermalised neutrons back to the detector, and thus the field around the detector is enriched with thermal neutrons and the flux through the converter increases. On the other hand, heavy materials like lead have a minimal effect on the neutron kinetic energy, therefore, they are ineffective in blocking the incoming neutrons from the source. However, lead blocks will reflect the thermal neutrons scattered back from the HDPE sheets. They are effective also in shielding the detector against gamma-rays. Hence, any special neutron materials like plutonium shielded by lead in order to be used in a nuclear threat can still be detected by their neutron emission.

The rate of thermal neutron interaction (dN/dt) with the neutron converter is proportional to the number of neutrons crossing the area (A) of the film of thickness (X).

$$\frac{dN}{dt} = \Phi_{th} \times (AX\Sigma_F), \tag{5.1}$$

where Σ_F is the film macroscopic thermal neutron absorption cross-section. As can be seen from the data in table 5.1, the thermal neutron flux through the converter in the "HDPE" layout simulation is approximately four times higher than the thermal flux in the "Basic" layout. As a result the rate of neutron interaction inside the ^{6}LiF film increases by factor 4.

$$\left(\frac{dN}{dt}\right)_{HDPE} = 4\left(\frac{dN}{dt}\right)_{Basic} \tag{5.2}$$

In this case the detection efficiency, which has been determined using GEANT4 simulations can be improved by modifying eq. (4.5) in section 4.2.3 as follows:

$$\varepsilon_n = \frac{n}{N} \times P(x) = \frac{n}{N} \times (1 - e^{-4x\Sigma_F}) \tag{5.3}$$

Consequently, the thermal neutron detection efficiency of one sandwich detector configuration is expected to be enhanced by using the HDPE experimental setup.

5.2.2 Experimental validation of HDPE layout

The sandwich detector configuration with ^{6}LiF film of (1.5 $\pm$ 0.6) mg/cm^2 thickness has been tested in both "Basic" and "HDPE" experimental layouts (see figs. 4.9 and 5.1). The measured energy spectra due to the neutron being captured within the neutron converter corresponding to these layouts are shown in fig. 5.3. As can be seen from this figure the "HDPE" experimental setup affects both the neutron and gamma-ray count rate, it enhances the neutron count rate due to the effect of HDPE sheets on the neutron flux via the converter. As a result, the total and coincidence count rate (cps) increases from ((298 $\pm$ 1) $\times 10^{-3}$) and ((75 $\pm$ 1) $\times 10^{-3}$) to ((642 $\pm$ 1) $\times$ 10^{-3}) and ((141 $\pm$ 1) $\times$ 10^{-3}) respectively going from "Basic" to "HDPE". Furthermore, the lead window reduces the total and the coincidence count rate (cps) of the background gamma radiation from ((51 $\pm$ 1) $\times$ 10^{-3}) and ((231 $\pm$ 3) $\times$ 10^{-4}) to ((197 $\pm$ 2) $\times$ 10^{-4}) and ((74 $\pm$ 2) $\times 10^{-4}$) respectively.

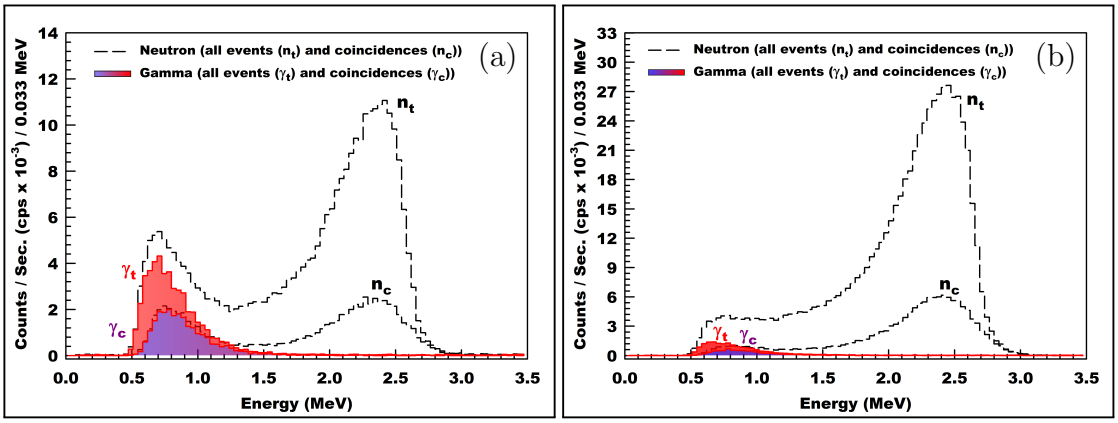

Figure 5.3: Spectra of energy deposited in both Si sensors of the detector corresponding to different experimental layouts: (a) "Basic" experimental layout, (b) "HDPE" experimental setup.

Consequently, the HDPE experimental configuration will not only result in an improvement of the thermal neutron detection efficiency, but it will also enhance the rejection ratio of the background gamma radiation. It has been found that the total (ε_{tn}) and coincidence (ε_{cn}) detection efficiencies of one sandwich sensor configuration increases up to (10.4 $\pm$ 1.3)% and (2.2 $\pm$ 0.8)% respectively. The experimentally determined detection efficiency is in a good agreement with the predicted values of ε_{tn} and ε_{cn} based on the MCNP and GEANT4 simulations, as shown in fig. 5.4.

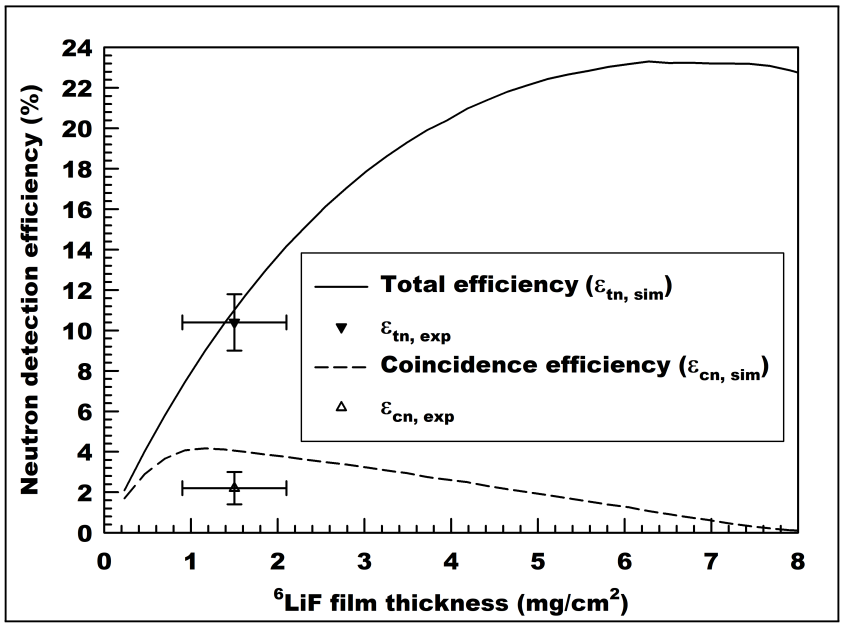

Figure 5.4: Simulated variation of the thermal neutron detection efficiency of a single sandwich detector as a function of ^{6}LiF film thickness corresponding to "HDPE" experimental layout. Also the experimentally determined thermal neutron detection efficiency is shown.

Five ^{6}LiF films with different thicknesses have been prepared and characterised using the same method, which was discussed before (see section 4.3.3.1). The thicknesses varied between (1.5 $\pm$ 0.6) and (2.9 $\pm$ 0.6) mg/cm^2. These sensors were tested individually in a single sandwich detector design with respect to the "HDPE" experimental layout (see fig. 5.1). The experimental results show that they were able to attain a higher total detection efficiency ($\varepsilon_{tn,exp}$) of (10.4 $\pm$ 1.3)%, (12.1 $\pm$ 1.6)%, (14.3 $\pm$ 1.9)%, (14.5 $\pm$ 1.9)% and (15.4 $\pm$ 1.7)% respectively. The detection efficiency of the detector increases by the growth of the converter thickness. This is due to the increment of the neutron capture probability, while the neutron reaction products are still capable of reaching and interacting with Si sensors, specifically the triton particles which have a higher range (L_t) through the ^{6}LiF film than that of the alpha-particles (L_α). These results are necessary in order to validate the predicted behaviour of the total thermal neutron detection efficiency ($\varepsilon_{tn,sim}$) based on MCNP and GEANT4 simulations as a function of the converter thickness, as displayed in fig. 5.5.

The simulations show that the coincidence detection efficiency ($\varepsilon_{cn,sim}$) decreases, as a result of increasing the converter thickness from (1.5 $\pm$ 0.6) to (2.9 $\pm$ 0.6) mg/cm^2 (see fig. 5.5). This is due to alpha particles are being stopped and lost inside the thicker film. Contrary to the expectation, the experimental results show that the coincidence detection efficiency ($\varepsilon_{cn,exp}$) changed randomly

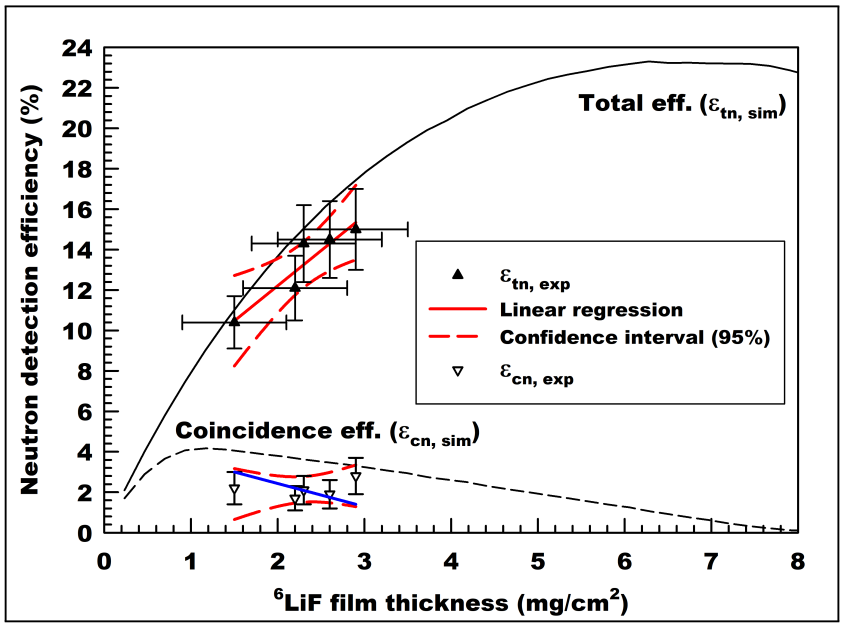

Figure 5.5: Variation of the thermal neutron detection efficiency of a single sandwich detector configuration as a function of ^{6}LiF film thickness in the "HDPE" experimental layout. This figure also shows the experimental thermal neutron detection efficiencies of five ^{6}LiF films.

with the variation of the film thickness in this particular range, as can be seen in fig. 5.5. A possible reason for this is that the capability of the detector to count a neutron based on the detection of a coincidence event is affected by the surface roughness of the film, which has been characterised by using AFM and KVDM (see section 4.3.3.1). Unfortunately, fig. 5.6 shows the non-uniform distribution of the films on the sensors surfaces, where the thickest areas of the films are identified by the red colour. Therefore, if a neutron is captured in these areas, there is a low possibility to be counted by the detection of alpha and triton particles as coincidences and this is the cause of the random behaviour of the coincidence detection efficiency. However, the diagonal (blue line in fig. 5.5) of the confidence interval for the experimental coincidence detection efficiency indicates that there might be an agreement between the experimental and the expected results.

In summary, the results in section 5.2 indicate the effect and the contribution of the HDPE sheets and the lead window on the thermal neutron detection efficiency of a single sandwich detector. It has been shown that, the detection efficiency of this single sandwich detector can be improved and the effect of the background gamma radiation on silicon sensor reduced to a lower limit by using this confinement.

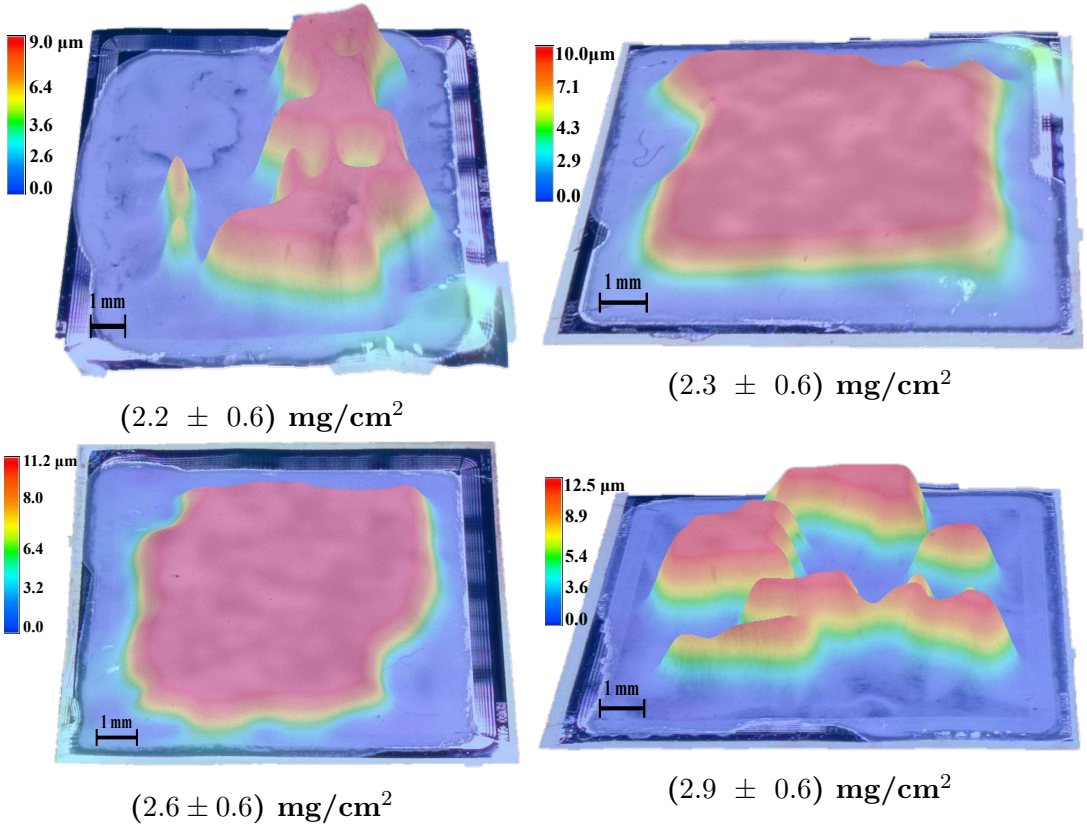

Figure 5.6: 3D images by KVDM, which show the distribution of the precipitated films of different thicknesses over the surface of the silicon sensor of an active area (1 × 1) cm^2, which will affect the behaviour of the detector regarding the coincidence detection efficiency (ε_{cn}).

5.3 Directionality and solid-angle

Determining the direction of the neutrons mainly depends on the interaction of fast neutrons. Fast neutron detection is based on the recoil protons from hydrogen-rich materials such as polyethylene through the (n,p) elastic scattering. This (n,p) reaction is not isotropic due to the direction of the recoil proton being a function of the direction of the incident neutron. Hence, the detection of this recoiled proton from a thin sheet of polyethylene can provide directional information about the incoming neutron [107]. There are several directional neutron detectors, which have been investigated such as ^{3}He detectors and plastic scintillating fibres [107–111].

Typical neutron detectors employed today are thermal neutron capture detectors because of their high intrinsic detection efficiency. In contrast to fast neutron detectors, thermal neutron capture detectors do not have the capability of inferring the direction of the incident neutron. Since, the incident thermal neutrons have low kinetic energy and, thus, they cannot affect the direction of the capture

reaction products, which are emitted in random directions. Consequently, the direction of the incoming thermal neutrons cannot be determined [112]. However, it has been shown that an array of large area silicon sensors used as a neutron captured detector has the capability of detecting thermal neutrons and determine the direction of the neutrons emitting source for the purpose of nuclear monitoring [113].

In the present work, the thermal neutron detector has been improved to provide information about the direction of the incoming neutron flux. The aim of this is to construct a portable neutron detection system which is based on both scattering and capture mechanism. In this construction, the detection efficiency will be affected by the direction of the neutron source with respect to the plane of the detector. Hence, the detector is able to determine the direction of neutron flux according to the variation of its detection efficiency at different angles in-front of this neutron source.

5.3.1 Solid angle effect on neutron flux

The hypothesis to be tested is based on the "HDPE" layout (see fig. 5.1) described in section 5.2.1. It is expected that this layout results in the total and thermal neutron flux of (13.0 $\pm$ 0.2) and (7.9 $\pm$ 0.2) n/cm^2/s respectively, through the converter. The thermal neutron flux is approximately increased up to 60% of the total due the effect of the HDPE sheets and lead blocks (see table 5.1). In order to achieve a directional detection, the whole setup, which includes the detector and HDPE box with a lead window was rotated corresponding to the original position in-front of an isotropic (^{241}Am-^{9}Be) neutron source as displayed in fig. 5.7.

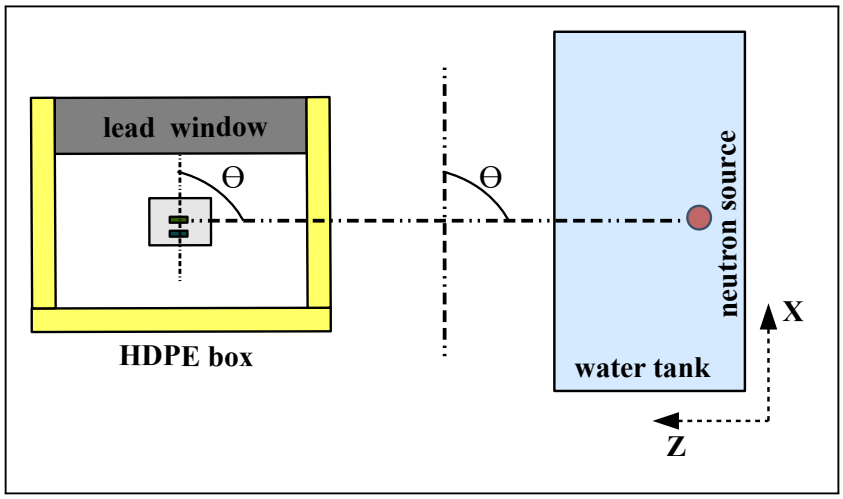

Figure 5.7: MCNP layout, which shows the rotational movement of the whole setup of "HDPE" experiment in front of the neutron source.

The original position is where the lead window faces the neutron source and the neutron flux is perpendicular to the surface area of the sandwich detector. The effect of the angular movement between the neutron source and the HDPE box on the neutron flux through the plane of the detector has been studied using MCNP simulations (see appendices D.3 to D.5). In addition, the detection efficiency of the detector corresponding to this angular movement will be examined in order to validate the simulations in achieving a directional information.

The simulated neutron flux through the sensitive part of the detector was affected by the angular between the flux direction and the plane of the detector. The predicted total and thermal neutron fluxes from this study are presented in fig. 5.8. Furthermore, fig. 5.9 illustrates the predicted energy spectrum of the neutron flux as a function of the angle (θ). It can be seen that the highest thermal neutron flux is achieved when the lead window faces the neutron source (i.e. $\theta = 0^{\circ}$). As discussed before in section 5.2, light material, like HDPE, will work as a neutron moderator, which will reduce the energy of fast neutrons and scatter them back towards the detector volume. Moreover, lead works to shield the detector against gamma-rays and reflects the thermal neutrons, which are scattered from the HDPE sheets, towards the detector.

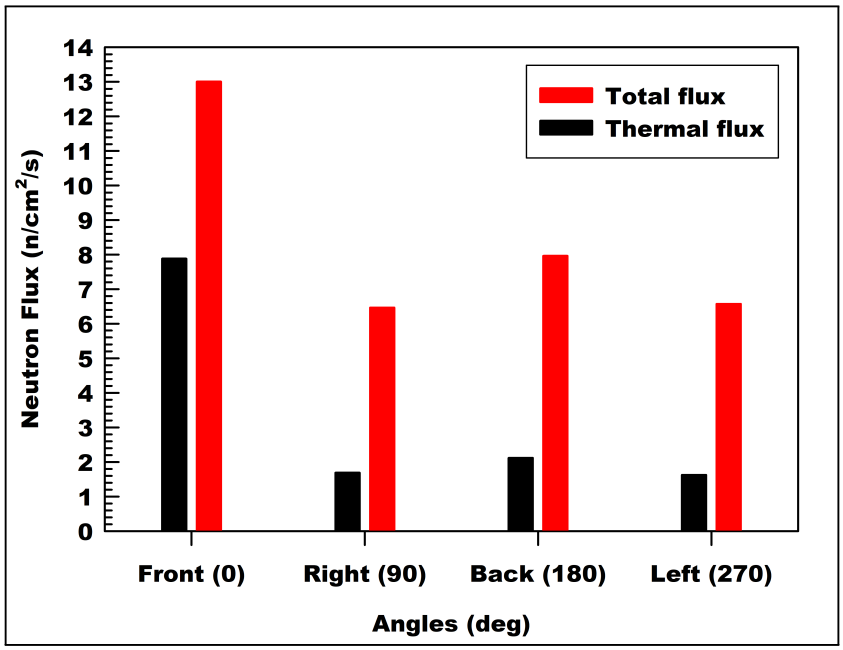

Figure 5.8: Simulated total and thermal neutron fluxes as a function of the angle between the detector and neutron source, which defines the direction of the flux through the detector.

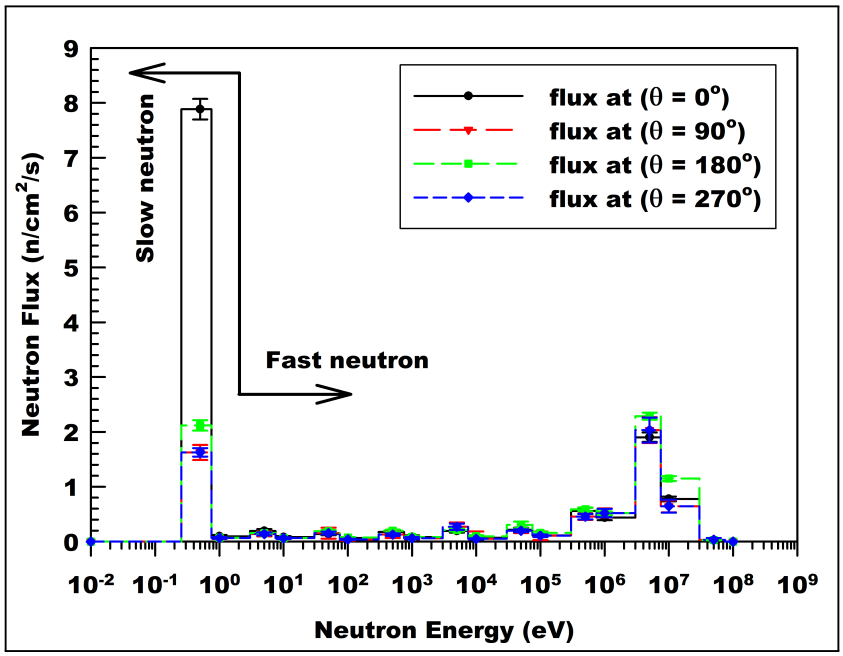

Figure 5.9: The simulated neutron flux as a function of the neutron energy and flux direction.

It is apparent from this theoretical investigation that it is possible to determine the direction of a neutron source based on the variation of the thermal neutron flux in specific directions. Therefore, it is expected that by using a neutron capture detector inside a HDPE box with a lead window, the direction of a neutron source can be determined.

5.3.2 Experimental behaviour of the detector

Experimental measurements have been carried out using a single sandwich detector with ^{6}LiF film (1.5 $\pm$ 0.6) mg/cm^2 thick as a neutron converter in combination with the "HDPE" experimental geometry (see fig. 5.1). The setup has been tested in front of the 1 Ci ^{241}Am-^{9}Be neutron source. It has been proved that the HDPE layout enhances the thermal neutron detection efficiency, which can be achieved by a single sandwich detector (see section 5.2.2).

The whole encapsulated detector setup is rotated in front of the neutron source, where the angle (θ) between the direction of neutron flux and the plane of the neutron converter is changed in steps of 90° (see fig. 5.7). The measured count rates of neutron and gamma-ray events for these configurations are presented in fig. 5.10. The highest neutron count rate is achieved when the lead window is facing the neutron source. On the other hand, the gamma-ray count rate is the lowest as a result of shielding using lead in the direction of neutron and gamma-ray fluxes as shown in fig. 5.10a. Hence, the lower gamma-ray count rate and the

highest thermal neutron count rate will result in the determination of the direction of the neutron flux.

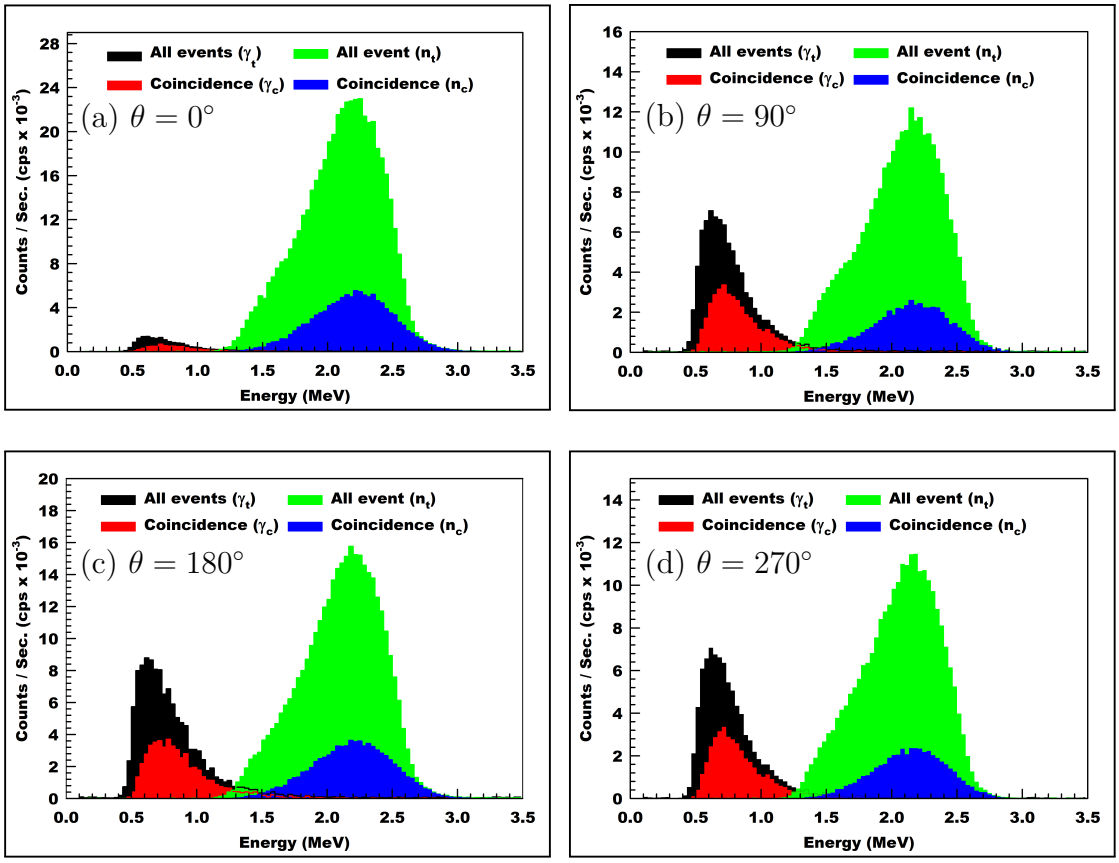

Figure 5.10: Measured neutron and gamma-ray energy spectrum as a function of the angle between the detector and neutron flux: (a) 0°, (b) 90°, (c) 180° and (d) 270°.

The total and coincidence detection efficiencies of the detector configuration for the different angles have also been determined, as shown in table 5.2 and fig. 5.11. These results show that the highest total and coincidence detection efficiencies are achieved when the lead window of the detector is perpendicular to the direction of the neutron flux and facing the neutron source. The detection efficiency varies with the rotation of the detector in front of neutron source with the lowest detection efficiency obtained when the lead window is parallel to the direction of neutron flux. In the case of back-flux, however, the neutron flux is perpendicular to the detector surface, the detector has a lower neutron detection efficiency than that in the case of front neutron flux. This is due to the HDPE sheet, which is facing the neutron flux, which causes thermal neutrons from the source to be reflected away from the detector.

Table 5.2: The experimental values of total and coincidence detection efficiency as a function of neutron flux direction.

Direction of flux (angle)	Total detection efficiency $\varepsilon_{tn,exp}$ (%)	Coincidence detection efficiency $\varepsilon_{cn,exp}$ (%)
Front (0°)	11.53 ± 0.04	2.54 ± 0.02
Right (90°)	5.96 ± 0.03	1.17 ± 0.01
Back (180°)	7.63 ± 0.03	1.65 ± 0.01
Left (270°)	5.71 ± 0.02	1.15 ± 0.01

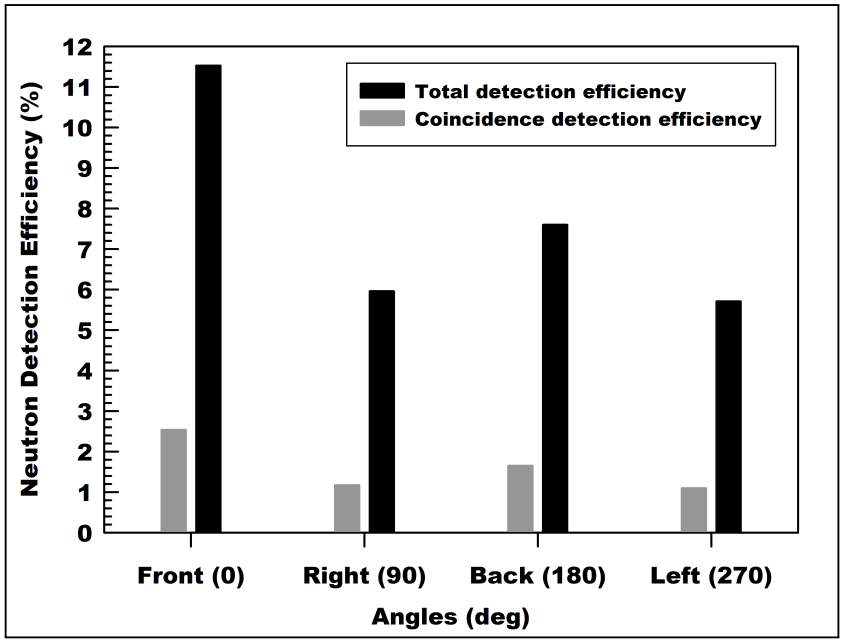

Figure 5.11: Total and coincidence detection efficiencies as a function of the angle between the detector and neutron source, which define the direction of the flux through the detector.

These experimental results are in agreement with the theoretical investigation using MCNP-4C simulations as can be seen in fig. 5.12. This figure shows the variation of normalised values of the simulated thermal neutron flux and detection efficiency with respect to the front configuration. This variation suggests that the combination of a thermal neutron detector and neutron moderators and reflectors can be used to find the direction of a neutron source.

In conclusion, a method was developed to increase the detection efficiency by using neutron moderators and reflectors, such as HDPE and lead, around the detector to increase the thermal neutron flux through the area of the neutron converter. As a result, the total and the coincidence detection efficiencies of a single sandwich detector with ^{6}LiF film of (1.5 ± 0.6) mg/cm^2 thick is enhanced from (4.1 ± 0.5)% and (0.9 ± 0.3)% to (10.4 ± 1.3)% and (2.2 ± 0.8)%

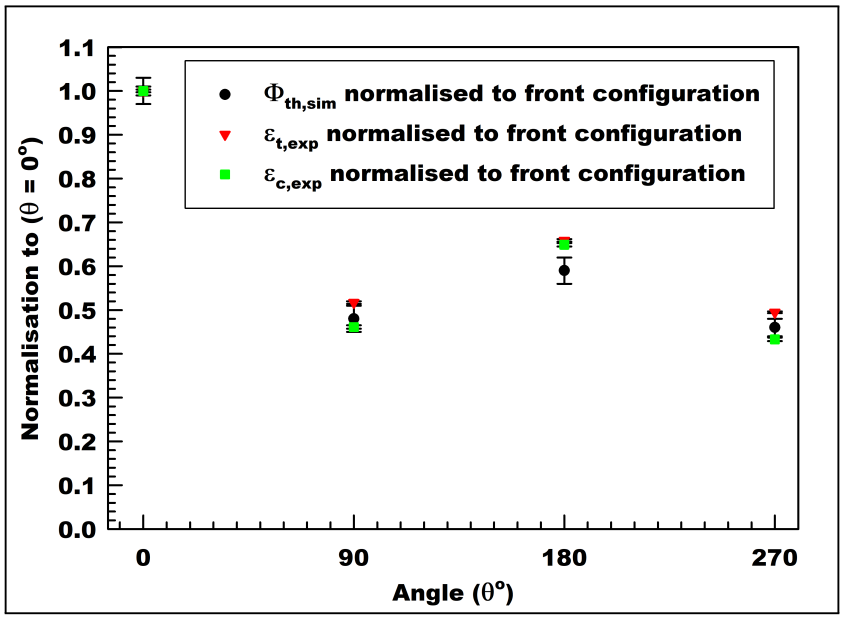

Figure 5.12: Variation of simulated thermal neutron flux, total and coincidence detection efficiency as a function of neutron flux direction with respect to the surface area of sensitive ^{6}LiF film.

respectively. It has also been found that the thermal neutron detection efficiency and the measured neutron and gamma-ray count rates of the detector, surrounded by scattering material, rotated with respect to the direction of the neutron flux change depending on the angle between the detector and neutron source. Therefore, the neutron detection system based on a thermal neutron capture detector in a sandwich configuration, which is combined with an enclosure of neutron moderators and reflectors can be used as a directional detector. The next Chapter moves on to discuss the effect of stacking detector configuration combined with the HDPE layout on the detection efficiency of the GAMBE system.

Chapter 6

Advanced stacked detector

6.1 Introduction

The purpose of the stacking approach is to increase the active volume where the neutron can be captured, while the charged particle reaction products are still capable of generating electronic signals in the silicon sensor [64, 76, 95]. Therefore, stacking individual sandwich detectors (Si-converter-Si) can increase the overall system neutron detection efficiency.

In this Chapter, the effect of stacking on the performance of GAMBE will be discussed. The study will take into consideration both neutron converter materials, which are ^{6}LiF and pure ^{6}Li. The optimum thickness of these converter materials will vary as a function of the number of the detectors in the stack. It also depends on the type of thermal neutron detection efficiency (total or coincidence), which is required to be achieved by the detector. This is due to the fact that the optimum thickness to attain the highest total detection efficiency for a certain number of stacked detectors will not be the same if the maximum coincidence detection efficiency is demanded for the same stacked detector. However, even though the coincidence method reduces the efficiency of the detector, it greatly improves the rejection of the background gamma radiation as has been discussed in chapter 4.

A stack of two sandwich detectors with ^{6}LiF films has been examined experimentally using the "HDPE" setup in order to validate results from simulations. The "HDPE" experimental geometry has been chosen due to its positive effect on the performance of a single sandwich detector. The combination between multilayer configuration and HDPE sheets in the design of the detector improves the thermal neutron detection efficiency as shown later in this Chapter.

6.2 Neutron detection efficiency enhancement

The concept of the proposed method is to enhance the detection efficiency of the GAMBE system by using multiple layers of sandwich detector (Si-converter-Si) as shown in fig. 6.1. This method is based on introducing a new factor, m, in eq. (4.5), which was discussed in section 4.2.3, where m is the number of the detectors in the stack. For the case in which the neutron converter layer is of the same thickness for all sandwich detectors in the stack, the fraction of the captured neutrons $P(x)$ is determined as follows.

$$P(x) = 1 - \frac{I_x}{I_\circ} = 1 - exp(-m \times \frac{N_A}{w_A} \times \rho \times \sigma \times x) \tag{6.1}$$

Hence, the thermal neutron detection efficiency, ε_n, of the stacked detector can be expressed by eq. (6.2).

$$\varepsilon_n = \frac{n}{N} \times P(x) = \frac{n}{N} \times \{1 - exp(-\frac{N_A}{w_A} \times \rho \times \sigma \times x \times m)\} \tag{6.2}$$

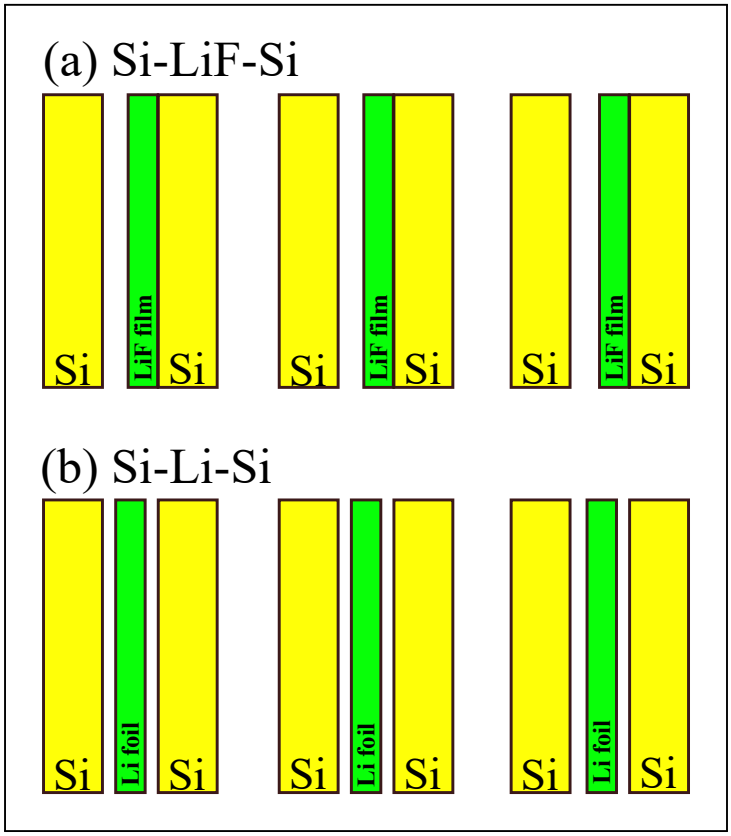

Figure 6.1: Schematic of a stacked detector with different converter materials. For instance three sandwich detectors in the stack with (a) ^{6}LiF film, (b) ^{6}Li foil.

Figure 6.2 shows the detection efficiency for multiple sensors in series. It can clearly be seen that the detection efficiency is not scaling linearly with the increasing number of stacked detectors. The initial neutron flux ($I_\circ$) will be attenuated by each of the neutron converters. As a result, the neutron flux (I_x) decreases for each subsequent detector. Moreover, in each reactive layer a proportion of incident neutrons are captured and not all result in a detection event.

Theoretically, if m in eq. (6.2) tends to infinity ($m \to \infty$), this means the exponential part of this equation will tend to zero ($e^{-\infty} \to 0$). Hence, the neutron capture efficiency is up to 100%, where all the incident neutrons on the stacked detector will be captured. However, the capture reaction products detection efficiency ($\frac{n}{N}$) of 100% cannot be achieved, due to the losses of the capture reaction products (n) in the converter itself. As a result, a stack with an infinite number of sandwich detectors cannot achieve 100% thermal neutron detection efficiency. For instance, it is anticipated, a multiple-layer proposal of one hundred and fifty sandwich detectors with converters of 4 μm or 2 μm thick (Si-^{6}LiF-Si) can achieve a total (ε_{tn}) and a coincidence (ε_{cn}) detection efficiency up to 82.5% and 53.8% respectively (see fig. 6.2a). In the case of using ^{6}Li foil, a lower number of stacked detectors is required to achieve $\varepsilon_{tn} > 80\%$ and $\varepsilon_{cn} > 50\%$. For example, a 70 sandwich detectors in a stack can attain a total (ε_{tn}) and a coincidence (ε_{cn}) detection efficiency up to 82% and 55% using foils of 12 and 7 μm thick respectively (see fig. 6.2b).

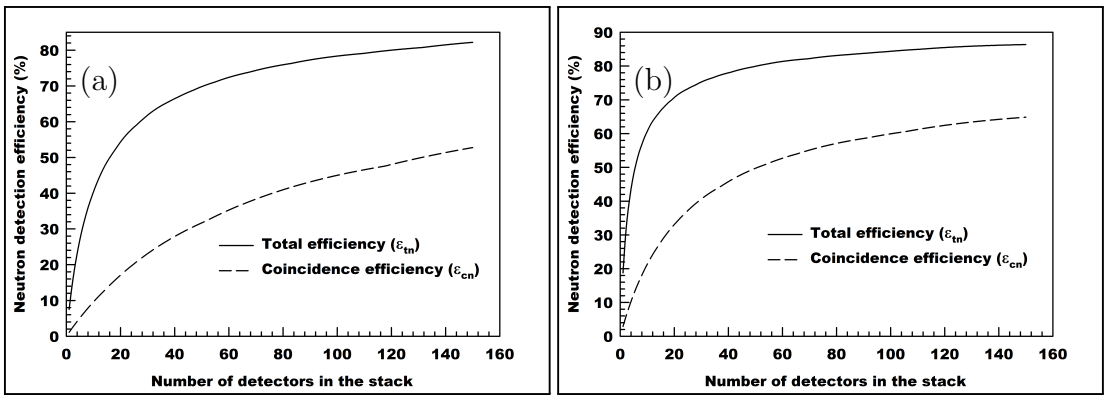

Figure 6.2: Variation of the thermal neutron detection efficiency as a function of the number of the sandwich detector in the stack corresponding to different neutron converter material: (a) ^{6}LiF, (b) ^{6}Li.

In addition, it is unlikely that the optimum thickness of either ^{6}LiF films or ^{6}Li foils remains constant. As can be seen in figs. 6.3 to 6.6 the optimum thickness of the individual neutron reactive layers decreases as the number of the detectors in the stack increases. These figures also show the calculated total or

coincidence detection efficiency for ^{6}LiF and ^{6}Li as a function of neutron converter layer thickness and the number of the detectors in the stack. The results of this study indicate that for a particular number of layers there is an ideal thickness that maximises the total and the coincidence detection efficiency of a stacked detector.

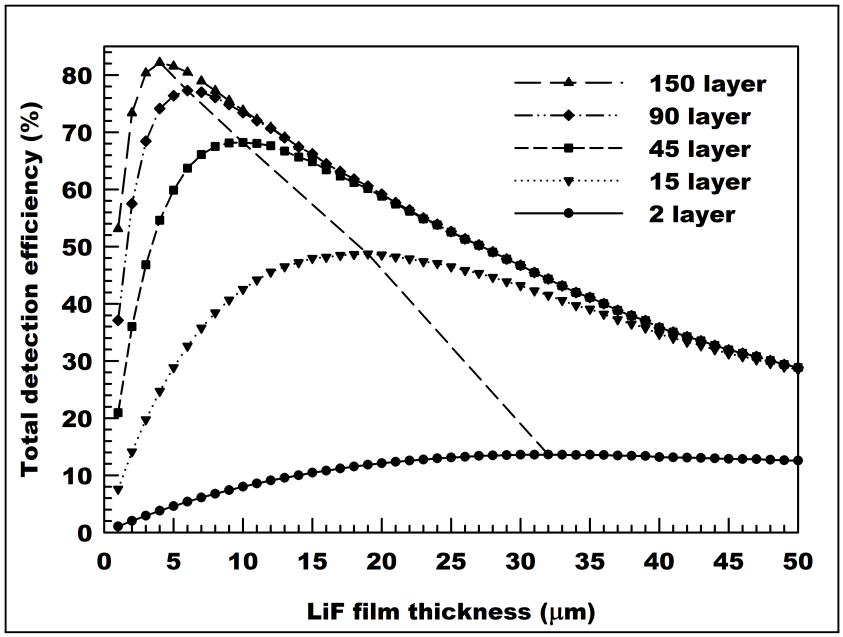

Figure 6.3: Variation of the total thermal neutron detection efficiency as a function of the number of sandwich detectors in the stack. The dashed line shows the change in the optimum ^{6}LiF film thickness corresponding to the number of layers.

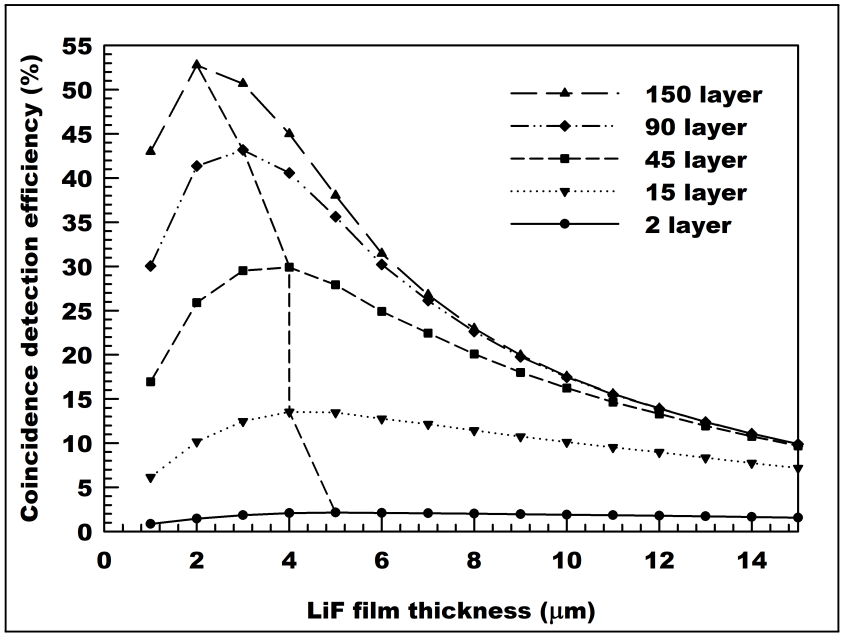

Figure 6.4: Variation of the coincidence thermal neutron detection efficiency corresponding to the number of sandwich detectors in the stack. The dashed line represents the the optimum ^{6}LiF film thickness as a function of the layer number.

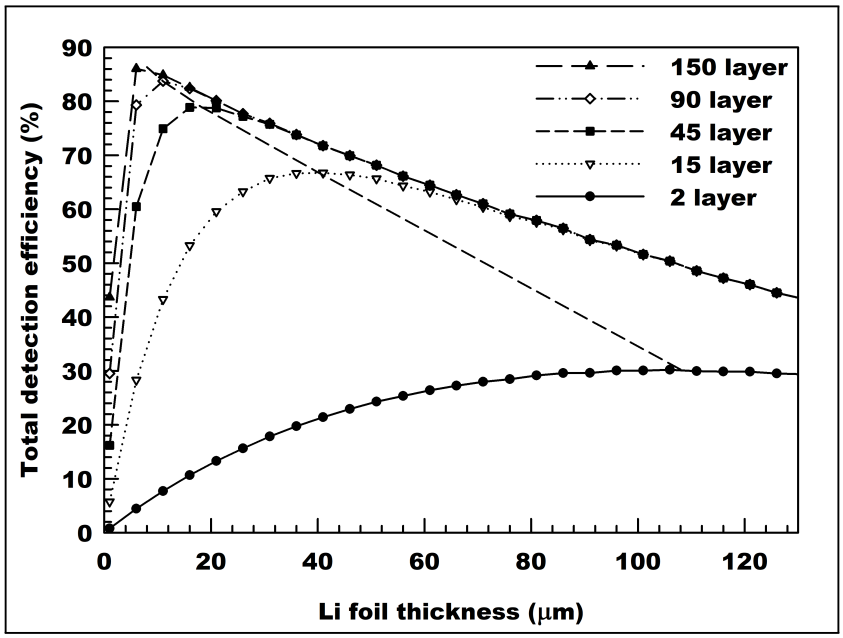

Figure 6.5: Variation of the total thermal neutron detection efficiency due to the number of sandwich detectors in the stack. The dashed line shows the optimum ^{6}Li foil thickness as a function of the layer number.

Some of the obtained results corresponding to the total and the coincidence detection efficiency of a stack with different number of detectors are summarised in table 6.1. The simulations indicate that a stack of ^{6}Li coated devices can achieve a much higher detection efficiency than a stack of ^{6}LiF coated sensors. However, the hygroscopic and reactive nature of pure ^{6}Li requires special handling and processing techniques in order to protect the foil thickness as discussed before in section 4.3.3.2.

Table 6.1: The variation of the neutron detection efficiency as a function of converter film/foil thickness and number of detectors.

^{6}LiF film				
Number of detectors	Optimum thickness (μm)	total detection efficiency ε_{tn} (%)	Optimum thickness (μm)	Coincidence detection efficiency ε_{cn} (%)
2	32	13.6	5	2.0
15	19	48.7	4	13.5
45	10	68.2	4	29.9
90	6	77.3	3	43.2
150	4	82.2	2	52.8

^{6}Li foil				
Number of detectors	Optimum thickness (μm)	Total detection efficiency ε_{tn} (%)	Optimum thickness (μm)	Coincidence detection efficiency ε_{cn} (%)
2	108	30.2	17	5.6
15	40	66.9	13	27.9
45	18	79.0	9	48.0
90	11	83.8	7	58.6
150	8	86.4	5	64.9

In all cases in figs. 6.3 to 6.6, it is shown that the number of detectors in the stack affects both the optimum neutron converter layer thickness and the detection efficiency of the stack. The optimum thickness decreases, while the detection efficiency increases due to the increment in the sandwich detectors numbers in the stack. However, it should be pointed out that the increase in the detection efficiency per added detector in the stack reduces as the number of detectors in the stack increases. This is due to the incident neutron flux on each sandwich detector in the stack not being the same. One thing to note is that more detectors in the stack increase the electronic noise in the system, which will affect the measurements especially in the lower energy range [77]. This is an issue that needs to be taken into account when designing the overall device.

6.3 Stack of two sandwich detectors with HDPE

It is apparent from the results, which have been discussed in sections 5.2 and 6.2 that both the use of HDPE sheets and of stacked detectors have a positive effect on the performance of the GAMBE system. Each of them enhances the thermal neutron detection efficiency of the detector. Therefore, the original design of the thermal neutron detector in a single sandwich configuration can be enhanced into a new design. In this design, two coated Si sensors with ^{6}LiF films of thicknesses (2.6 ± 0.6) and (2.9 ± 0.6) mg/cm^2 have been used in combination with two bare silicon sensors as a stack of two sandwich detectors. The coated and bare silicon sensors are connected to the available readout electronics (see figs. A.4 and A.5 in appendix A.3) as is shown schematically in fig. 6.7.

This stack has been mounted in the same aluminium box, which has been used in the previous experiments. The measurements have been carried out using the "HDPE" layout geometry (see fig. 5.1 in section 5.2.1) to examine the thermal neutron detection efficiency of the detector, as a result of the effect of both HDPE

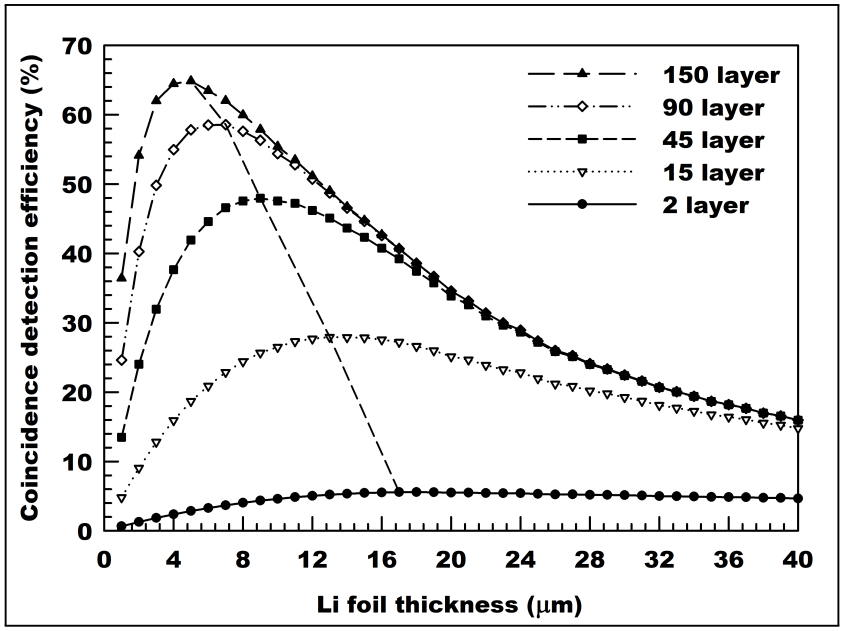

Figure 6.6: Variation of the coincidence thermal neutron detection efficiency as a result of the number of the sandwich detectors in the stack. The Dashed line represents the optimum ^{6}Li foil thickness as a function of the layer number.

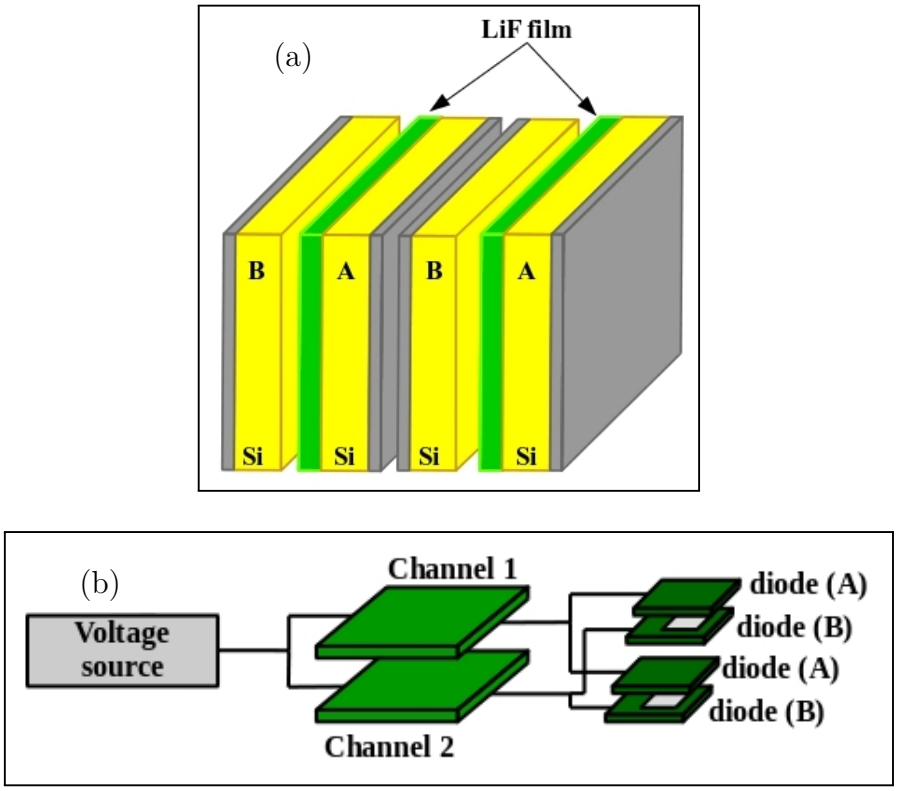

Figure 6.7: Configuration of the detector: (a) two sandwich detectors in combination with 2 ^{6}LiF films in a stack and (b) the connection of Si sensors to the reading out channels.

sheets and multilayer configuration. Figure 6.8 shows the neutron count rate of a single sandwich detector and a stacked detector. It can be seen that the stacked detector led to an increase of the total and coincidence count rates.

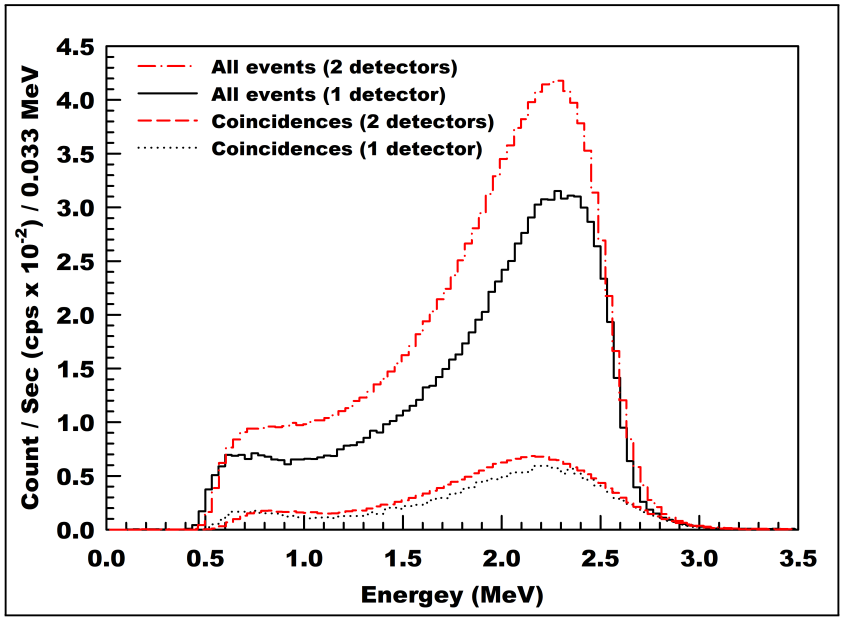

Figure 6.8: Measured spectra of the deposited energy in silicon sensors of the detector corresponding to the number of sandwich detectors in the stack, which have been tested by using "HDPE" experimental layout.

The total and the coincidence detection efficiencies were enhanced by about 72% and 47% respectively, compared to the total and coincidence detection efficiencies of a single (2.9±0.6) mg/cm^2 thick ^{6}LiF film. The stack can achieve a total and a coincidence detection efficiency of (27 ± 3)% and (4 ± 1)% respectively, as shown and compared to the results from the simulation in fig. 6.9. In this figure, the thickness of both ^{6}LiF films is considered to be (2.8 ± 0.6) mg/cm^2 based on the average thickness of the layers used. The detection efficiency of this stack was not expected to be doubled as a result of neutron attenuation by each ^{6}LiF layer, where the neutron flux decreases for each subsequent detector. Moreover, in each reactive layer a fraction of incident neutrons is captured and not all result in a detected event.

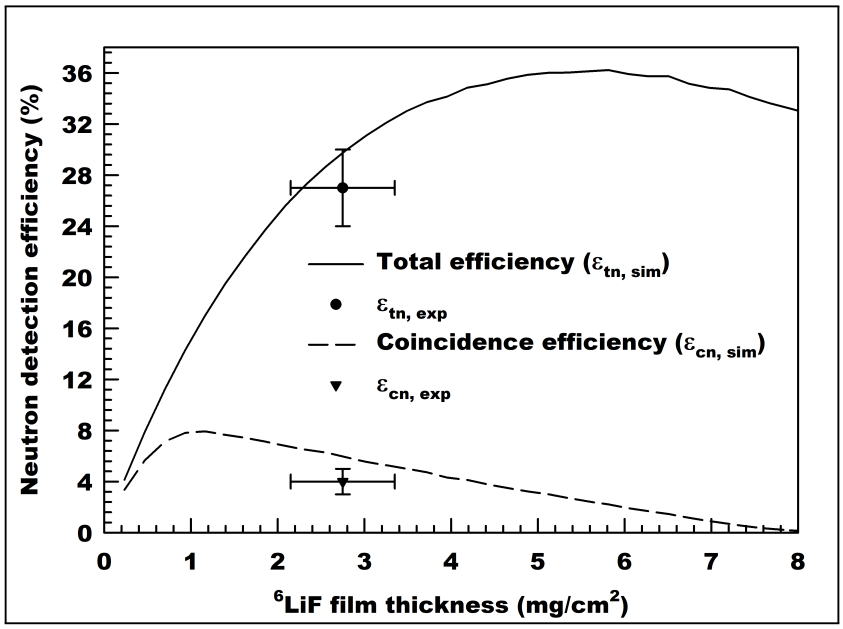

Figure 6.9: Variation of the thermal neutron detection efficiency of a stack of two sandwich detectors as a function of ^{6}LiF film thickness by using the "HDPE" experimental layout, showing the experimental detection efficiency of ^{6}LiF film of an average thickness of (2.8 $\pm$ 0.6) mg/cm^2.

6.4 Reducing the size of HDPE

For the purpose of constructing a handheld thermal neutron detector with high thermal neutron detection efficiency, the HDPE experimental layout has been redesigned with different dimensions. The lead window (see fig. 5.1) has been replaced by a lead window of 2.5 mm thick and an area of 8 cm $\times$ 8 cm. In addition, the HDPE sheets were replaced by ones with smaller dimensions, which have the same thickness but a different area of 10 cm $\times$ 10 cm. Figure 6.10 presents the modified construction of the handheld thermal neutron detector.

MCNP simulations (see appendix D "MCNP code") were performed to determine the total ($\Phi_{t,sim}$) and the thermal ($\Phi_{th,sim}$) neutron flux (n/cm^2/s) through the converters (2 ^{6}LiF films) of the stacked detector. In this simulation, the geometry of the "HDPE" experimental layout is altered into the new configuration with smaller dimensions, which will facilitate the design of a portable detection system. This new construction is placed at the standard detector position, where the system is in line with the neutron source, 75 cm away including 25 cm in water. The neutron source is an isotropic source, which generates 1.5×10^9 particles with energies up to 12 MeV (see section 5.2.1). In addition, the detector is enclosed by five small sheets of HDPE. Each sheet is 2 cm thick and has an area of 10×10 cm^2. The detector is also shielded by a lead sheet of 2.5 mm thick and

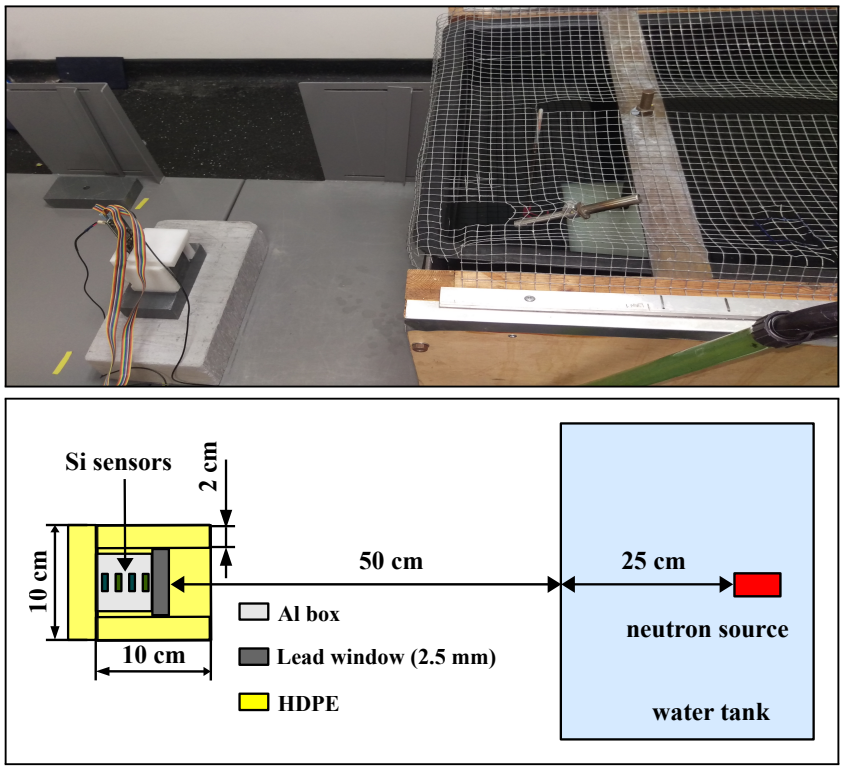

Figure 6.10: Layout of the encapsulated thermal neutron detector by 2 cm thick HDPE sheets, which have an area of 10 cm × 10 cm.

area of 8 × 8 cm^2, which is placed in the direction of the incoming neutron flux form the source. Figure 6.11 shows the predicted values of the neutron flux as a function of neutron energy, which have been normalised to the total flux ($\Phi_{t,sim}$) through the converter films according to the "HDPE" layout (see fig. 5.1) and the small HDPE detector design (see fig. 6.10).

These values are calculated and compared to the real ^{241}Am-^{9}Be neutron source, which emits 2.5 × 10^6 neutron per second (n/s). It is found that the thermal neutron flux via the neutron sensitive films in the small setup is reduced due to the reduction of the volume created by the HDPE sheets around the detector. In this case HDPE sheets work on shielding the detector and will reflect thermal neutrons away from the detector especially if the neutrons interact with the outer surface of the HDPE box. As a result, the total and coincidence detection efficiencies of the same stack of two sandwich detectors is reduced from (27 ± 3)% and (4 ± 1)% to (18 ± 2)% and (2.6 ± 0.9)% respectively. As can be seen in fig. 6.12, the results are compared to the predicted performance of the stack of two sandwich detectors corresponding to the small HDPE detector design and the "HDPE" experimental setup. This figure shows that the experimental results are in a good agreement with the simulation.

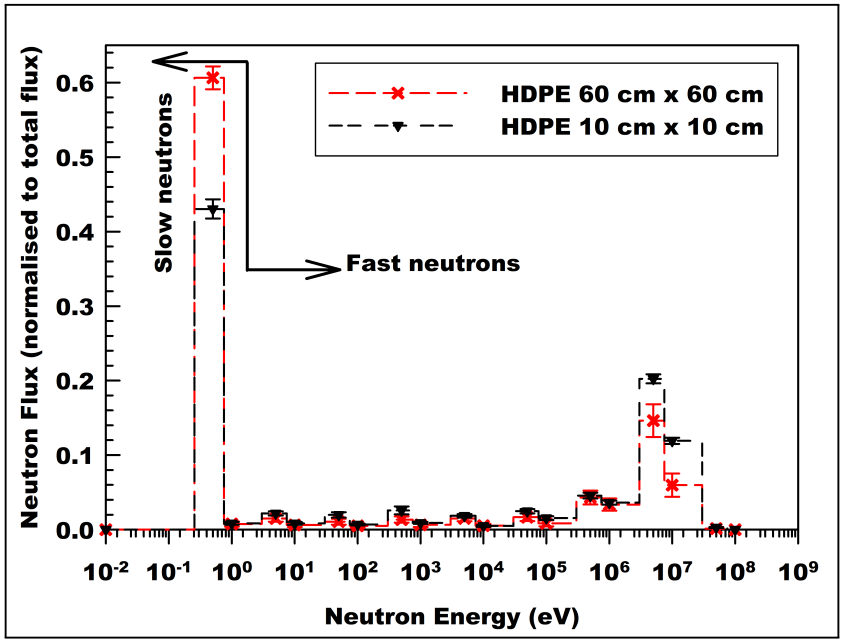

Figure 6.11: The normalised neutron flux to the total flux corresponding to "HDPE" experimental layout and the small HDPE detector configuration.

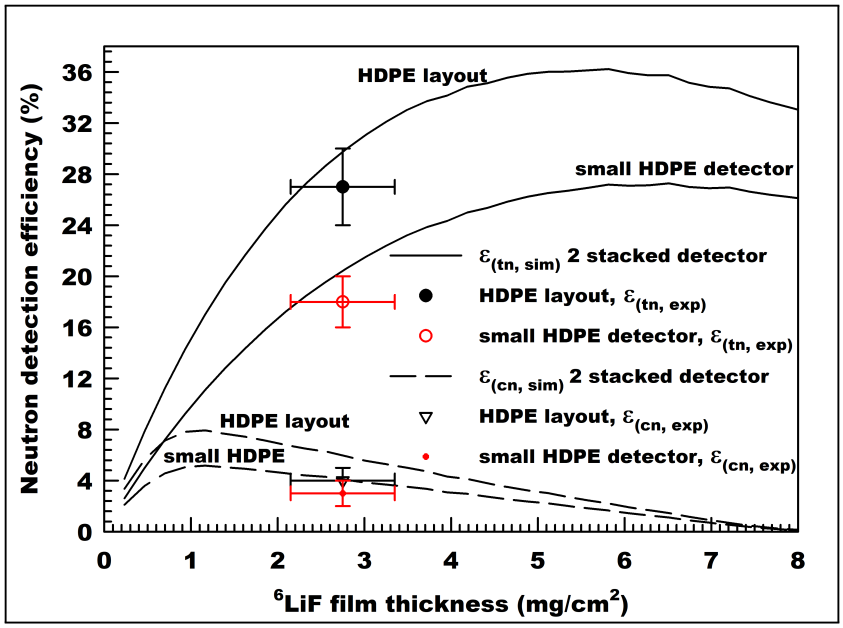

Figure 6.12: Variation of the thermal neutron detection efficiency of a stack of two sandwich detectors as a function of ^{6}LiF film thickness corresponding to the HDPE and small HDPE detector, showing the experimental detection efficiency of a ^{6}LiF film of an average thickness of (2.8 ± 0.6) mg/cm^2.

6.4.1 Small HDPE detector enhancement

It has been shown in the previous section that the purpose behind reducing the size of HDPE sheets is to construct a new design for a portable thermal neutron detector, which can achieve high detection efficiency relative to ^{3}He detector tubes. However, the size reduction process of the HDPE sheets has a negative side effect on the neutron detection efficiency of the detector. Therefore, four coated silicon sensors (see fig. 6.13) with ^{6}LiF films thicknesses of (2.2 $\pm$ 0.6), (2.3 $\pm$ 0.6), (2.6 $\pm$ 0.6) and (2.9 $\pm$ 0.6) mg/cm^2 have been used in the stack in order to diminish this negative effect on the detection efficiency. These four coated silicon sensors are connected to the electronic system as described previously in fig. 6.7b, where the bare silicon sensors are replaced by coated ones.

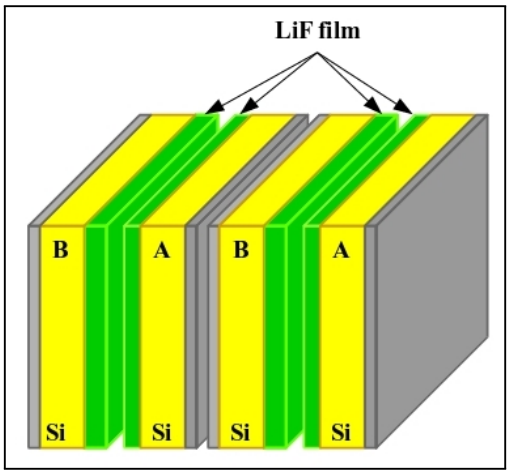

Figure 6.13: Schematic configuration of stacked four Si sensors, which have been coated with ^{6}LiF.

This configuration severely affects the coincidence detection capability of the small HDPE detector, where the coincidence detection efficiency is decreased to a lower level of (0.61 $\pm$ 0.02)% from (2.6 $\pm$ 0.9)%. This is due to losing alpha particles inside the ^{6}LiF films, which are on top of each silicon sensor. Figure 6.14 clarifies the effect of this stack of four coated silicon sensors on the energy of the charged particle reaction products. These reaction products have to move through the converter films to interact with the depleted region of silicon sensors in order to produce electronic signals. Hence, triton and alpha particles will lose a large amount of energy prior to them reaching the silicon sensors in the stack of four coated sensors.

In contrast, results show that the total detection efficiency of this small HDPE detector raised from (18 $\pm$ 2)% to (22.8 $\pm$ 0.1)% by using these four coated silicon sensors in this stack of two sandwich detectors. However, this modified

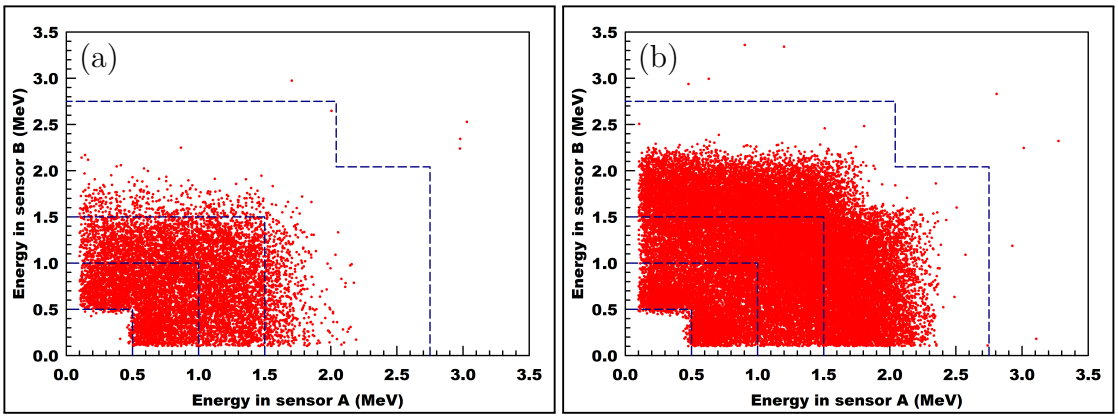

Figure 6.14: Detected events as coincidences in four silicon sensors of the small HDPE detector, which consists of two sandwich detectors in a stack: (a) Each Si sensor is coated (see fig. 6.13), (b) two silicon sensors are coated (see fig. 6.7a).

detector show a worse resolution as seen in fig. 6.15, which will affect the γ/n rejection factor. This is caused by the alpha and triton particles, which will lose their energy inside each film before interacting with the sensitive region of the detector. Therefore, it is suggested that this device can work as a neutron counter to detect the presence of neutrons in the field or for dosimetry purposes.

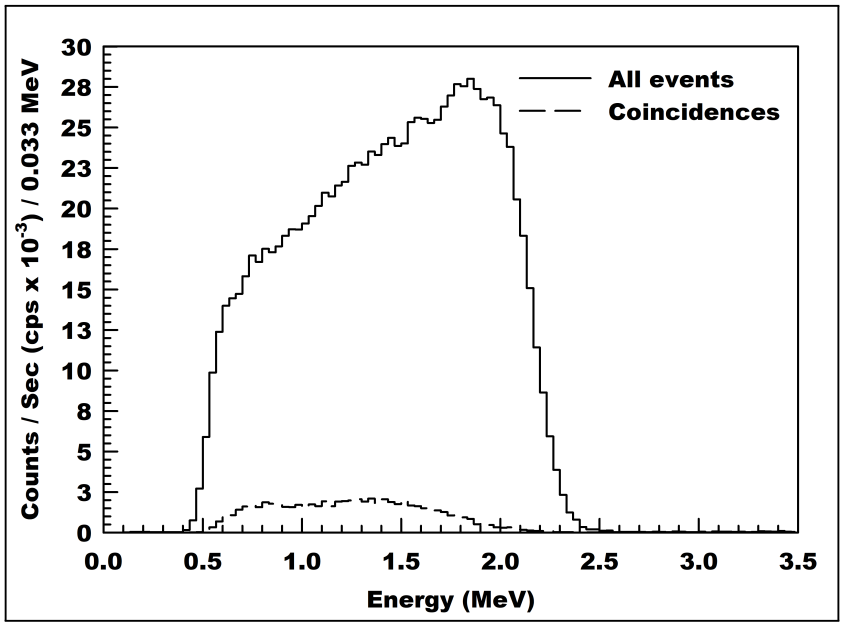

Figure 6.15: The deposited energy spectrum for ^{6}Li(n,α)^{3}H reaction products in the coated Si sensors of stacked detector.

In conclusion, the results in the previous Chapter (chapter 5) indicate that the HDPE layout improved the total and the coincidence detection efficiency of a single sandwich detector up to (15 $\pm$ 2)% and (2.8 $\pm$ 0.9)% respectively. In this Chapter, it was found that the combination of a stacked detector design and

HDPE sheets increases the total and the coincidence detection efficiencies up to (27 ± 3)% and (4 ± 1)% respectively. In addition, the potential of a small HDPE detector with a 2.5 mm thick lead window has been studied by using four coated silicon sensors. These coated sensors have been mounted in stacked design of two sandwich detectors. This small HDPE detector can achieve a high total detection efficiency of (22.8 ± 0.1)% comparable to the detection efficiency of ^{3}He detector tubes of 1 m long.

Finally, the information gathered in this thesis has been combined to suggest an optimum configuration for a handheld thermal neutron detector, as will be discussed in the final Chapter. This handheld detector depends on semiconductor neutron capture detector and neutron moderators such as HDPE, where the GAMBE system can achieve the best performance and the highest detection efficiency. In addition, it will have the ability to determine the direction of a neutron source.

Chapter 7

Handheld neutron detector

7.1 Introduction

This project was undertaken to design a neutron detector, GAMBE, which can achieve a high neutron detection efficiency with a high gamma-ray rejection factor of 10^8. Moreover, making the detector able to determine the direction of neutron flux according to the variation of the detection efficiency at different angles in front of a neutron source. This Chapter will deliver the ultimate goal of this research, which is the design of a portable neutron detector. This portable detector is able to achieve a high thermal neutron detection efficiency. Hence, the handheld neutron detector can be used in homeland security, where it can help in identifying nuclear threats.

The design of the handheld detector is based on the simulation packages, which have been validated by the experimental results through demonstration of a good agreement with the predicted results during the various stages of this research. This Chapter starts with an overview of all results, which have been discussed. Then, the requirements to design a handheld neutron detector will be explained, and finally, the recommendation for future work are suggested.

7.2 Results overview

The research started with a series of GEANT4 simulations to predict the converter thickness corresponding to optimal total and coincidence detection efficiencies of a single sandwich detector with a 1 × 1 cm^2 active area. The results have shown that a single sandwich detector was able to achieve a highest total detection efficiency of 7.5% by using a 35 μm thick ^{6}LiF film. This efficiency was enhanced up to 19% by changing the converter to 120 μm ^{6}Li foil. It has also been found that the highest coincidence detection efficiencies that can be achieved by a single sandwich detector are 1.1% and 3.1% for a 5 μm (1.2 mg/cm^2) thick ^{6}LiF film and 20 μm thick ^{6}Li foil respectively. In order to validate the coincidence detection capability of the single sandwich design, the detector was tested experimentally in a particular position, in front of an isotropic ^{241}Am-^{9}Be neutron source. Such detector in a sandwich design with (1.5 ± 0.6) mg/cm^2 ^{6}LiF film was able to achieve a coincidence detection efficiency (ε_{cn}) of (0.9 ± 0.3)% and a total detection efficiency (ε_{tn}) of (4.1 ± 0.5)%. While, (40 ± 10) μm thick ^{6}Li foil was capable of attaining a higher total (ε_{tn}) and coincidence (ε_{cn}) detection efficiency of (9 ± 1)% and (1.5 ± 0.9)% respectively. The GAMBE detection system also has a high gamma rejection factor up to 10^8, due to the coincidence detection methodology and works efficiently as a thermal neutron detector.

A method was developed in order to enhance the detection efficiency of a single sandwich detector. This method employs neutron moderators and reflectors such as HDPE sheets and lead blocks, which were named the "HDPE" layout. The HDPE sheets were used to encase the detector to increase the neutron flux through the converter. While, the lead blocks were used to create a window for the suppression of the incident gamma rays on the detector. As a consequence of this, the total and coincidence detection efficiencies of a single sandwich detector with (1.5 ± 0.6) mg/cm^2 thick ^{6}LiF film is enhanced from (4.1 ± 0.5)% and (0.9 ± 0.3)% to (10 ± 1)% and (2.2 ± 0.8)% respectively. Furthermore, the total and the coincidence detection efficiency raised to (16 ± 2)% and (2.8 ± 0.9)% respectively due to the growth of this film thickness to (2.9 ± 0.6) mg/cm^2. The "HDPE" layout has another significant aspect, which is supplying the single sandwich detector with the ability to determine the direction of the neutron flux. This is due to the changes in the thermal neutron detection efficiency and the variation of the measured neutron and gamma-ray count rates, depending on the angle between the detector plane and the neutron source.

It has also been shown that stacking multiple layers of a sandwich detector, (Si-converter-Si), increased the detection efficiency of the GAMBE system. For

instance, it was predicted that a stack of one hundred and fifty sandwich detectors, (Si-^{6}LiF-Si), with converters of 4 μm or 2 μm thick raised the total (ε_{tn}) and coincidence (ε_{cn}) detection efficiencies up to 82.5% and 53.8% respectively. While, using ^{6}Li foil results in lowering the number of sandwich detectors in a stack in order to achieve $\varepsilon_{tn} > 80\%$ and $\varepsilon_{cn} > 50\%$. For example, stacking 70 sandwich detectors can attain a total (ε_{tn}) or a coincidence (ε_{cn}) detection efficiency up to 82% and 55% using foils of 12 μm and 7 μm thick respectively. Furthermore, it was experimentally confirmed that the combination of a stacked detector design and "HDPE" layout improved the total and the coincidence detection efficiency from (16 $\pm$ 2)% and (2.8 $\pm$ 0.9)% to (27 $\pm$ 3)% and (4 $\pm$ 1)% respectively. This combination led to studying the potential of a small HDPE detector with a 2.5 mm thick lead window as a handheld detector, which is consisted of four coated sensors in a stacked design of two sandwich detectors. Consequentially, the small HDPE detector is able to achieve a high total detection efficiency of (22.8 $\pm$ 0.1)%.

Finally, the results of this study are summarised in table 7.1. These results provide further support to design the handheld thermal neutron detector, which has a high neutron detection efficiency comparatively with the existing neutron detectors nowadays.

7.3 Handheld thermal neutron detector

Combining all results, which have been discussed in this research, the optimum configuration for a handheld thermal neutron detector can be designed based on GEANT4 simulations. The optimal thickness of the neutron converter relies on the demanded thermal neutron detection efficiency, the type of converter material (^{6}LiF or ^{6}Li) and the number of the sandwich detectors in the stack. In addition, the handheld detector design depends on the MCNP simulations to predict the thermal neutron flux through the converters, which was experimentally validated in section 6.4 for the small HDPE detector.

It can therefore be assumed that the portable neutron detector has the same design of the small HDPE box with a 2.5 mm thick lead window, which was explained in section 6.4. The thickness of each face of the HDPE box is 2 cm thick, where this box has an inner space of 8 cm height and base of 8 $\times$ 8 cm^2. Inside this space, an aluminium enclosure will be mounted, which can contain a number of sandwich detector up to seven in a stack. Each one of these sandwich detectors consists of 2 silicon sensors, where each sensor has a thickness of 300 μm and an active area of 1 $\times$ 1 cm^2. In addition, the designed aluminium box is used

Table 7.1: GAMBE detection efficiency according to different experimental setups and detector configurations.

Geometry	Material	Thickness		Simulation efficiency		Experimental efficiency	
		($\frac{mg}{cm^2}$)	(μm)	total (%)	coincidence (%)	total (%)	coincidence (%)
Basic	^{6}LiF	1.5 ± 0.6	∼ 7 ± 3	3.0	1.0	4 ± 1	0.9 ± 0.3
	^{6}Li	∼ 1.8 ± 0.5	40 ± 10	11.6	2.7	9 ± 1	1.5 ± 0.9
	^{6}Li	∼ 3.2 ± 0.5	70 ± 10	16.1	2.0	15 ± 2	0.5 ± 0.3
HDPE	^{6}LiF	1.5 ± 0.6	∼ 7 ± 3	11.0	3.9	10 ± 1	2.2 ± 0.8
		2.2 ± 0.6	∼ 9 ± 3	14.5	3.7	12 ± 2	1.7 ± 0.6
		2.3 ± 0.6	∼ 10 ± 3	15.0	3.6	14 ± 2	2.1 ± 0.7
		2.6 ± 0.6	∼ 11 ± 3	16.2	3.4	15 ± 2	1.9 ± 0.7
		2.9 ± 0.6	∼ 13 ± 3	17.3	3.2	16 ± 2	2.8 ± 0.9
HDPE 2 sandwiches	^{6}LiF	2.8 ± 0.6	∼ 12 ± 3	29.7	5.7	27 ± 3	4 ± 1
small HDPE 2 sandwiches	^{6}LiF	2.8 ± 0.6	∼ 12 ± 3	20.6	4.1	18 ± 2	2.6 ± 0.9
enhanced small HDPE 4 layers	^{6}LiF	2.2 ± 0.6	∼ 9 ± 3	N/A	N/A	22.8 ± 0.1	0.61 ± 0.02
		2.3 ± 0.6	∼ 10 ± 3				
		2.6 ± 0.6	∼ 11 ± 3				
		2.9 ± 0.6	∼ 13 ± 3				
Double-inward coated detector [77]	^{10}B	N/A	1.7	8.06	1.87 (at 0.5 μm)	N/A	N/A
	^{6}LiF	N/A	30	8.2	1.29 (at 2 μm)	8.95	avoided

to provide a protective environment for ^{6}Li foils against corrosion.

In the case of using ^{6}LiF coating as a thermal neutron sensitive material, one silicon sensor of each sandwich detector in the stack will be coated, with all coated sensors having the same ^{6}LiF film thickness. Figure 7.1 shows the determined total and coincidence detection efficiency of a portable GAMBE system, which consists of seven single sandwich detectors as a function of ^{6}LiF film thickness. The results indicate that the designed portable detector can achieve a total detection efficiency of 52%, where seven silicon sensors of the sandwich detectors are coated by ^{6}LiF of 17 μm thick. This thickness is able to attain a coincidence detection efficiency of 6.6%. On the other hand, a 4 μm thick ^{6}LiF film enhances the ability of the detector to detect more coincidence events, where the coincidence detection efficiency of the portable detector increases up to 15.4%. As a consequence, the total detection efficiency is reduced to 28.1%.

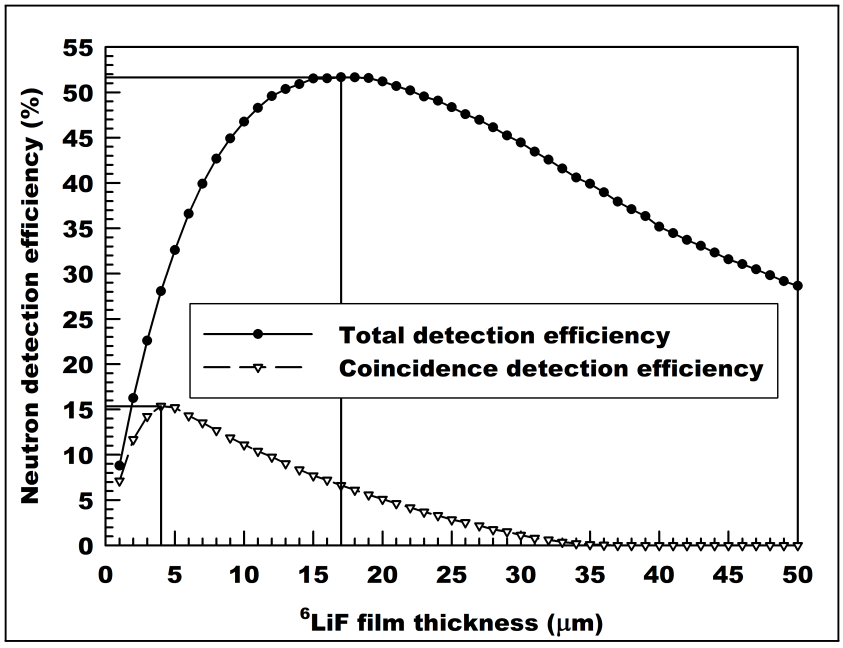

Figure 7.1: Variation of the total and coincidence detection efficiencies of the handheld detector of seven sandwich detectors in a stack as a function of the ^{6}LiF film thickness.

Regarding the ^{6}Li-coated devices, fig. 7.2 presents the calculated total and coincidence detection efficiencies of the handheld GAMBE system, which consists of seven single sandwich detectors as a function of ^{6}Li foil thickness. It becomes clear from figs. 7.1 and 7.2 that a stack of ^{6}Li-coated devices provides much higher neutron detection efficiencies than the portable detector of stacked ^{6}LiF-coated sensors. However, the hygroscopic and reactive nature of ^{6}Li requires special handling and processing techniques in order to achieve an accurate and optimized

foil thickness. Therefore, the detector configuration must be sealed inside the aluminium enclosure under high pressure of an inert gas such as argon to provide a protective environment for the sensitive ^{6}Li against corrosion. As can be seen from fig. 7.2, the stack of seven sandwich detectors has a highest total detection efficiency of 69% corresponding to 36 μm thick ^{6}Li foil, which is able to achieve a coincidence detection efficiency of 12.1%. This coincidence detection efficiency can be improved up to 16.4% by reducing the thickness of ^{6}Li foil to 16 μm. The total detection efficiency corresponding to this thickness of 16 μm decreases to 57.9% due the decrement of the converter thickness.

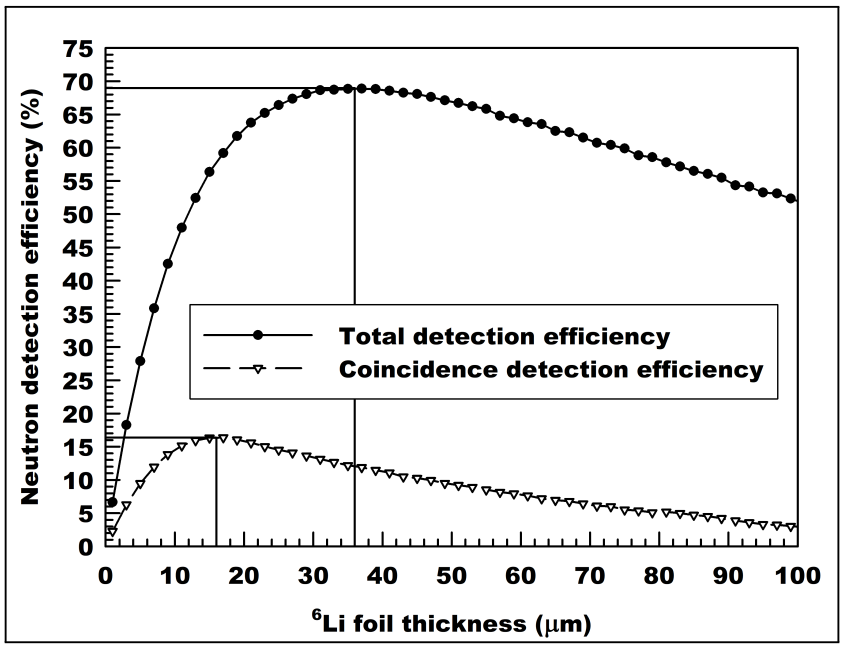

Figure 7.2: Variation of the total and coincidence detection efficiencies of the handheld detector of seven sandwich detectors in a stack as a function of the ^{6}Li foil thickness.

7.4 Conclusion

In conclusion, this thesis has described a developed directional neutron detector, which is based on the simplest planar design used to adapt semiconductor devices for the detection of thermal neutrons. This study covers the simulations, design, fabrication, characterisation and application of this neutron detector. The developed GAMBE detector is useful for mixed $\gamma-$n radiation environments, where current neutron detectors cannot be easily used. This is due to the high gamma-ray rejection factor of 10^{8}, which is achieved by using the detector new features, the detection of coincidence and the PHD method. Furthermore, this research

gives the opportunity to the users to choose among different designs of the detector, which can be used in different applications based on the required neutron detection efficiency. This detection efficiency varies according to the type of neutron converter materials (^{6}LiF or ^{6}Li), the encapsulated volume by the HDPE box, and the number of the sandwich detector in the stack.

GAMBE detection system has been tested in a proton therapy facility for cancer treatment as shown in fig. 7.3. The experimental measurements have been carried out using the handheld configuration, which consists of single sandwich detector with ^{6}LiF film of (1.5 $\pm$ 0.6) mg/cm^2 thick. The detector was positioned at a distance of 75 cm, facing the water phantom with an angle of 45° (see fig. 7.3). The incident proton beam on the water phantom has an energy of 120 MeV. Moreover, the applied bias on the Si sensors of the detector is 20 V and high PHD of 1 MeV is used to reject the background radiation in the field due to the interaction of this energetic beam with the water phantom.

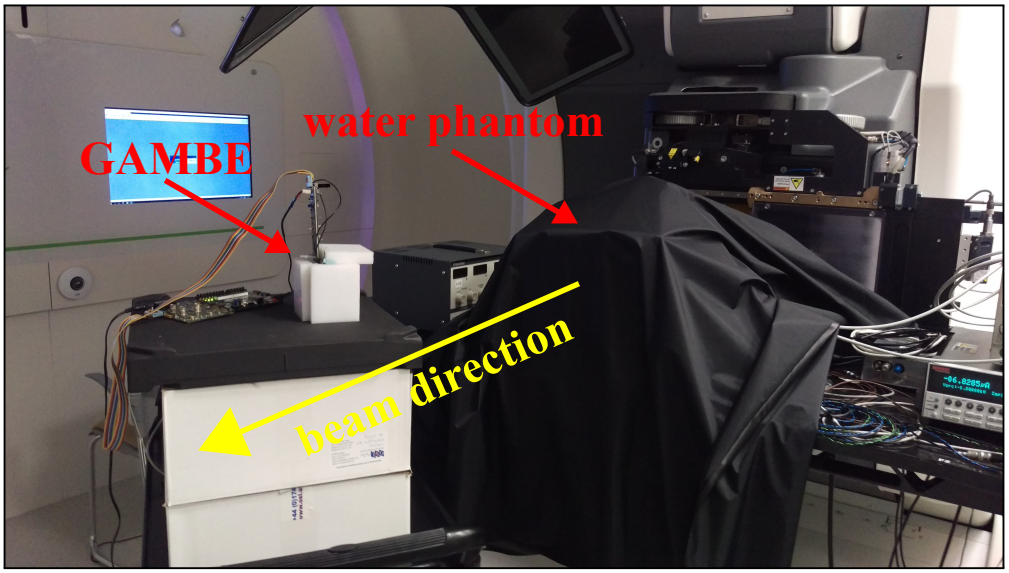

Figure 7.3: Experimental measurements at a proton therapy facility.

The results of this preliminary test show the capability of the detector to detect the produced neutrons as secondary radiation due the interaction of the energetic protons with water, which represents the human body in this experiment. Figure 7.4 presents the spectrum of energy deposited in the Si sensors by the charged particle reaction products due to neutrons being captured in the ^{6}LiF converter film. In addition, this figure presents the coincidence events, which are classed as good events, typical of neutrons induced alpha-triton pairs. Therefore, one of the most important issues to cover in the near future for this research is to do a part of the experimental work in some of the workplaces, where the neutrons

exist in the radiation field in order to improve the statistical study with more experimental conditions and to get a real implementation for this research.

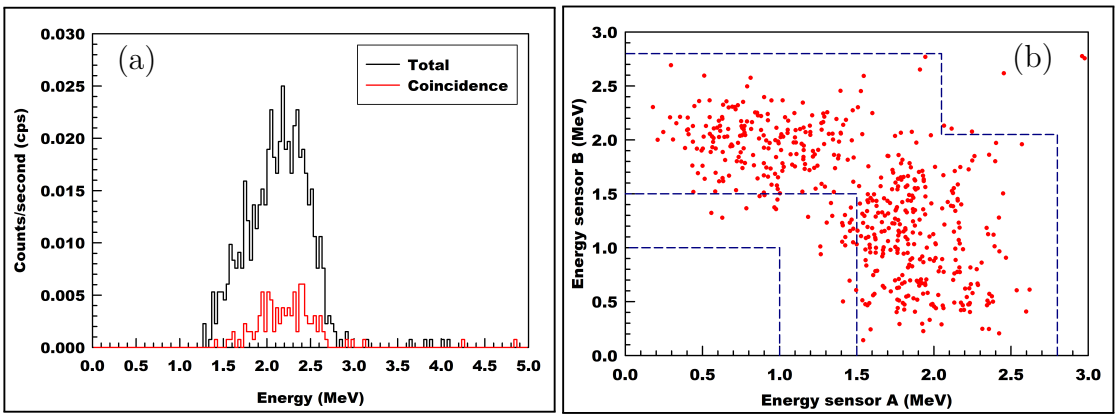

Figure 7.4: Results of testing GAMBE of single sandwich detector at a proton therapy facility: (a) spectrum of energy deposited in Si sensors of the detector, (b) detected events as coincidences.

Most of the facilities and radiation sources necessary for this research such as hospitals, proton therapy facilities, nuclear reactors and neutron sources are restricted areas and not directly accessible. For that, a considerable number of procedures have to be initiated. First of all, it is necessary to construct a new research project in collaboration with one of these facilities such as hospitals or proton therapy centres in order to facilitate the access to neutron sources and proton beam, where the GAMBE detection system can be tested. Secondly, it is also important to develop a new readout electronics, which will be used with the stacked seven sandwich detectors in order to validate the performance of the designed handheld neutron detector. Third, starting on the basis of the achievement obtained from the ^{6}LiF precipitation technique, another deposition technology such as chemical vapour deposition (CVD) has to be employed in order to manufacture a coated silicon sensor with a uniform controllable thickness of the converter over the entire active area of the sensor.

Finally, from the author's point of view, it is hoped that this thesis will encourage to continue the opened research line in the developed innovative silicon radiation detectors for security and medical applications.

Appendices

Appendix A

GAMBE electronic system

A.1 Introduction

Electrical current is induced in the detector, when an ionising radiation goes through it. Therefore, this detector is considered as a current source with an internal resistance and capacitance as shown in fig. A.1a. Even if there is no ionising radiation, there is a small current, which is called leakage current. The detector produces a voltage signal by generating a current within its capacitance. This signal is too small to be detected directly, therefore, it needs to be amplified [114]. This is done by directing the measured voltage into the amplifier, as presented in fig. A.1b. The input voltage of the amplifier modifies its resistance, which is usually a transistor. The change in the resistance modulates the current in the output circuit, resulting in a voltage above the load resistance, which has an associated electronic noise.

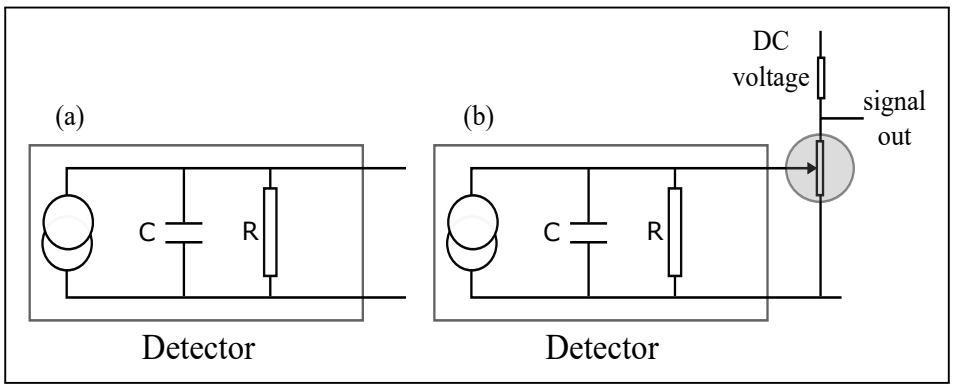

Figure A.1: Electronic circuit which represents a detector. (a) The detector acts as a current source with an internal resistance and a capacitance. (b) The output voltage of the detector is directed to the subsequent processing electronics.

A.2 Silicon sensor characterisation

The production of semiconductor devices depends on the microelectronic technology which makes use of wafers. These wafers are thin slices of a semiconductor material such as silicon (Si), which are altered by means of a series of processing steps like doping, chemical etching, oxidation and deposition of materials, in the clean room facilities [115]. Semiconductor radiation detectors are based on this technology.

The simplest configuration of a silicon particle detector is a reverse biased diode. The diodes used to manufacture the thermal neutron detector, GAMBE, have a p-i-n (PIN) configuration as shown in fig. A.2. These devices are 300 μm thick with an active area of 10×10 mm^2, and a total area of 12.5×12.5 mm^2. The bulk of these diodes consists of high resistivity (10 kΩ·cm) p-type silicon, which is lightly doped with boron (10^{12} particles/cm^{-3}). The surface and the bottom of this bulk is highly doped with phosphorous (10^{18} particles/cm^{-3}) and boron (10^{16} particles/cm^{-3}) by ion implantation process to form highly doped regions of $n^+$and p^+ respectively. These $n^+$and p^+ regions are used as Ohmic contacts in combination with the metallisation that is done with aluminium.

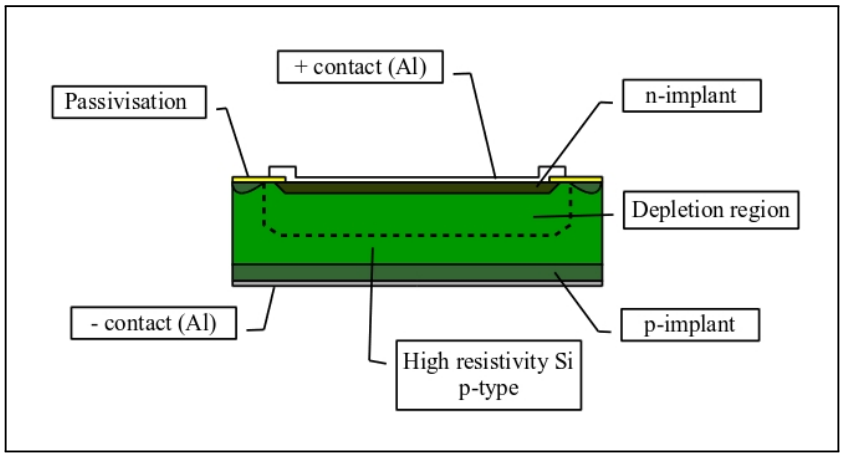

Figure A.2: Schematic of a p-i-n Si semiconductor sensor. The total area including the guard ring is 12.5×12.5 mm^2, with an active area (defined by the n-type implantation) of 10×10 mm^2.

The electrical characterisation of the silicon sensors was performed by using a probe station biasing the sensors with a 2410 Keithley power supply at a controlled temperature with continuous flow of N_2 to reduce the humidity. The I-V and C-V characteristics of the produced devices have been obtained under a reverse bias configuration. In this configuration, a voltage scan from 0 to positive voltage values up to 200 V, where the n-type region connected to the positive terminal of

the keithley and the p-type region connected to the negative (ground) terminal. As a result, it has been found that the full depletion voltage (V_{FD}) of these detectors is 80 V as presented in fig. A.3.

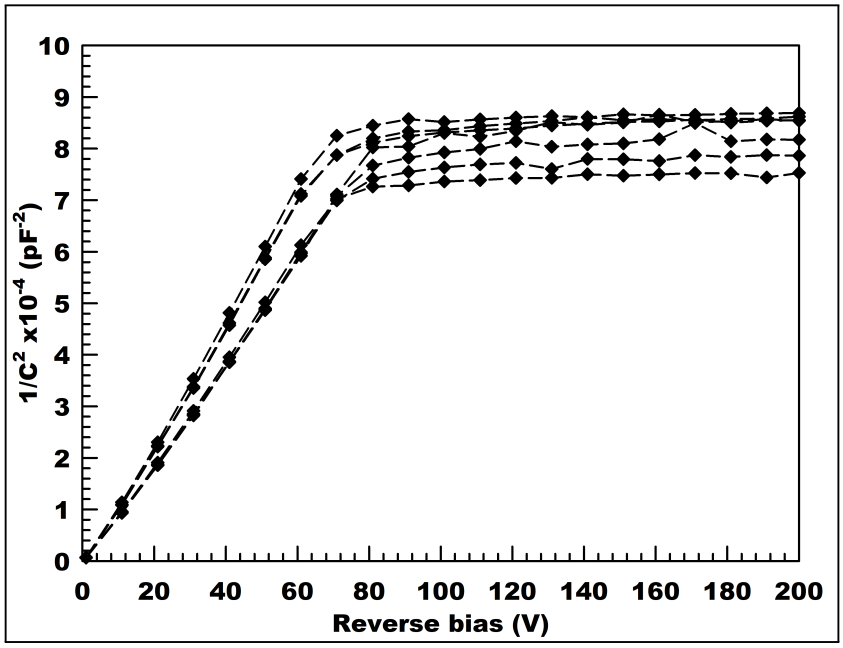

Figure A.3: C−V characteristic curve for 7 PIN diodes - capacitances versus reverse voltage up to 200 V. The full depletion voltage is 80 V.

A.3 Electronic system and pulse processing

There are two modes, which can be used for measuring signals from the radiation detector [36]. The first is the current mode, where the total current of the detector is measured. While, the second is the pulse mode, which counts the individual pulses generated by the ionising radiation, giving a pulse height spectrum. The amplitude of the pulses in most of radiation detectors is proportional to the initial charge signal. Hence, in mixed radiation fields, it is possible to differentiate between pulses coming from different types of radiation by using thresholds.

In this work a pulse counting mode has been applied, where the fundamental output is a burst of charge Q liberated by the interacted triton or alpha particle with the sensitive volume of the detector. The charge Q is proportional to the energy deposited, which is delivered as a transient current. A pulse hight spectrum can be obtained, where the electronics digitises the recorded pulses and sends them to a PC interface. This is iteratively done for a large number of pulses, producing a histogram.

Figure A.4 shows the main components of the readout electronics of the thermal

neutron detection system. The detector converts the energy deposited by the charged particle reaction products into an electrical signal, which is directed to a shaping amplifier, as it can be sees in fig. A.5.

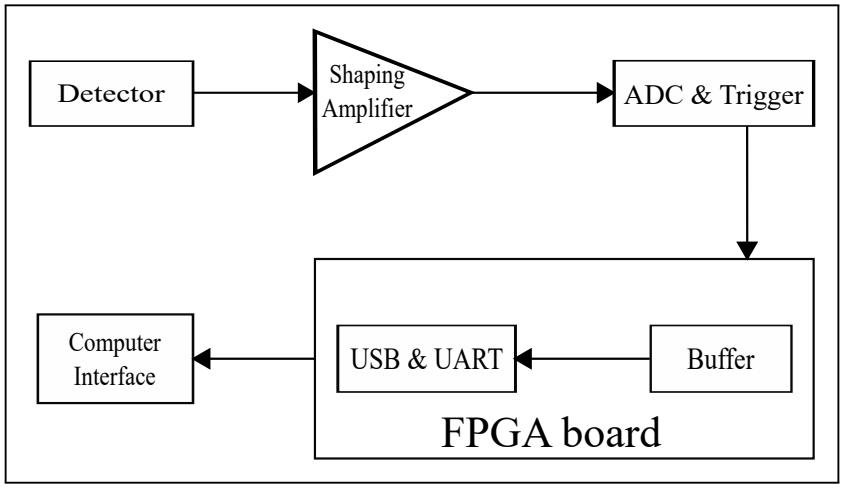

Figure A.4: Schematic diagram of the readout electronic system of the thermal neutron detector.

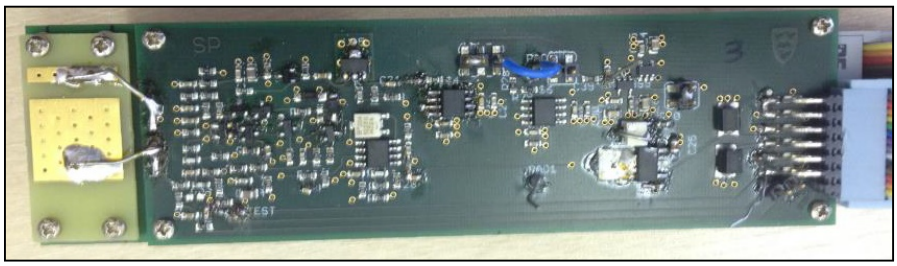

Figure A.5: Photograph of the amplifier board, which delivers the electrical signal from the detector to the subsequent readout electronic system.

The amplifier is an interface with shaping time constant ($\tau \approx 600\ ns$) between the detector and the subsequent processing electronics, where the transient current pulse is integrated into a voltage step ΔV, which is proportional to the liberated charge Q. This voltage step will be converted to an analog voltage pulse with pulse height V_{peak}. The output voltage peak will be moved to a dual analog-to-digital converter, ADC (MAX1183), with sampling rate of 40 mega-samples per second (MSPS), or one sample every 25 ns. The basic function of this ADC is to produce a digital code at its output that is proportional to analog voltage supplied to its input. An ideal ADC would perform a perfectly linear conversion of analog voltage to code value. This code is transmitted to FPGA board with a buffer (size = 1 Mb), which is a temporary holding place for data that are being sent to or received from an external device. This buffer will hold approximately 100

codes to be transmitted by UART (baud rate = 115200 bits per second) through a USB cable to a computer interface within 5.5 ms.

The output of this electronic system is either a count rate (a measurement of the rate of pulses meeting a certain acceptance criteria) or an energy spectrum (a measurement of the distribution of energies deposited by alpha-triton pairs in the silicon diodes). These outputs require accumulation of multiple events, which are produced due to the interaction of charged particles (α/t) produced from thermal neutrons being captured in the converter material. The data acquisition system (DAQ) is able to generate online histograms, trace event by event and record not only the pulse height but also write each pulse trace to a log file. This log file allows the users to do offline analysis of the collected data by using the software codes, which have been written in C++ (see appendix B).

A.3.1 Energy calibration of the system

The default spectrum provided by DAQ is displayed in counts vs. channels, as shown in fig. A.6a. Hence, an energy calibration is required to get the energy spectrum over 1024 channels. This calibration was made by determining the ratio between the channel number and the energy in MeV (MeV/channel). In order to get an accurate energy calibration, the calculation of this MeV/channel ratio is based on the energy of the triton peak from simulations and the height of pulses recorded, when an alpha source of energy 5 MeV was placed in front of silicon sensor. Consequently, the MeV/channel ratio is concluded to be 0.0042 MeV/channel, which is in agreement with the calibrated energy spectrum from the simulation, as displayed in fig. A.6b.

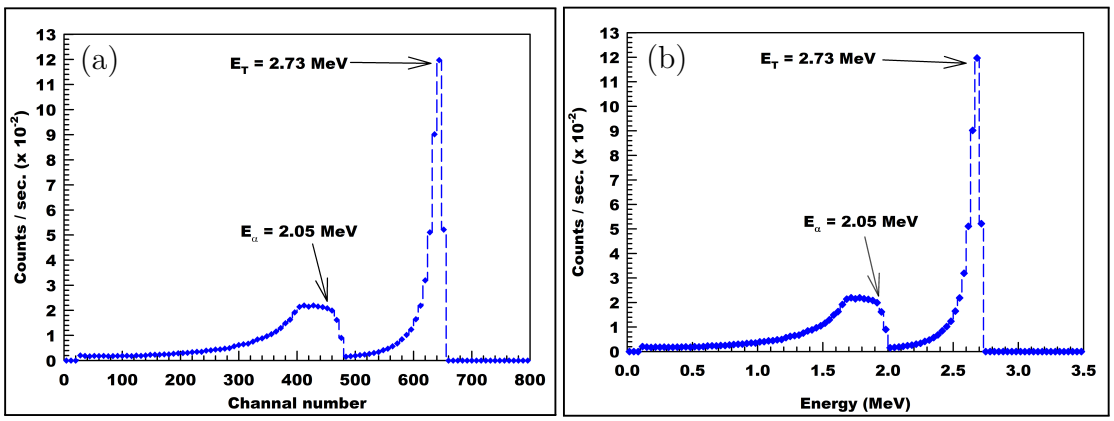

Figure A.6: Transformation from ADC channel number to energy (MeV): (a) counts vs. channel spectrum, (b) calibrated energy spectrum.

A.4 Electronic noise

There are several causes of electronic noise during the experimental measurements. Noise can be picked up from the the electromagnetic radiation which is caused by external devices without any relation to the process of collecting data itself. For instance, noise from digital parts of the electronics and readout computer. This type of noise can be avoided by enclosing the silicon sensors in a box made out of a good conductor, such as aluminium.

There are other types of electronic noise, which depend on intrinsic properties of the semiconductor material. These types are shot and thermal noise [116]. The shot noise is related to the small number of carriers passing through the diode in the absence of radiation, which causes the fluctuations in the leakage current within the detector itself. The thermal noise is due to the Brownian thermal motion of the semiconductor atoms where the thermal velocity is not zero, giving rise to the instantaneous current called thermal or Johnson noise. The main goal for any electronic system is to reduce the generated electronic noise at the beginning of signal processing, where the signal level is at minimum and the noise at this point will undergo the same amplification process as the signal.

The amount of noise added by the preamplifier-amplifier combination is often expressed in terms of the equivalent noise charge (ENC). This ENC is defined as the amount of charge that if applied to the input terminals of the system would give rise to output voltage equal to RMS level of the output due only to noise. Thus, the contribution of electronic noise to FWHM of peaks in the energy spectrum can be calculated from ENC. The equivalent noise charge could be expressed in energy units (eV) by multiplication with the deposited energy required to create one charge carrier (ε). For instance, silicon has $\varepsilon = 3.62$ eV and, thus, the amount of energy equivalent to the noise charge will be $E = 3.62 \times ENC$ [117].

A.4.1 Temperature effect on leakage current

The bare silicon sensors of the sandwich detector configuration have been tested individually at different temperatures to investigate the feasibility of using the thermal neutron detector, GAMBE, at higher temperatures than normal. In this experiment, each silicon sensor was mounted in an aluminium box, where the whole box was placed inside an oven and a bias voltage of 80 V was applied to the sensors. The oven is a Carbolite PF 120 (120 L Volume), where the temperature is raised up to 80 ^{o}C to study its effect on the detector leakage current.

The increment in the temperature (t) up to 80 ^{o}C affects the leakage cur-

rent (I_{lk}) of both Si sensors as presented in table A.1. A linear regression fitting between the natural logarithm of the leakage current and the temperature is accomplished. This regression deduced an equation represents the dependency of the leakage current on the environmental temperature.

Table A.1: The variance of the leakage current upon the temperature.

Temperature (^{o}C)	20	30	40	50	60	70	80
I_{lk} (μA) sensor A	0.004	0.01	0.02	0.06	0.2	0.5	0.99
ln(I_{lk}) $_A$	-5.6	-4.7	-3.8	-2.8	-1.7	-0.6	-0.002
I_{lk} (μA) sensor B	0.03	0.05	0.1	0.2	0.4	0.8	0.99
ln(I_{lk}) $_B$	-3.5	-3	-2.4	-1.7	-1	-0.2	-0.002

The fitted linear relation between the natural logarithm of the leakage current and the temperature of both sensors A and B is shown in fig. A.7 . Moreover, this regression is represented by the eq. (A.1) with a coefficient, R^2, of 0.996 and 0.992 for sensor A and sensor B respectively.

$$ln(I_{lk}) = bt + ln(a) \tag{A.1}$$

where $ln(a)$ and b are the coefficients of regression and their values are presented in table A.2 with an interval of confidence more than 95%.

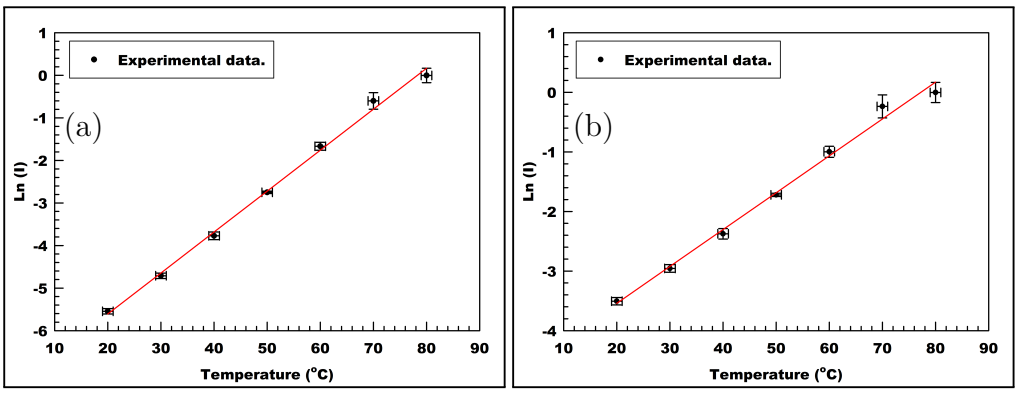

Figure A.7: Linear regression between the natural logarithm of the leakage current and the temperature: (a) Si sensor A, (b) Si sensor B.

The exponential variation of the leakage current of both Si sensors A and B with the environmental temperature is presented in fig. A.8. This figure illustrates that the leakage current increases slightly until 60 ^{o}C, then it will increase rapidly at temperatures higher than 60 ^{o}C. Therefore, it has been concluded that the detector can be used for the neutron detection at different temperatures higher than normal. However, care has to be taken if this temperature goes higher than 60 ^{o}C and the detector has to be monitored all the time. This is due to

Table A.2: Coefficients of linear regression between $ln(I_{lk})$ and temperature (t) for both sensors A and B.

	Coefficients		Standard Error	P-value	Lower 95%	Upper 95%
sensor A	ln(a)	-7.5	0.1	4×10^{-8}	-7.9	-7.2
	b	0.096	0.003	2.5×10^{-7}	0.089	0.102
sensor B	ln(a)	-4.8	0.1	3×10^{-7}	-5.1	-4.4
	b	0.062	0.003	2×10^{-6}	0.055	0.068

that the temperature more than 60 ^{o}C may damage the electronics parts if the measurements have been taken for a long time, where the leakage current goes higher than 1 μA.

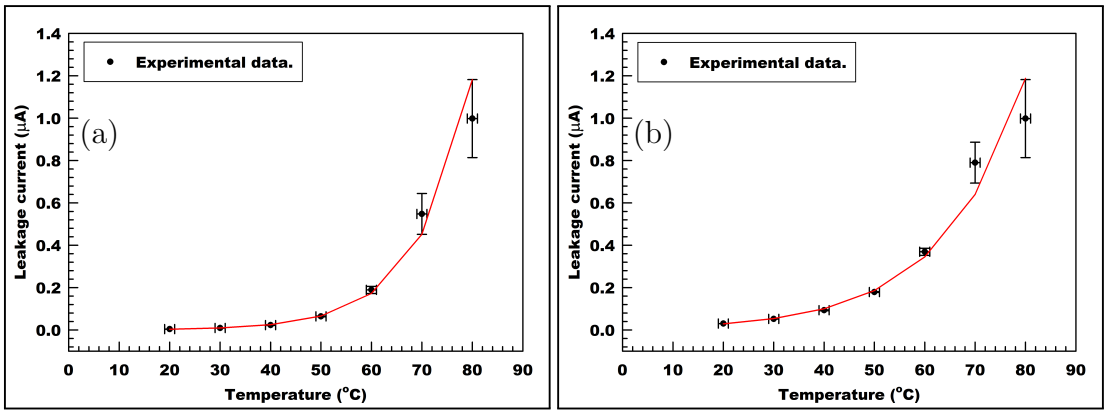

Figure A.8: The variation of the leakage current as a function of the environmental temperature: (a) Si sensor A, (b) Si sensor B.

A.4.2 Parallel electronic noise for both sensors A and B

Parallel electronic noise is a combination of both shot and thermal noises where the shot noise is a series of discrete pulses of equal height arriving randomly in time which is represented by the leakage current. This leakage current $I_{lk} = ne$, where n is the average pulse rate and e is the electron charge.

The specific electronic design of the amplifier circuit for both silicon sensors A and B has a shaping time, $\tau = RC$ of 4.7×10^{-6} s. The ENC is quoted as $\sqrt{N}$, where N is the number of the pulses elapsed during a specific period of time and it equals τn. Hence, the amount of generated energy is equal to $3.62 \times ENC$ eV. Table A.3 shows the calculations to determine the amount of energy related to this shot noise which is dependent on the leakage current of both silicon sensors A and B. These results display that sensor B has electronic noise greater than sensor A especially at a temperature lower than 70 ^{o}C.

Table A.3: The variation of ENC with the leakage current due to the effect of temperature.

Sensor A					
T (^{o}C)	$I_{lk} \times 10^{-6}$ (A)	Flow rate (n) (e/s)	N ($\tau n \times 10^5$)	ENC ($\sqrt{N}$)	Equivalent energy (keV)
20	0.004	2×10^{10}	1	338	1.2
30	0.01	6×10^{10}	3	514	2
40	0.02	1×10^{11}	7	821	3
50	0.06	4×10^{11}	19	1370	5
60	0.19	1×10^{12}	55	2355	8.5
70	0.55	3×10^{12}	161	4009	14.5
80	1	6×10^{12}	293	5411	19.6
Sensor B					
T (^{o}C)	$I_{lk} \times 10^{-6}$ (A)	Flow rate (n) (e/s)	N ($\tau n \times 10^5$)	ENC ($\sqrt{N}$)	Equivalent energy (keV)
20	0.03	2×10^{11}	9	938	3
30	0.05	3×10^{11}	15	1235	5
40	0.1	6×10^{11}	27	1652	6
50	0.2	1×10^{12}	53	2292	8
60	0.4	2×10^{12}	108	3290	12
70	0.8	5×10^{12}	232	4814	17
80	1	6×10^{12}	293	5411	19.6

Thermal noise is due to the thermal motion of the charge carriers in the resistors, especially the feedback resistor. The motion is driven by the thermal energy KT of an electron in a resistor, where K is the Boltzmann constant. This thermal energy generates thermal current ($I_{th} = \frac{V}{R}$), which has been treated as an effective input source of electronic noise such as the shot noise. Therefore, thermal noise (N) is defined according to the following equations as a function of the I_{th}:

$$N = eI_{th}\tau,$$

$$N = e\frac{V}{R}\tau,$$

$$N = \frac{4KT}{R}\tau,$$

where R is the feedback preamplifier resistor and KT is equivalent to the effective

voltage across the preamplifier feedback resistor, giving energy $eV = KT$. Table A.4 presents the equivalent energy due to the variation of the thermal noise with the temperature of both sensors A and B, which are connected to the same electronic design of an amplifier with the same value of R. As can be seen in table A.4, the amount of energy equivalent to the thermal noise is extremely small when it is compared to the equivalent energy of the shot noise. Moreover, the variation of the temperature has small effect on the thermal noise. As a result, the thermal noise can be neglected.

Table A.4: The equivalent energy to the thermal noise for both Si sensors.

T (^{o}C)	$N = \frac{4KT}{R}\tau$	$ENC = \sqrt{N}$	Equivalent energy (keV)
20	4.8×10^{-10}	2.1×10^{-5}	$7.9{\times}10^{-8}$
30	4.9×10^{-10}	2.2×10^{-5}	$8{\times}10^{-8}$
40	5.1×10^{-10}	2.3×10^{-5}	$8.2{\times}10^{-8}$
50	5.2×10^{-10}	2.3×10^{-5}	$8.3{\times}10^{-8}$
60	5.4×10^{-10}	2.3×10^{-5}	$8.4{\times}10^{-8}$
70	5.6×10^{-10}	2.4×10^{-5}	$8.5{\times}10^{-8}$
80	5.7×10^{-10}	2.4×10^{-5}	$8.7{\times}10^{-8}$

The variation of total equivalent energy due to the parallel electronic noise of both silicon sensors A and B is presented in table A.5. This table displays the dependency of parallel electronic noise on the shot noise which is related to the leakage current. Also, it shows that the equivalent energy of electronic noise in sensor B is greater than that in sensor A. However, the level of this equivalent energy due to the electronic noise of both silicon sensors is still accepted and can be completely eliminated by applying a threshold of 100 keV.

The relation between the equivalent energy of the electronic noise (ENC) and the temperature is examined through a linear regression between the natural logarithm of the ENC and the temperature. The regression suggests the following equation with R^2-values of 0.996, 0.992 for sensor A and sensor B respectively.

$$ln(ENC) = ln(a) + bt$$

where $ln(a)$ and b are the coefficients of the regression and their values are presented in table A.6 with an interval of confidence of 95%. The relation between the equivalent energy of the electronic noise in the system and the environmental temperature is an exponential relationship as shown in fig. A.9.

Table A.5: The variation of the equivalent energy due to electronic noise with temperature for both sensors A and B.

Sensor A			
T (^{o}C)	Shot noise energy (keV)	Thermal noise energy (keV)	Electronic noise energy (keV)
20	1.2	7.9×10^{-8}	1.2
30	2	8×10^{-8}	2
40	3	8.2×10^{-8}	3
50	5	8.3×10^{-8}	5
60	8.5	8.4×10^{-8}	8.5
70	14.5	8.5×10^{-8}	14.5
80	19.6	8.7×10^{-8}	19.6
Sensor B			
T (^{o}C)	Shot noise energy (keV)	Thermal noise energy (keV)	Electronic noise energy (keV)
20	3	7.9×10^{-8}	3
30	5	8×10^{-8}	5
40	6	8.2×10^{-8}	6
50	8	8.3×10^{-8}	8
60	12	8.4×10^{-8}	12
70	17	8.5×10^{-8}	17
80	19.6	8.7×10^{-8}	19.6

Table A.6: Coefficients of linear regression between $ln(ENC)$ and temperature (t).

	Coefficients		Standard Error	P-value	Lower 95%	Upper 95%
sensor A	ln(a)	-0.8	0.1	9×10^{-5}	-1	-0.6
	b	0.05	0.001	2.5×10^{-7}	0.04	0.05
sensor B	ln(a)	0.6	0.1	3×10^{-4}	0.4	0.8
	b	0.03	0.001	2×10^{-6}	0.027	0.034

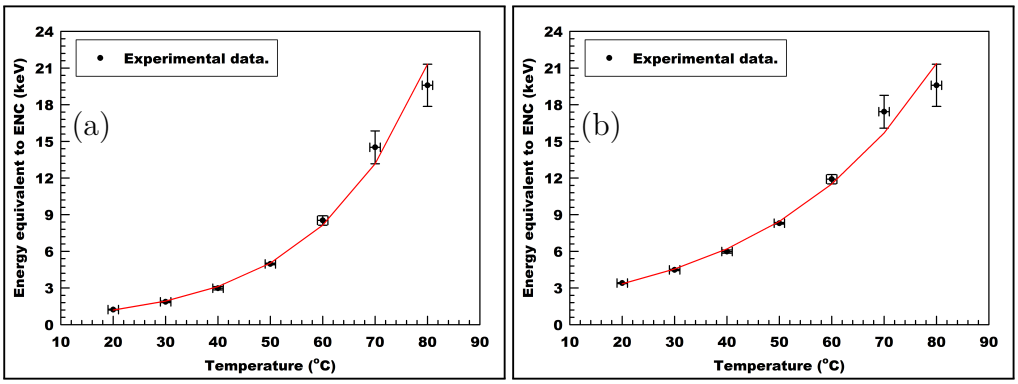

Figure A.9: The variation of the electronic noise energy equivalent as a function of the environmental temperature: (a) Si sensor A, (b) Si sensor (B).

Finally, the GAMBE system shows the capability to work at higher environmental temperatures up to 80 ^oC with limited electronic noise. This electronic noise has no effect on the signal recorded by the two silicon sensors facing the conversion layer due to the applied PHD of 100 keV.

Appendix B

Data acquisition codes

B.1 Presort data into a text file

```
#include <iostream>
#include <fstream>
#include <string>
#include <sstream>
#include <iomanip>
#include <math.h>
#include <stdio.h>
#include <cstring>
#include <cstdlib>
#include <stdlib.h>
#include <vector>
#include <math.h>
#include <algorithm>
using namespace std;
inline size_t word_count(std::istream& is)
{
  size_t c = 0;
  for(std::string w; is >> w; ++c);
  return c;
}
inline size_t word_count(const std::string& str)
{
  std::istringstream iss(str);
  return word_count(iss);
}
std::vector <int> getTrace(std::istream& trc);
std::vector <int> getTrace(std::istream& trc)
{
  std::vector<int> trace;
```

```
30   for(int a; trc >> a; trace.push_back(a));
31   return trace;
32 }
33 std::vector <double> fitPulse(vector<int> trace, vector<int> gdPulse,
       double base, double target);
34 std::vector <double> fitPulse(vector<int> trace, vector<int> gdPulse,
       double base, double target)
35 {
36   vector <double> fit;
37   unsigned size = trace.size();
38   if (size != 0 && size==gdPulse.size()){
39 //perform linear regression fit of measured trace 'good pulse'
40 double xsum, ysum, xysum, x2sum, y2sum;
41         xsum=ysum=xysum=x2sum=y2sum=0;
42   for(int i=0; i!=size; i++)
43   {
44     double y(base-trace[i]);
45     double x(gdPulse[i]);
46     xysum+=y*x; x2sum+=x*x; y2sum+=y*y; xsum+=x; ysum+=y;
47   }
48     double m = (xysum/size)/(x2sum/size);
49 // r-regression factor
50     double r = (xysum/size)/sqrt((x2sum/size)*(y2sum/size));
51     int biggest;
52   biggest = *max_element(gdPulse.begin(), gdPulse.end());
53   double hFit = biggest * m;
54   fit.push_back(r);
55   if (r>target)fit.push_back(hFit);
56   else fit.push_back(0);
57   else {fit.push_back(0);fit.push_back(0);}
58   return fit;
59 }
60 int main()
61 {
62 unsigned total = 0, goodCount = 0, countA = 0, countB = 0, coincCount
       = 0;
63 double Time = 0;
64 const int traceSize = 39;
65 const int eventSize = 83;
66 char *inputName = "DAQ LOG FILE.txt";
67 char *outputDir = "presort";
68 std::ios::openmode iostemp1; iostemp1 = std::ios::out|std::ios::app;
69 ifstream myFile (inputName);
70 if (myFile.is_open())
71     {
72   string line;
```

```
73   while (getline(myFile,line))
74   {
75     int myint;
76     int eventNo, hA, hB;
77     double tStamp;
78     bool detectorTrigger;
79     vector<int> traceA, traceB;
80     size_t words = word_count(line);
81     std::istringstream event(line);
82     stringstream trcA, trcB;
83     event >> eventNo >> tStamp >> hA >> hB;
84     for(int i=0; i != traceSize; ++i)
85     {event >> myint; traceA.push_back(myint);trcA << myint << " ";}
86     for(int i=0; i != traceSize; ++i)
87     {event >> myint; traceB.push_back(myint);trcB << myint << " ";}
88     event >> detectorTrigger;
89     string trA=trcA.str();
90     bool rightSize=false;
91 if (words==eventSize && traceA.size()==traceSize && traceB.size()==
      traceSize) rightSize=true;
92 if (rightSize==false) {continue;}
93 else{
94 total++; Time = tStamp;
95 std::istringstream gdPulseA("0  1 1 1 2 2 2 2 3 3   3 3 3 3 7 25  77
       161 229 250 233 195 152 111 76  46    22  3 -13 -26 -35 -43 -47
     -50 -51 -52 -53 -53 -53");
96 std::istringstream gdPulseB("0  0 0 0 0 0 0 0 0 0 0 0 0 1 4 25  77
     149 199 208 187 151 112 77  47  23  3 -12 -24 -34 -41 -45 -48 -49
     -50 -50 -50 -49 -49");
97 vector<int> goodPulseA, goodPulseB;
98 for (int a; gdPulseA >> a; goodPulseA.push_back(a));
99 for (int a; gdPulseB >> a; goodPulseB.push_back(a));
100 double baselineA=920, baselineB=915;
101 double target = 0.75;
102 vector<double>fitA =fitPulse(traceA, goodPulseA, baselineA, target);
103 vector<double>fitB =fitPulse(traceB, goodPulseA, baselineB, target);
104 bool goodEvent = false, goodA = false;
105 bool goodB = false, coincident = false;
106 double thresh = 24;
107 if (fitA[0] > target && fitA[1] > thresh ){goodA = true; countA++;}
      else{fitA[1]=0;}
108 if (fitB[0] > target && fitB[1] > thresh ){goodB = true; countB++;}
      else{fitB[1]=0;}
109 if (goodA == true && goodB == true){coincident=true; coincCount++;}
110 if (goodA == true || goodB == true){goodEvent=true;  goodCount++;}
111 char name1[80];  strcpy (name1,outputDir);
```

```
112 strcat (name1,"/PRESORTDATA.txt");
113 std::ofstream outPut1(name1, iostemp1);
114 outPut1 <<  line   << endl;
115 outPut1.close();
116 char name2[80];  strcpy (name2,outputDir);
117 strcat (name2,"/OUTPUT.txt");
118 std::ofstream outPut2(name2, iostemp1);
119 if (goodEvent==true){
120 outPut2<<eventNo<<" "<<tStamp<<" "<<fitA[1]<<" "<<fitB[1]<<" "<<
      detectorTrigg<<" "<<coincident<<endl;
121 outPut2.close();}
122 char name3[80];  strcpy (name3,outputDir);
123 strcat (name3,"/COINCIDENCES.txt");
124 std::ofstream outPut3(name3, iostemp1);
125 if (coincident == true)
126 {outPut3<<eventNo<<" "<< tStamp<<" "<<fitA[1]<<" "<<fitB[1]<<" "<<
      detectorTrigger<<" "<<coincident<< endl;
127 outPut3.close();}
128 char name4[80];  strcpy (name4,outputDir);
129 strcat (name4,"/BADEVENTSA.txt");
130 std::ofstream outPut4(name4, iostemp1);
131 if (goodA==false)
132 {outPut4 <<eventNo<<" "<<fitA[0]<<fitA[1]<<" "<<trcA.str()<< endl;
133 outPut4.close();}
134 char name5[80];  strcpy (name5,outputDir);
135 strcat (name5,"/GOODEVENTSA.txt");
136 std::ofstream outPut5(name5, iostemp1);
137 if(goodA == true)
138 {outPut5<<eventNo<<" "<<fitA[0]<< fitA[1]<<" "<<trcA.str()<< endl;
139 outPut5.close();}
140 char name6[80];  strcpy (name6,outputDir);
141 strcat (name6,"/BADEVENTSB.txt");
142 std::ofstream outPut6(name6, iostemp1);
143 if (goodB==false)
144 {outPut6<<eventNo<<" "<<fitB[0]<<fitB[1]<<" "<<trcB.str()<< endl;
145 outPut6.close();}
146 char name7[80];  strcpy (name7,outputDir);
147 strcat (name7,"/GOODEVENTSB.txt");
148 std::ofstream outPut7(name7, iostemp1);
149 if(goodB == true)
150 {outPut7<<eventNo<<" "<<fitB[0]<<fitB[1]<<" "<<trcB.str()<< endl;
151 outPut7.close();}
152     }
153   }
154   myFile.close();
155 }
```

```
156 else cout << "Unable to open file";
157 char file1[80];  strcpy (file1,outputDir);
158 strcat (file1,"/SUMMARY.txt");
159 char nfrun1[200];
160 sprintf(nfrun1,file1 );
161 std::ofstream runout1(nfrun1);
162 runout1<<"Good events:       "<< goodCount << std::endl;
163 runout1<<"Good counts A:     "<< countA << std::endl;
164 runout1<<"Good counts B:     "<< countB << std::endl;
165 runout1<<"Coincidences:      "<< coincCount << std::endl;
166 runout1<<"Singles:           "<< goodCount - coincCount << std::endl;
167 runout1<<"Total events:      "<< total << std::endl;
168 runout1<<"Bad events:        "<< total - goodCount << std::endl;
169 runout1<<"Time elapsed (s)   "<< Time << std::endl;
170 runout1<<"COUNT RATES (cps) "<< std::endl;
171 runout1<<"Good event rate:   "<< goodCount/Time << std::endl;
172 runout1<<"Good count rate A:"<< countA/Time << std::endl;
173 runout1<<"Good count rate B:"<< countB/Time << std::endl;
174 runout1<<"Coincidence rate: "<< coincCount/Time << std::endl;
175 runout1<<"Singles rate       "<< (goodCount - coincCount)/Time << std
      ::endl;
176 runout1<<"Total rate:        "<< total/Time << std::endl;
177 runout1<<"Bad event rate     "<< (total-goodCount)/Time << std::endl;
178 runout1.close();
179   return 0;
180 }
```

B.2 Data offline analysis

```
// reading a text file
#include <iostream>
#include <fstream>
#include <string>
#include <sstream>
#include <iomanip>
#include <math.h>
#include <stdio.h>
#include <cstring>
#include <cstdlib>
using namespace std;
inline size_t word_count(std::istream& is)
{
  size_t c = 0;
  for(std::string w; is >> w; ++c);
  return c;
}
inline size_t word_count(const std::string& str)
{
  std::istringstream iss(str);
  return word_count(iss);
}
int main (int argc, char *argv[])
{
double mevPerChan = 240;
char *pFilename = "presort/OUTPUT.txt";
char *pOutput = "rates";
int sumgoodA=0;
int sumgoodB=0;
int goodEvents=0;
int coincidences=0;
int neutrons1=0;
int neutrons2=0;
int neutronCounts1=0;
int neutronCounts2=0;
int singles=0;
int total=0;
double Time=0;
int coincA=0; int coincB=0;
int singlesA=0; int singlesB=0;
int counts=0;
int coincCounts=0;
int countsA=0;
```

```
44 int countsB=0;
45 double tBin = 3600;
46 double tMax=tBin;
47 int lim1=120; int lim2=660; int lim3=490;
48 //HISTOGRAM BINS
49 int binsize;
50 int N;
51 int Elow, Ehigh, Elowj, Ehighj;
52 binsize=8;
53 N = 1024/binsize;
54 //HISTOGRAM ARRAYS
55 int AplusB[256], AplusB2[256], AplusBsq[256], AplusBsq2[256];
56 for(int i=0; i<N*2; i++)
57 {AplusB[i]=0;AplusB2[i]=0;AplusBsq[i]=0;AplusBsq2[i]=0;}
58 int NA[128],NA1[128],NA2[128],NA3[128],NA4[128],NA5[128],NA6[128],NA7
       [128],NA8[128],NA9[128],NA10[128];
59 int NB[128],NB1[128],NB2[128],NB3[128],NB4[128],NB5[128],NB6[128],NB7
       [128],NB8[128],NB9[128],NB10[128];
60 for(int i=0; i<N; i++)
61 {NA[i]=0;NA1[i]=0;NA2[i]=0;NA3[i]=0;NA4[i]=0;NA5[i]=0;NA6[i]=0;NA7[i
       ]=0;NA8[i]=0;NA9[i]=0;NA10[i]=0;
62 NB[i]=0;NB1[i]=0;NB2[i]=0;NB3[i]=0;NB4[i]=0;NB5[i]=0;NB6[i]=0;NB7[i
       ]=0;NB8[i]=0;NB9[i]=0;NB10[i]=0;}
63 //matrix arrays
64 int mat1[128][128], mat2[128][128];
65 for(int i=0; i<N; i++){
66 for(int j=0; j<N; j++){ mat1[i][j]=0;  mat2[i][j]=0;}}
67   std::ios::openmode iostemp1; iostemp1 = std::ios::out|std::ios::app
       ;
68   string line;
69   ifstream myfile (pFilename);
70   if (myfile.is_open())
71   {
72     int A[100];
73     while ( std::getline (myfile,line) )
74     {
75     int n=0;
76     double hA=0;
77     double hB=0;
78     bool CT=false;
79     bool goodEvent = false;
80     bool coincident=false;
81     bool neutron1=false;
82     bool neutron2=false;
83     double tstamp=0;
84     std::istringstream event(line);
```

```
85      size_t words = word_count(line);
86        event >> n
87              >> tstamp
88              >> hA
89              >> hB
90              >> CT
91              >> coincident;
92        if (words != 6){continue;} else{
93 total++;
94 Time=tstamp;
95 bool Agood=false;
96 bool Bgood=false;
97 if(hA>=24){Agood=true;sumgoodA++;}else{Agood=false;}
98 if(hB>=24){Bgood=true;sumgoodB++;}else{Bgood=false;}
99 if(Agood==true || Bgood==true){goodEvent==true; goodEvents++;}
100 else{goodEvent==false;}
101 bool abovethresholdA, abovethresholdB;
102 if (hA<24) {abovethresholdA = false;}
103 else {abovethresholdA=true;}
104 if (hB<24) {abovethresholdB = false;}
105 else {abovethresholdB=true;}
106 counts++;
107 if (coincident==true){coincCounts++; coincidences++;}
108 if (Agood==true){countsA++;}
109 if (Bgood==true){countsB++;}
110 if ((hA>=lim1 && hA<=lim2 && hB <=lim3)||(hB>=lim1 && hB<=lim2 && hA
    <=lim3))
111 {neutron1=true;neutrons1++;neutronCounts1++;
112 if(Agood==true && Bgood==true){neutron2=true;neutrons2++;
    neutronCounts2++;}}
113 if(Agood!=Bgood){singles++;}
114 if(Agood==true && Bgood==false){singlesA++;}
115 if(Bgood==true && Agood==false){singlesB++;}
116 // fill arrays for sum of energy
117 for(int i=0; i<256; i++){ Elow=0+binsize*i; Ehigh=0+binsize*(i+1);
118 if(hA+hB>= Elow && hA + hB < Ehigh){AplusB[i]++;}
119 if(coincident==true && hA+hB>= Elow && hA + hB < Ehigh){AplusB2[i
    ]++;}
120 if(sqrt(hA*hA+hB*hB)>= Elow && sqrt(hA*hA + hB*hB) < Ehigh){AplusBsq[
    i]++;}
121 if(coincident==true && sqrt(hA*hA+hB*hB)>= Elow && sqrt(hA*hA + hB*hB
    ) < Ehigh){AplusBsq2[i]++;}}
122 for(int i=0; i<128; i++){ Elow=0+binsize*i; Ehigh=0+binsize*(i+1);
123 if(Agood==true && hA >= Elow && hA < Ehigh){NA[i]++;}
     // All sensor A
124 if(Bgood==true && hB >= Elow && hB < Ehigh){NB[i]++;}
```

```
      // All sensor B
125 if(Agood==true && Bgood==true && hA >= Elow && hA < Ehigh){NA1[i]++;}
      // Coincidence A
126 if(Agood==true && Bgood==true && hB >= Elow && hB < Ehigh){NB1[i]++;}
      // Coincidence B
127 if(Bgood==false && hA >= Elow && hA < Ehigh){NA2[i]++;}
      // Single A
128 if(Agood==false && hB >= Elow && hB < Ehigh){NB2[i]++;}
      // Single B
129 for (int j=0; j<128; j++){  Elowj=0+binsize*j; Ehighj=0+binsize*(j+1)
    ;
130 if(Agood==true && Bgood==true && hA >= Elow && hA < Ehigh && hB >=
    Elowj && hB < Ehighj)
131 {mat1[i][j]++;}
132 }}
133   char name1[80];  strcpy (name1,pOutput);
134   strcat (name1,"/RATE1.dat");
135   char name2[80];  strcpy (name2,pOutput);
136   strcat (name2,"/RATE2.dat");
137     if (Time>tMax){
138   counts=counts-1;
139   if (coincident==true){coincCounts=coincCounts-1;}
140   if (Agood==true){countsA=countsA-1;}
141     if (Bgood==true){countsB=countsB-1;}
142   if (neutron1==true){neutronCounts1=neutronCounts1-1;}
143   if (neutron2==true){neutronCounts2=neutronCounts2-1;}
144 std::ofstream outPut1(name1, iostemp1);
145 outPut1 << tMax           << " "
146         << counts         << " "
147         << coincCounts    << " "
148         << countsA        << " "
149         << countsB        << " "
150         << neutronCounts1 << " "
151         << neutronCounts2 << endl;
152 outPut1.close();
153 std::ofstream outPut2(name2, iostemp1);
154 outPut2 << tMax             << " "
155         << counts/tBin      << " "
156         << coincCounts/tBin << " "
157         << countsA/tBin     << " "
158         << countsB/tBin     << " "
159         << neutronCounts1/tBin << " "
160         << neutronCounts2/tBin << endl;
161 outPut2.close();
162 cout    << tMax        << " "
163         << counts      << " "
```

```
164         << coincCounts << " "
165         << countsA     << " "
166         << countsB     << endl;
167 if (Time>tBin && Time<2*tBin){
168   char file6[80];  strcpy (file6,pOutput);
169   strcat (file6,"/1hr.dat");
170   char nfrun6[200];
171 sprintf(nfrun6,file6 );
172 std::ofstream runout6(nfrun6);
173 for(int i=0; i<N; i++)
174 {  runout6   <<  (i+0.5)*binsize << " "
175  <<  (i+0.5)*binsize/mevPerChan  << " "
176 << NA[i]  << " "
177 << NB[i]    << " "
178 << NA1[i]   << " "
179 << NB1[i]   << " "
180 << NA2[i]   << " "
181 << NB2[i]   << " "
182 << NA[i]  /tBin << " "
183 << NB[i]  /tBin << " "
184 << NA1[i] /tBin << " "
185 << NB1[i] /tBin << " "
186 << NA2[i] /tBin << " "
187 << NB2[i] /tBin << " "
188 << std::endl;}
189       runout6.close();
190   char file7[80];  strcpy (file7,pOutput);
191   strcat (file7,"/1hrmatrix.dat");
192   char nfrun7[200];
193   sprintf(nfrun7,file7 );
194  std::ofstream runout7(nfrun7);
195  for(int i=0; i<N; i++)
196  {
197  for(int j=0; j<N; j++)
198  {runout7   <<   mat1[i][j] << " "; }
199   runout7   << std::endl;}
200   runout7.close();
201   char file8[80];  strcpy (file8,pOutput);
202   strcat (file8,"/1hrcpsmatrix.dat");
203   char nfrun8[200];
204   sprintf(nfrun8,file8 );
205   std::ofstream runout8(nfrun8);
206   for(int i=0; i<N; i++)
207   {
208   for(int j=0; j<N; j++)
209   {runout8 << mat1[i][j]/tBin << " "; }
```

```
210     runout8 << std::endl;}
211     runout8.close();
212     char file9[80];  strcpy (file9,pOutput);
213     strcat (file9,"/1hrSUMMARY.txt");
214     char nfrun9[200];
215     sprintf(nfrun9,file9 );
216     std::ofstream runout9(nfrun9);
217 runout9<<"Good counts A:          "<<sumgoodA << std::endl;
218 runout9<<"Good counts B:          "<<sumgoodB << std::endl;
219 runout9<<"Coincidences:           "<<coincidences << std::endl;
220 runout9<<"Singles:                "<<singles << std::endl;
221 runout9<<"Singles sensor A:       "<<singlesA << std::endl;
222 runout9<<"Singles sensor B:       "<<singlesB << std::endl;
223 runout9<<"Neutron energy (either):"<<neutrons1 << std::endl;
224 runout9<<"Neutron energy (both):  "<<neutrons2 << std::endl;
225 runout9<<"Total events:           "<<total << std::endl;
226 runout9<<"Time elapsed (s)        "<<Time << std::endl;
227 runout9<<"COUNT RATES (cps)       "<<std::endl;
228 runout9<<"Good count rate A:      "<<sumgoodA/Time << std::endl;
229 runout9<<"Good count rate B:      "<<sumgoodB/Time << std::endl;
230 runout9<<"Coincidence rate:       "<<coincidences/Time << std::endl;
231 runout9<<"Singles rate            "<<singles/Time << std::endl;
232 runout9<<"Singles rate A          "<<singlesA/Time << std::endl;
233 runout9<<"Singles rate B          "<<singlesB/Time << std::endl;
234 runout9<<"Neutron energy (either):"<<neutrons1/Time << std::endl;
235 runout9<<"Neutron energy (both):  "<<neutrons2/Time << std::endl;
236 runout9<<"Total rate:             "<<total/Time << std::endl;
237 runout9.close();
238   char name12[80];  strcpy (name12,pOutput);
239   strcat (name12,"/1hrCOINCIDENT.txt");
240   std::ofstream outPut12(name12, iostemp1);
241   if(coincident==true){
242   outPut12  << n        << " "
243             << tstamp   << " "
244             << hA       << " "
245             << hB       << " "
246             << CT       << " "
247             << coincident  << endl;
248   outPut12.close();}
249 }
250   tMax=tMax+tBin;
251   counts=1;
252 if (coincident==true){coincCounts=1;}else{coincCounts=0;}
253 if (Agood==true){countsA=1;}else{countsA=0;}
254 if (Bgood==true){countsB=1;}else{countsB=0;}
255 if (neutron1==true){neutronCounts1=1;}else{neutronCounts1=0;}
```

```
256 if (neutron2==true){neutronCounts2=1;}else{neutronCounts2=0;}
257 }
258     char name11[80];  strcpy (name11,pOutput);
259     strcat (name11,"/COINCIDENT.txt");
260     std::ofstream outPut11(name11, iostemp1);
261     if(coincident==true){
262   outPut11<<  n << " "
263             <<   tstamp      << " "
264             <<   hA          << " "
265             <<   hB          << " "
266             <<   CT        << " "
267             <<   coincident  << endl;
268   outPut11.close();}
269 }
270 }
271     myfile.close();
272 }
273   else cout << "Unable to open file";
274   char file1[80];  strcpy (file1,pOutput);
275   strcat (file1,"/SUMMARY.txt");
276   char nfrun1[200];
277   sprintf(nfrun1,file1 );
278   std::ofstream runout1(nfrun1);
279 runout1<<"Good counts A:          "<<sumgoodA << std::endl;
280 runout1<<"Good counts B:          "<<sumgoodB << std::endl;
281 runout1<<"Coincidences:           "<<coincidences << std::endl;
282 runout1<<"Singles:                "<<singles << std::endl;
283 runout1<<"Singles sensor A:       "<<singlesA << std::endl;
284 runout1<<"Singles sensor B:       "<<singlesB << std::endl;
285 runout1<<"Neutron energy (either):"<<neutrons1 << std::endl;
286 runout1<<"Neutron energy (both):  "<<neutrons2 << std::endl;
287 runout1<<"Good events:            "<<goodEvents << std::endl;
288 runout1<<"Total events:           "<<total << std::endl;
289 runout1<<"Time elapsed (s)        "<<Time << std::endl;
290 runout1<<"COUNT RATES (cps)       "<<std::endl;
291 runout1<<"Good count rate A:      "<<sumgoodA/Time << std::endl;
292 runout1<<"Good count rate B:      "<<sumgoodB/Time << std::endl;
293 runout1<<"Coincidence rate:       "<<coincidences/Time << std::endl;
294 runout1<<"Singles rate            "<<singles/Time << std::endl;
295 runout1<<"Singles rate A          "<<singlesA/Time << std::endl;
296 runout1<<"Singles rate B          "<<singlesB/Time << std::endl;
297 runout1<<"Neutron energy (either):"<<neutrons1/Time << std::endl;
298 runout1<<"Neutron energy (both):  "<<neutrons2/Time << std::endl;
299 runout1<<"Total rate:             "<<total/Time << std::endl;
300     runout1.close();
301   char file2[80];  strcpy (file2,pOutput);
```

```
302   strcat (file2,"/histogram1.dat");
303   char nfrun2[200];
304   sprintf(nfrun2,file2 );
305   std::ofstream runout2(nfrun2);
306 for(int i=0; i<N; i++)
307 {  runout2   <<  (i+0.5)*binsize  << " "
308  <<  (i+0.5)*binsize/mevPerChan  << " "
309 << NA[i]  << " "
310 << NB[i]    << " "
311 << NA1[i]   << " "
312 << NB1[i]   << " "
313 << NA2[i]   << " "
314 << NB2[i]   << " "
315 << std::endl;}
316       runout2.close();
317   char file3[80];  strcpy (file3,pOutput);
318   strcat (file3,"/cps1.dat");
319   char nfrun3[200];
320   sprintf(nfrun3,file3 );
321   std::ofstream runout3(nfrun3);
322 for(int i=0; i<N; i++)
323 {  runout3   <<  (i+0.5)*binsize  << " "
324  <<  (i+0.5)*binsize/mevPerChan  << " "
325 << NA[i]  /Time     << " "
326 << NB[i]  /Time     << " "
327 << NA1[i] /Time     << " "
328 << NB1[i] /Time     << " "
329 << NA2[i] /Time   << " "
330 << NB2[i] /Time   << " "
331 << std::endl;}
332       runout3.close();
333   char file4[80];  strcpy (file4,pOutput);
334   strcat (file4,"/matrix.dat");
335   char nfrun4[200];
336   sprintf(nfrun4,file4 );
337  std::ofstream runout4(nfrun4);
338 for(int i=0; i<N; i++)
339 {
340 for(int j=0; j<N; j++)
341 { runout4   <<   mat1[i][j] << " "; }
342   runout4   << std::endl;}
343   runout4.close();
344   char file5[80];  strcpy (file5,pOutput);
345   strcat (file5,"/cpsmatrix.dat");
346   char nfrun5[200];
347   sprintf(nfrun5,file5 );
```

```
348   std::ofstream runout5(nfrun5);
349 for(int i=0; i<N; i++)
350 {
351 for(int j=0; j<N; j++)
352 { runout5   <<   mat1[i][j]/Time << " "; }
353   runout5   << std::endl;}
354   runout5.close();
355   char sums[80];   strcpy (sums,pOutput);
356   strcat (sums,"/sums1.dat");
357   char nfrun6[200];
358   sprintf(nfrun6,sums );
359   std::ofstream runout6(nfrun6);
360 for(int i=0; i<N*2; i++)
361 {  runout6   <<  (i+0.5)*binsize  << " "
362  <<  (i+0.5)*binsize/mevPerChan  << " "
363 << AplusB[i]  << " "
364 << AplusB2[i]   << " "
365 << AplusBsq[i]  << " "
366 << AplusBsq2[i] << " "
367 << std::endl;}
368       runout6.close();
369   char sumscps[80];   strcpy (sumscps,pOutput);
370   strcat (sumscps,"/sumscps.dat");
371   char nfrun7[200];
372   sprintf(nfrun7,sumscps );
373   std::ofstream runout7(nfrun7);
374 for(int i=0; i<N*2; i++)
375 {  runout7   <<  (i+0.5)*binsize  << " "
376  <<  (i+0.5)*binsize/mevPerChan  << " "
377  << AplusB[i]/Time       << " "
378  << AplusB2[i] /Time  << " "
379  << AplusBsq[i] /Time << " "
380  << AplusBsq2[i] /Time  << " "
381  << std::endl;}
382       runout7.close();
383   return 0;
384 }
```

Appendix C

GEANT4 codes

C.1 Detector construction

```
#include "DetectorConstruction.hh"
#include "DetectorMessenger.hh"
#include "SteppingAction.hh"
#include "G4RunManager.hh"
#include "G4NistManager.hh"
#include "G4Box.hh"
#include "G4Cons.hh"
#include "G4Orb.hh"
#include "G4Sphere.hh"
#include "G4Trd.hh"
#include "G4LogicalVolume.hh"
#include "G4PVPlacement.hh"
#include "G4SystemOfUnits.hh"
#include "G4Material.hh"
#include "G4SDManager.hh"
#include "G4GeometryManager.hh"
#include "G4PhysicalVolumeStore.hh"
#include "G4LogicalVolumeStore.hh"
#include "G4SolidStore.hh"
#include "G4VisAttributes.hh"
#include "G4Colour.hh"
DetectorConstruction::DetectorConstruction():
diodeLog1(0),diodeLog2(0),diodePhys1(0),diodePhys2(0), worldPhys(0),
    foilBox(0), foilLog(0),foilPh(), filmMaterial(0),BGOPhys(0)
{
thickness = 1*micrometer; //Set a default thickness of reactive film
detectorMessenger = new DetectorMessenger(this);
}
DetectorConstruction::DetectorConstruction(){ }
```

```
29 G4VPhysicalVolume DetectorConstruction::Construct()
30 {
31 return ConstructDetectors();
32 }
33 G4VPhysicalVolume* DetectorConstruction::ConstructDetectors()
34 {
35 G4String symbol, name;   //a=mass of a mole
36 G4double a, z, density;  //z=mean number of protons
37 G4int iz, n;             //iz=number of protons  in an isotope
38 G4int ncomponents, natoms;
39 G4double abundance, fractionmass;
40 G4NistManager* nist = G4NistManager::Instance();
41 G4Material* world_mat = nist->FindOrBuildMaterial("G4_AIR");
42 G4Material* silicon = nist->FindOrBuildMaterial("G4_Si");
43 G4Material* aluminium = nist->FindOrBuildMaterial("G4_Al");
44 density=0.462*g/cm3; a=6.00*g/mole; z=3;
45 name="6Li";
46 G4Element* Li = new G4Material(name, z, a, density);
47 G4Element* F = new G4Element("Fluorine",symbol="F",z=9,a=19*g/mole);
48 G4Element* H = new G4Element("Hydrogen","H",z= 1,a=1.01*g/mole);
49 G4Element* O  = new G4Element("Oxygen","O",z= 8,a=16.00*g/mole);
50 G4Material* LiF = new G4Material("6LiF", density= 2.539* g/cm3,
       ncomponents=2);
51 LiF->AddElement(F, natoms=1);
52 LiF->AddElement(Li, natoms=1);
53 G4GeometryManager::GetInstance()->OpenGeometry();
54 G4PhysicalVolumeStore::GetInstance()->Clean();
55 G4LogicalVolumeStore::GetInstance()->Clean();
56 G4SolidStore::GetInstance()->Clean();
57 SetFilmMaterial("6Li");
58 // Define the geometry of world
59   G4double world_hx = 0.5*m;
60   G4double world_hy = 0.5*m;
61   G4double world_hz = 0.5*m;
62 G4Box* worldBox = new G4Box("World", world_hx, world_hy, world_hz);
63 G4LogicalVolume* worldLog= new G4LogicalVolume(worldBox, world_mat, "
       World");
64 worldPhys = new G4PVPlacement(0,        //no rotation
65              G4ThreeVector(),          //at (0,0,0)
66              worldLog,                 //its logical volume
67              "World",                  //its name
68              0,                        //its mother  volume
69              false,                    //no boolean operation
70              0);                       //copy number
71 //set gap between sensor and foil
72   G4double gap = 300*micrometer;
```

```
73 //Define detector width and height
74   G4double diode_hy = 5*mm;
75   G4double diode_hz = 5*mm;
76   G4double diode_hx = 150* micrometer;
77 //thickness of aluminium contact
78   G4double contact_hx = 0.05*micrometer;
79 // Lithium 6 layer "Foil"
80   G4double foil_hx = thickness/2;
81 //G4Box* foilBox
82   foilBox = new G4Box("Foil", foil_hx, diode_hy, diode_hz);
83
84 //Changeing material command
85   foilLog   = new G4LogicalVolume(foilBox, L6, "Foil");
86   foilLog    = new G4LogicalVolume(foilBox, LiF, "Film");
87 // Aluminium contact layer "Contact"
88 G4Box* contactBox = new G4Box("Contact", contact_hx, diode_hy,
      diode_hz);
89 G4LogicalVolume* contactLog = new G4LogicalVolume(contactBox,
      aluminium, "Contact");
90 G4double contactpos_x = foil_hx + contact_hx + gap/2;
91 G4double pos_y = 0*mm;
92 G4double pos_z = 0*mm;
93
94 G4VPhysicalVolume* contactPhys  = new G4PVPlacement(0, G4ThreeVector(
       contactpos_x, pos_y, pos_z), contactLog, "Contact", worldLog,
      false, 0);
95 G4VPhysicalVolume* contactPhys2 = new G4PVPlacement(0, G4ThreeVector
      (-contactpos_x + gap/2, pos_y, pos_z), contactLog, "Contact",
      worldLog, false, 0);
96 // Silicon detectors "Diode"
97 diodeBox = new G4Box("Diode", diode_hx, diode_hy, diode_hz);
98 diodeLog1 = new G4LogicalVolume(diodeBox, silicon, "Diode1");
99 diodeLog2 = new G4LogicalVolume(diodeBox, silicon, "Diode2");
100 G4double diodepos_x = contactpos_x + contact_hx + diode_hx;
101 diodePhys1 = new G4PVPlacement(0,  G4ThreeVector(diodepos_x, pos_y,
      pos_z),  diodeLog1, "Diode1", worldLog, false, 0);
102 diodePhys2 = new G4PVPlacement(0,  G4ThreeVector(-diodepos_x + gap/2,
       pos_y, pos_z), diodeLog2, "Diode2", worldLog, false, 0);
103 return worldPhys;
104 }
105 void DetectorConstruction::SetThickness(G4double val)
106 {
107   thickness = val;
108 }
109 void DetectorConstruction::SetFilmMaterial(G4String materialChoice)
110 {
```

```
111   G4Material* pttoMaterial = G4Material::GetMaterial(materialChoice);
112   if (pttoMaterial) filmMaterial = pttoMaterial;
113 }
114 void DetectorConstruction::UpdateGeometry()
115 {
116   G4RunManager::GetRunManager()->DefineWorldVolume(ConstructDetectors
        ());
117 }
```

C.2 Primary generator action

```
#include "PrimaryGeneratorAction.hh"
#include "G4LogicalVolumeStore.hh"
#include "G4LogicalVolume.hh"
#include "G4Box.hh"
#include "G4RunManager.hh"
#include "G4ParticleGun.hh"
#include "G4ParticleTable.hh"
#include "G4ParticleDefinition.hh"
#include "G4SystemOfUnits.hh"
#include "Randomize.hh"
PrimaryGeneratorAction* PrimaryGeneratorAction::fgInstance = 0;
const PrimaryGeneratorAction* PrimaryGeneratorAction::Instance()
{
  return fgInstance;
}
PrimaryGeneratorAction::PrimaryGeneratorAction()
: G4VUserPrimaryGeneratorAction(),
  fParticleGun1(0)
{
  G4int n_particle = 1;
  fParticleGun1  = new G4ParticleGun(n_particle);
  fgInstance = this;
}
PrimaryGeneratorAction::~PrimaryGeneratorAction()
{
  delete fParticleGun1;
 fgInstance = 0;
}
void PrimaryGeneratorAction::GeneratePrimaries(G4Event* anEvent)
{
  // default particle kinematic
  G4ParticleTable* particleTable = G4ParticleTable::GetParticleTable
    ();
  G4String particleName;
  G4ParticleDefinition* particle  = particleTable->FindParticle(
    particleName="alpha");
  fParticleGun1->SetParticleDefinition(particle);
  fParticleGun1->SetParticleEnergy(2.05*MeV);
  G4double envSizeX = 0;
  G4double envSizeY = 0;
  G4double envSizeZ = 0;
  G4LogicalVolume* envLV = G4LogicalVolumeStore::GetInstance()->
    GetVolume("Foil");
```

```
41   G4Box* envBox = NULL;
42   if ( envLV ) envBox = dynamic_cast<G4Box*>(envLV->GetSolid());
43   if ( envBox ) {
44     envSizeX = envBox->GetXHalfLength()*2.;
45     envSizeY = envBox->GetYHalfLength()*2.;
46     envSizeZ = envBox->GetZHalfLength()*2.;
47   }
48   else  {
49     G4cerr << "Envelope volume of box shape not found." << G4endl;
50     G4cerr << "Perhaps you have changed geometry." << G4endl;
51     G4cerr << "The gun will be placed in the center." << G4endl;
52   }
53   G4double size = 1;
54   G4double x0 = size * envSizeX * (G4UniformRand()-0.5);
55   G4double y0 = size * envSizeY * (G4UniformRand()-0.5);
56   G4double z0 = size * envSizeZ * (G4UniformRand()-0.5);
57   G4double  Pi = 3.141592654;
58   G4double   phi= Pi* G4UniformRand();
59   G4double   theta = 2.*Pi* G4UniformRand();
60   G4double   ux= sin(theta) * cos(phi);
61 //Following line makes all alphas decays go towards detector 1 (and
     therefore tritons to detector 2)
62  G4double   uy= sin(theta) * sin(phi);
63  G4double   uz =cos(theta);
64  G4double   rando= G4UniformRand();
65  fParticleGun1->SetParticlePosition(G4ThreeVector(x0, y0, z0));
66  fParticleGun1->SetParticleMomentumDirection(G4ThreeVector(ux, uy, uz
     ));
67 //following generates the alpha
68   fParticleGun1->GeneratePrimaryVertex(anEvent);
69   G4ParticleDefinition* particle2  = particleTable->FindParticle(
     particleName="triton");
70   fParticleGun1->SetParticleDefinition(particle2);
71   fParticleGun1->SetParticleEnergy(2.73* MeV);
72   fParticleGun1->SetParticleMomentumDirection(G4ThreeVector(-ux, -uy,
     -uz));
73 //followiing generates the triton
74  fParticleGun1->GeneratePrimaryVertex(anEvent);
75 }
```

C.3 Stepping action

```
#include "SteppingAction.hh"
#include "EventAction.hh"
#include "DetectorConstruction.hh"
#include "G4SystemOfUnits.hh"
#include "G4Step.hh"
#include "G4RunManager.hh"
#include "G4UnitsTable.hh"
SteppingAction::SteppingAction(DetectorConstruction* det, EventAction
    * evt)
: detector(det), eventaction(evt)
    ,G4UserSteppingAction()
{ }
SteppingAction::~SteppingAction()
{ }
void SteppingAction::UserSteppingAction(const G4Step* step)
{
    G4VPhysicalVolume* volume = step->GetPreStepPoint()->
    GetTouchableHandle()->GetVolume();
// collect energy and track length step by step
 G4double edep = step->GetTotalEnergyDeposit();
 if (volume == detector->GetDetector1()) eventaction->AddDet1(edep);
 if (volume == detector->GetDetector2()) eventaction->AddDet2(edep);
  eventaction->AddWorld(edep);
 G4int evtNb =eventaction->GetEventNumber();
if (evtNb == 0) {
    eventaction->SaveDetectorParameters(detector->GetThickness());
  }
}
```

C.4 Run action

```
#include "RunAction.hh"
#include "DetectorConstruction.hh"
#include "G4RunManager.hh"
#include "G4UnitsTable.hh"
#include "G4Run.hh"
#include "G4SystemOfUnits.hh"
#include <fstream>
#include "G4ios.hh"
#include <iostream>
RunAction::RunAction()
{}
RunAction::~RunAction()
{}
void RunAction::BeginOfRunAction(const G4Run* aRun)
{
G4cout << "### Run " << aRun->GetRunID() << " start." << G4endl;
G4cout << std::setw(12) << "Event#" <<  std::setw(12)  << "World" <<
    std::setw(12)  << "Energy1" << std::setw(12)  << "Energy2" <<
    G4endl;

G4RunManager::GetRunManager()->SetRandomNumberStore(true);

//initialize cumulative quantities
  sumEDet1 = sum2EDet1 = 0.0;
  sumEDet2 = sum2EDet2 = 0.0;
   threshDet1 = 100.0 * keV;
   threshDet2 = 100.0 * keV;
   aboveThreshDet1 = 0;
   aboveThreshDet2 = 0;
   aboveThreshBoth = 0;
   goodEvents = 0;
   inwindowSingle = 0;
   inwindowDouble = 0;
   ratio1=0;

N=50;
M=30;
for(G4int i=0; i<N; i++){b[i]=0; c[i]=0;}
for(G4int i=0; i<N; i++){b[i]=0;c[i]=0;d[i]=0; e[i]=0; f[i]=0; h[i
    ]=0;}
for(G4int i=0; i<N; i++){nE[i]=0; rmsE[i]=0; bE[i]=0; lE[i]=0;}
sumb=sumc=sumd=sume=sumf=sumh=sumnE=sumrmsE=0;
Elow = 0*keV; Ehigh= 0*keV; binsize=100*keV; binsize2=0.5;
```

```
41 binsizemat=100*keV; Elowj = 0*keV; Ehighj= 0*keV;
42 for(G4int i=0; i<M; i++){for(G4int j=0; j<M; j++){ mat[i][j]=0;}}
43 for(G4int i=0; i<M; i++){for(G4int j=0; j<N; j++){ mat[i][j]=0;}}
44 for(G4int i=0; i<N; i++){rat[i]=0;}
45 sumrat=0;
46 }
47
48 void RunAction::fillPerEvent(G4double EDet1, G4double EDet2, G4int
     NbEvent)
49 {
50   G4double lim1, lim2, lim3;
51   lim1 = 1.5 * MeV; lim2 = 2.75 * MeV; lim3 = 2.05 * MeV;
52
53 //accumulate statistic
54   Coincident= goodEvent = good1 = good2 = false;
55   if (EDet1 > threshDet1) {aboveThreshDet1++; good1=true;}
56   if (EDet2 > threshDet2) {aboveThreshDet2++; good2=true;}
57   if ((EDet1 > threshDet1) && (EDet2 > threshDet2)) {aboveThreshBoth
      ++; Coincident=true;}
58   if ((EDet1 > threshDet1) || (EDet2 > threshDet2)) {goodEvents++;
      goodEvent=true;}
59   if ((EDet1 > lim1  && EDet1 < lim2 && EDet2 < lim3) || (EDet2 >
      lim1  && EDet2 < lim2 && EDet1 < lim3)) {inwindowSingle++; if (
      Coincident==true) inwindowDouble++;}
60
61   sumEDet1 += EDet1;  sum2EDet1 += EDet1*EDet1;
62   sumEDet2 += EDet2;  sum2EDet2 += EDet2*EDet2;
63
64 //following fills bins for doubles (coincidences) spectrum
65 for(G4int i=0; i<N; i++){ Elow=0+binsize*i; Ehigh=0+binsize*(i+1);
66 if (Coincident==true &&(EDet1 >= Elow) && (EDet1 < Ehigh)) {b[i]++;
     sumb++;}}
67
68 //following fills bins for sensor 1 spectrum (all events)
69 for(G4int i=0; i<N; i++){ Elow=0+binsize*i; Ehigh=0+binsize*(i+1);
70 if (good1==true && (EDet1 >= Elow) && (EDet1 < Ehigh)) {c[i]++; sumc
     ++;}}
71
72 //doubles spectrum, summed energy from both detectors
73 if ((EDet1 > threshDet1) && (EDet2 > threshDet2)) {
74 for(G4int i=0; i<N; i++){ Elow=0+binsize*i; Ehigh=0+binsize*(i+1);
75 if (((EDet1 + EDet2) >= Elow) && ((EDet1 + EDet2) < Ehigh)) {d[i]++;
     sumd++;}}}
76
77 //singles spectrum, summed energy from both detectors
78 for(G4int i=0; i<N; i++){ Elow=0+binsize*i; Ehigh=0+binsize*(i+1);
```

```
79 if (((EDet1+EDet2) >= Elow) && ((EDet1+EDet2) < Ehigh)) {e[i]++; sume
       ++;}}
80
81 //following fills bins for doubles (coincidences) spectrum detector 2
82 for(G4int i=0; i<N; i++){ Elow=0+binsize*i; Ehigh=0+binsize*(i+1);
83 if (Coincident==true &&(EDet2 >= Elow) && (EDet2 < Ehigh)) {f[i]++;
       sumf++;}}
84
85 //following fills bins for singles spectrum detector 2
86 for(G4int i=0; i<N; i++){ Elow=0+binsize*i; Ehigh=0+binsize*(i+1);
87 if (good2==true && (EDet2 >= Elow) && (EDet2 < Ehigh)) {h[i]++; sumh
       ++;}}
88
89 if ((EDet1 > threshDet1) && (EDet2 > threshDet2)){
90 if (EDet1 >= EDet2) ratio1=EDet1/EDet2; else ratio1=EDet2/EDet1;
91 } else ratio1=0;
92
93 //if (EDet2 < EDet1) ratio1=EDet2/EDet1;
94 for(G4int i=0; i<N; i++){ Elow=0+binsize2*i; Ehigh=0+binsize2*(i+1);
95 if ((ratio1 >= Elow) && (ratio1 < Ehigh)) {rat[i]++; sumrat++;}}
96 G4double bigE =0;
97 G4double littleE =0;
98 if (EDet1>=EDet2) {bigE=EDet1;littleE=EDet2;} else {bigE=EDet2;
       littleE=EDet1;}
99
100 G4double newE=0;
101 newE=bigE+littleE/5.3;
102
103 if ((EDet1 > threshDet1) && (EDet2 > threshDet2)){
104 for(G4int i=0; i<N; i++){ Elow=0+binsize*i; Ehigh=0+binsize*(i+1);
105 if ((newE >= Elow) && (newE < Ehigh)) {nE[i]++; sumnE++;}}
106 }
107
108 if ((EDet1 > threshDet1) && (EDet2 > threshDet2)){
109 for(G4int i=0; i<N; i++){ Elow=0+binsize*i; Ehigh=0+binsize*(i+1);
110 if ((bigE >= Elow) && (bigE < Ehigh)) bE[i]++;
111 if ((littleE >= Elow) && (littleE < Ehigh)) lE[i]++;
112 }}
113
114 if ((EDet1 > threshDet1) && (EDet2 > threshDet2)){
115 for(G4int i=0; i<M; i++){ Elow=0+binsizemat*i; Ehigh=0+binsizemat*(i
       +1);
116 for(G4int j=0; j<M; j++){ Elowj=0+binsizemat*j; Ehighj=0+binsizemat*(
       j+1);
117 if ((EDet1 >= Elow) && (EDet1 < Ehigh) && (EDet2 >= Elowj) && (EDet2
       < Ehighj)) {mat[i][j]++;}}}}
```

```
118
119  if ((EDet1 > threshDet1) && (EDet2 > threshDet2)){
120 for(G4int i=0; i<N; i++){ Elow=0+binsize*i; Ehigh=0+binsize*(i+1);
121 if (sqrt(EDet1*EDet1+EDet2*EDet2) >= Elow && sqrt(EDet1*EDet1+EDet2*
      EDet2) < Ehigh) {rmsE[i]++; sumrmsE++;}}}
122
123 //Following lines write to file a list of energy values
124 // 'events1.dat' contains all good events 'events2.dat' is
      coincidences only
125 std::ios::openmode iostemp2; iostemp2 = std::ios::out|std::ios::app;
126 G4double Energy1=EDet1;
127 G4double Energy2=EDet2;
128
129 std::ofstream outPutEvents("events1.dat", iostemp2);
130 if (goodEvent == true){
131 outPutEvents << NbEvent << " "
132              << Energy1 << " "
133              << Energy2 << G4endl;
134 outPutEvents.close();}
135
136 std::ofstream outPutEvents2("events2.dat", iostemp2);
137 if (Coincident == true){
138 outPutEvents2 << NbEvent << " "
139               << Energy1 << " "
140               << Energy2 << G4endl;
141 outPutEvents2.close();}
142
143 std::ofstream outPutEvents3("LOG FILE.dat", iostemp2);
144 if (goodEvent == true){
145 outPutEvents3 << NbEvent << " "
146               << NbEvent << " "
147               << G4int(Energy1 /MeV*240) << " "
148               << G4int(Energy2 /MeV*240) << " "
149               << Coincident << " "
150               << Coincident << G4endl;
151 outPutEvents3.close();}
152
153 std::ofstream outPutEvents4("OUTPUT.dat", iostemp2);
154 if (goodEvent == true){
155 outPutEvents4 << NbEvent << " "
156               << NbEvent << " "
157               << Energy1 << " "
158               << Energy2 << " "
159               << Coincident << " "
160               << Coincident << G4endl;
161 outPutEvents4.close();}
```

```
162 }
163 void RunAction::EndOfRunAction(const G4Run* aRun)
164 {
165 G4int NbOfEvents = aRun->GetNumberOfEvent();
166 if (NbOfEvents == 0) return;
167 sumEDet1 /= NbOfEvents; sum2EDet1 /= NbOfEvents;
168 sumEDet2 /= NbOfEvents; sum2EDet2 /= NbOfEvents;
169 G4double rmsEDet1 = sum2EDet1 - sumEDet1*sumEDet1;
170 G4double rmsEDet2 = sum2EDet2 - sumEDet2*sumEDet2;
171 if (rmsEDet1 >0.) rmsEDet1 = std::sqrt(rmsEDet1); else rmsEDet1 = 0.;
172 if (rmsEDet2 >0.) rmsEDet2 = std::sqrt(rmsEDet2); else rmsEDet2 = 0.;
173   G4cout
174 << "\n----------------------End of Run------------------------------\n"
175 << "\n mean Energy in Detector1 :" << G4BestUnit(sumEDet1,"Energy")
176 << " +- "                          << G4BestUnit(rmsEDet1,"Energy")
177 << "\n mean Energy in Detector2 :" << G4BestUnit(sumEDet2,"Energy")
178 << " +- "                          << G4BestUnit(rmsEDet2,"Energy")
179      << G4endl;
180
181 G4double efftot = (G4double)goodEvents / NbOfEvents;
182 G4double erefftot = sqrt(efftot * (1.0 - efftot) / NbOfEvents);
183 G4double eff1 = (G4double)aboveThreshDet1 / NbOfEvents;
184 G4double ereff1 = sqrt(eff1 * (1.0 - eff1) / NbOfEvents);
185 G4double eff2 = (G4double)aboveThreshDet2 / NbOfEvents;
186 G4double ereff2 = sqrt(eff2 * (1.0 - eff2) / NbOfEvents);
187 G4double effBoth = (G4double)aboveThreshBoth / NbOfEvents;
188 G4double ereffBoth = sqrt(effBoth * (1.0 - effBoth) / NbOfEvents);
189 G4double weffSingle = (G4double)inwindowSingle / NbOfEvents;
190 G4double erweffSingle = sqrt(weffSingle * (1.0 - weffSingle) /
    NbOfEvents);
191 G4double weffDouble = (G4double)inwindowDouble / NbOfEvents;
192 G4double erweffDouble = sqrt(weffDouble * (1.0 - weffDouble) /
    NbOfEvents);
193
194 // neutron capture cross section of 6Li
195   G4double cross = 940 *barn;
196   G4double NA = 6.022e23;
197 //*************** change for material command ****************//
198
199   // Following line is correct for lithium metal film material
200      G4double density = 0.462 *g/cm3; G4double weight = 6*g;
201
202   // Following line is correct for LiF film material
203      G4double density = 2.539 *g/cm3; G4double weight = 25*g;
204
205 //  G4double Prob = cross/cm2 * Thickness/cm *NA/(weight/g) *density
```

```
    /(g/cm3);
206 G4double Prob = 1 - exp(-cross/cm2 * Thickness/cm *NA/(weight/g) *
    density/(g/cm3));
207 G4double absEfftot = efftot * 100 * Prob;
208 G4double erabsEfftot = erefftot * 100 * Prob;
209 G4double absEff1 = eff1 * 100 * Prob;
210 G4double erabsEff1 = ereff1 * 100 * Prob;
211 G4double absEff2 = eff2 * 100 * Prob;
212 G4double erabsEff2 = ereff2 * 100 * Prob;
213 G4double absEff = effBoth * 100 * Prob;
214 G4double erabsEff = ereffBoth * 100 * Prob;
215 G4double windowEffSingle = weffSingle * 100 * Prob;
216 G4double erwindowEffSingle = erweffSingle * 100 * Prob;
217 G4double windowEffDouble = weffDouble * 100 * Prob;
218 G4double erwindowEffDouble = erweffDouble * 100 * Prob;
219
220 G4cout
221 << "\n  NUmber of hits: \n"
222 << "All event: " << goodEvents
223 << "\n Detector1: " << aboveThreshDet1
224 << "\n Detector2: " << aboveThreshDet2
225 << "\n Coincidence: " << aboveThreshBoth
226 << "\n Neutron conversion single event > 1.5 MeV: " << inwindowSingle
227 << "\n Neutron conversion coincident event > 1.5 MeV: " <<
    inwindowDouble
228 << "\n Efficiency: "
229 << "\n Total detection efficiency: " << absEfftot << "+-" <<
    erabsEfftot
230 << "\n Detector1: " << absEff1 << "+-" << erabsEff1
231 << "\n Detector2: " << absEff2 << "+-" << erabsEff2
232 << "\n Both detectors: " << absEff << "+-" << erabsEff
233 << "\n window: " << windowEffSingle << "+-" << erwindowEffSingle
234 << "\n window+coinc: " << windowEffDouble << "+-" <<
    erwindowEffDouble
235 << G4endl;
236
237 char nfrun2[200];
238 sprintf(nfrun2,"output/run%d_doubles.dat",aRun->GetRunID() );
239 G4cout << "Name of file: " << nfrun2 << G4endl;
240 std::ofstream runout2(nfrun2);
241 for(G4int i=0; i<N; i++){  runout2      << b[i] <<  std::endl;   }
242 runout2.close();
243
244 char nfrun3[200];
245 sprintf(nfrun3,"output/run%d_singles.dat",aRun->GetRunID() );
246 std::ofstream runout3(nfrun3);
```

```
247 for(G4int i=0; i<N; i++){  runout3      << c[i] <<  std::endl;   }
248 runout3.close();
249
250 char nfrun4[200];
251 sprintf(nfrun4,"output/run%d_spectra.dat",aRun->GetRunID() );
252 std::ofstream runout4(nfrun4);
253 runout4 << NbOfEvents << " events, thickness of reactive film (um) =
      " << Thickness/micrometer << std::endl;
254 runout4   << "energy(keV) doubles singles doublessum singlessum" <<
      std::endl;
255    runout4   <<   " Total " << sumb << " " << sumc  << " " << sumd <<
       " " << sume << std::endl;
256 for(G4int i=0; i<N; i++)
257 {runout4 << (i+0.5)*binsize/keV << " " << b[i] << " " << c[i] << " "
      << d[i] << " " << e[i] << std::endl;}
258 runout4.close();
259
260 char nfrun5[200];
261 sprintf(nfrun5,"output/run%d_hist.dat",aRun->GetRunID() );
262 std::ofstream runout5(nfrun5);
263 runout5   << NbOfEvents << " events, thickness of reactive film (um)
      = " << Thickness/micrometer << std::endl;
264 runout5 << "energy(keV) singles1 singles2 doubles1 doubles2
      singlessum doublessum singlesall doublesall" <<  std::endl;
265 runout5 << "Total" << sumc << " " << sumh  << " " << sumb  << " " <<
      sumf << " " << sume << " " << sumd     << " " << sumb+sumc << " "
      << sumh + sumf << std::endl;
266 for(G4int i=0; i<N; i++)
267 {runout5 << (i+0.5)*binsize/keV << " " << c[i] << " " << h[i] << " "
      << b[i] << " " << f[i] << " " << e[i] << " " << d[i] << " " << c[i
      ]+b[i] << " " << h[i]+f[i] << std::endl;}
268 runout5.close();
269
270 char nfrun6[200];
271 sprintf(nfrun6,"output/run%d_mat.dat",aRun->GetRunID() );
272 std::ofstream runout6(nfrun6);
273 for(G4int i=0; i<M; i++)
274 {
275 for(G4int j=0; j<M; j++)
276 { runout6   <<   mat[i][j] << " "; }
277   runout6   << std::endl;}
278   runout6.close();
279
280 char nfrun7[200];
281 sprintf(nfrun7,"output/run%d_mat2.dat",aRun->GetRunID() );
282 std::ofstream runout7(nfrun7);
```

```
283 for(G4int i=0; i<M; i++)
284 {
285 for(G4int j=0; j<N; j++)
286 { runout7  <<  mat2[i][j] << " "; }
287   runout7  << std::endl;}
288   runout7.close();
289
290 std::ios::openmode iostemp1; iostemp1 = std::ios::out|std::ios::app;
291
292 std::ofstream outPut1("output/out1.dat", iostemp1);
293 outPut1 << aRun->GetRunID() <<  "  " << Thickness/micrometer << "
       "  << absEff1  << "    "<<  erabsEff1  <<  G4endl;
294 outPut1.close();
295
296 std::ofstream outPut2("output/out2.dat", iostemp1);
297 outPut2 << aRun->GetRunID() <<  Thickness/micrometer << "    " <<
     absEff2  << "    "<<  erabsEff2  <<  G4endl;
298 outPut2.close();
299
300 std::ofstream outPutBoth("output/both.dat", iostemp1);
301 outPutBoth <<  aRun->GetRunID() << Thickness/micrometer << "    "
     <<  absEff  <<  "    "<<  erabsEff  <<  G4endl;
302 outPutBoth.close();
303
304 std::ofstream outPutBig("output/numberoutput.dat", iostemp1);
305 outPutBig <<  aRun->GetRunID()      << "  "
306           <<  Thickness/micrometer << "  "
307           <<  NbOfEvents           << "  "
308           <<  goodEvents           << "  "
309           <<  aboveThreshDet1      << "  "
310           <<  aboveThreshDet2      << "  "
311           <<  aboveThreshBoth      << "  "
312           <<  inwindowSingle       << "  "
313           <<  inwindowDouble       <<  G4endl;
314 outPutBig.close();
315
316 std::ofstream outPutBig2("output/effoutput.dat", iostemp1);
317 outPutBig2 <<  aRun->GetRunID()      << "  "
318            <<  Thickness/micrometer << "  "
319            <<  NbOfEvents           << "  "
320            <<  absEfftot            << "  "
321            <<  erabsEfftot          << "  "
322            <<  absEff1              << "  "
323            <<  erabsEff1            << "  "
324            <<  absEff2              << "  "
325            <<  erabsEff2            << "  "
```

```
326             <<  absEff                  <<  "   "
327             <<  erabsEff                <<  "   "
328             <<  windowEffSingle         <<  "   "
329             <<  erwindowEffSingle       <<  "   "
330             <<  windowEffDouble         <<  "   "
331             <<  erwindowEffDouble       <<  G4endl;
332 outPutBig2.close();
333
334 std::ofstream outPutBig3("output/effoutput2.dat", iostemp1);
335 outPutBig3 <<   aRun->GetRunID()        <<  "   "
336             <<   Thickness/micrometer   <<  "   "
337             <<  NbOfEvents              <<  "   "
338             <<  efftot                  <<  "   "
339             <<  erefftot                <<  "   "
340             <<  eff1                    <<  "   "
341             <<  ereff1                  <<  "   "
342             <<  eff2                    <<  "   "
343             <<  ereff2                  <<  "   "
344             <<  effBoth                 <<  "   "
345             <<  ereffBoth               <<  "   "
346             <<  weffSingle              <<  "   "
347             <<  erweffSingle            <<  "   "
348             <<  weffDouble              <<  "   "
349             <<  erweffDouble            <<  G4endl;
350 outPutBig3.close();
351
352 //rename list of energy values to include run number in filename
353 char eventsRun1[200];
354 sprintf(eventsRun1,"output/run%d_events1.dat",aRun->GetRunID());
355 G4int result;
356 char oldname[] =  "events1.dat";
357 result= rename( oldname , eventsRun1 );
358 char eventsRun2[200];
359 sprintf(eventsRun2,"output/run%d_events2.dat",aRun->GetRunID());
360 char oldname2[] = "events2.dat";
361 result=rename( oldname2 , eventsRun2 );
362 char eventsRun3[200];
363 sprintf(eventsRun3,"output/run%d_log_file.dat",aRun->GetRunID());
364 char oldname3[] = "LOG FILE.dat";
365 result=rename( oldname3 , eventsRun3 );
366 char eventsRun4[200];
367 sprintf(eventsRun4,"output/run%d_OUTPUT.dat",aRun->GetRunID());
368 char oldname4[] = "OUTPUT.dat";
369 result=rename( oldname4 , eventsRun4 );
370 }
```

C.5 Event action

```
#include "EventAction.hh"
#include "RunAction.hh"
#include "G4TrajectoryContainer.hh"
#include "G4VTrajectory.hh"
#include "G4VVisManager.hh"
#include "G4UnitsTable.hh"
#include "SteppingAction.hh"
#include "G4RunManager.hh"
#include "G4Event.hh"

EventAction::EventAction(RunAction* run)
: runAct(run), fPrintModulo(100){ }

EventAction::~EventAction(){ }

void EventAction::BeginOfEventAction(const G4Event* event)
{
  G4int eventNb = event->GetEventID();
  eventNumber = eventNb;
  if (eventNb%fPrintModulo == 0) { }

  EnergyWorld = 0.0;
  EnergyDet1  = 0.0;
  EnergyDet2  = 0.0;
}

void EventAction::EndOfEventAction(const G4Event* event)
{
G4int eventNb = event->GetEventID();
runAct->fillPerEvent(EnergyDet1,EnergyDet2,eventNb);
if (eventNb == 0) runAct->SaveDetectorParameters(Thickness);
if (eventNb%fPrintModulo == 0) {

G4cout << std::setw(12) << eventNb <<  std::setw(12)  << EnergyWorld
    << std::setw(12)  << EnergyDet1 << std::setw(12)  << EnergyDet2 <<
    G4endl;
}

}
```

C.6 Detector messenger

```
#include "DetectorMessenger.hh"
#include "DetectorConstruction.hh"
#include "G4UIdirectory.hh"
#include "G4UIcmdWithAString.hh"
#include "G4UIcmdWithAnInteger.hh"
#include "G4UIcmdWithADoubleAndUnit.hh"
#include "G4UIcmdWithoutParameter.hh"

DetectorMessenger::DetectorMessenger (DetectorConstruction* Det)
:Detector(Det)
{
  alphaDir = new G4UIdirectory("/alpha/");
  alphaDir->SetGuidance("UI commands of this example");

  detDir = new G4UIdirectory("/alpha/det/");
  detDir->SetGuidance("detector control");
  thicknessCmd = new G4UIcmdWithADoubleAndUnit("/alpha/det/
    setThickness",this);
  thicknessCmd->SetGuidance("Set thickness of reactive film");
  thicknessCmd->SetParameterName("Size",false);
  thicknessCmd->SetRange("Size>0.");
  thicknessCmd->SetUnitCategory("Length");
  thicknessCmd->AvailableForStates(G4State_PreInit,G4State_Idle);
  FilmMaterCmd = new G4UIcmdWithAString("/alpha/det/filmMat",this);
  FilmMaterCmd->SetGuidance("Select 6Li or 6LiF reactive film.");
  FilmMaterCmd->SetParameterName("choice",false);
  FilmMaterCmd->AvailableForStates(G4State_PreInit,G4State_Idle);
  UpdateCmd = new G4UIcmdWithoutParameter("/alpha/det/update",this);
  UpdateCmd->SetGuidance("Update calorimeter geometry.");
  UpdateCmd->SetGuidance("This command MUST be applied before \"
    beamOn\" ");
  UpdateCmd->SetGuidance("if you changed geometrical value(s).");
  UpdateCmd->AvailableForStates(G4State_Idle);
}

DetectorMessenger::~DetectorMessenger()
{
  delete thicknessCmd;   delete UpdateCmd;
  delete detDir;
  delete alphaDir;
  delete FilmMaterCmd;
}

```

```
42 void DetectorMessenger::SetNewValue(G4UIcommand* command,G4String
       newValue)
43 {
44   if( command == thicknessCmd )
45    { Detector->SetThickness(thicknessCmd->GetNewDoubleValue(newValue)
       );}
46
47   if( command == FilmMaterCmd )
48    { Detector->SetFilmMaterial(newValue);}
49
50   if( command == UpdateCmd )
51    { Detector->UpdateGeometry(); }
52 }
```

Appendix D

MCNP codes

D.1 The "Basic" experimental setup

```
The "Basic" experiment layout
C
C material densities
C 1 = H2O (-1), 2 = Air(1e-3), 3 = silicon (-2.329), 4 = LiF (-2.53) 5 = Al (-2.7)
C -ve => g/cm3    +ve => atom/barn-cm
C ########################## Define Cells ##########################
C
1 1 -1 1 -2 3 -4 5 -6              imp:n 1 imp:p 0              $ water tank
2 3 -2.329   -7                    imp:n 1 imp:p 0              $ sensor A
3 4 -2.53    -8                    imp:n 1 imp:p 0              $ LiF film
4 3 -2.329   -9                    imp:n 1 imp:p 0              $ sensor B
5 2 -1e-3 -10 #(-7) #(-8) #(-9)  imp:n 1 imp:p 0              $ air box (detector space)
6 5 -2.7 10 -11                    imp:n 1 imp:p 0              $ Al box
10 0 100                           imp:n 0 imp:p 0              $ outer world
20 2 -1e-3 -100 #(1 -2 3 -4 5 -6) #(-11) imp:n 1 imp:p 0        $ inner world
C
C ########################## Define Surface ##########################
C
1 px 0                                                          $ surfaces define water tank
2 px 60
3 py 0
4 py 70
5 pz 100
6 pz 130
7 RPP 29.5 30.5 39.5 40.5 180 180.03                            $ sensor-1-silicon
8 RPP 29.5 30.5 39.5 40.5 180.03 180.0307                       $ converter LiF film
9 RPP 29.5 30.5 39.5 40.5 180.0607 180.0907                     $ sensor-2-silicon
10 RPP  24 36 35 45 178.75 181.25                               $ air box
11 RPP 23.75 36.25 34.75 45.25 177.95 182.25                    $ Al box include air box
100 RPP 0 70 0 80 100 200                                       $ world of interest
C
C ########################## Define Source ##########################
C Source AM/Be energy definition. Point source. Isotopic.
sdef pos=30 40 105 erg=d1 par=1
mode n
si1 h 0 0.5 1 1.5 2 2.5 3 3.5 4 4.5 5 5.5 6 6.5 7 7.5 8 8.5
    9 9.5 10 10.5 11 11.5 12
sp1 d 0 0.15 0.08 0.09 0.06 0.100 0.15 0.107 0.101 0.11 0.102 0.15
    0.07 0.12 0.05 0.08 0.10 0.05 0.02 0.03 0.04 0.02 0 0 0
print 110
C ########################## Define Tallies ##########################
C
f2:n 7.5                  $ flux across surface LiF
e2   0.5e-6 1e-6 0.5e-5 1e-5 0.5e-4 1e-4 0.5e-3 1e-3
     0.5e-2 1e-2 0.5e-1 1e-1 0.5 1 5 10 50 100
f14:n 3                   $Tally neutrons in cell 3
```

```
e14  0.5e-6 1e-6 0.5e-5 1e-5 0.5e-4 1e-4 0.5e-3 1e-3
     0.5e-2 1e-2 0.5e-1 1e-1 0.5 1 5 10 15 20 50 100
C
C Interaction in detector
C
f24:n 3                  $Tally neutrons in cell 3
e24  0.5e-6 1e-6 0.5e-5 1e-5 0.5e-4 1e-4 0.5e-3 1e-3
     0.5e-2 1e-2 0.5e-1 1e-1 0.5 1 5 10 15 20 50 100
C fm24 -1 4 207          $simulate total alpha production
fm24 -1 4 205            $simulate total tritum production
C
C ######################### Define Materials ############################
C
m1 1001.42C 0.67 8016.60C 0.33                    $ water
m2 8016.60c 0.21 7014.60c 0.79                    $ air
m3 14000.21c 1                                    $ silicon
m4 3006.50c 0.228 3007.60c 0.012 9019.42c 0.76    $ LiF
m5 13027.42c 1                                    $ Aluminum
mt1 lwtr.01t                                      $ thermal treatment water card
C
C ############################ Define run time ##########################
C
nps 1500000000
```

D.2 The "HDPE" experimental setup

```
The "HDPE" experimental layout (Front flux)
C
C material densities
C 1 = H2O (-1), 2 = air (1e-3), 3 = silicon (-2.329), 4 = LiF (-2.53), 5 = Al (-2.7)
C 6 = pb (-11.35), 7 = polyethylene (-0.93)
C -ve => g/cm3    +ve => atom/barn-cm
C ################################ Define Cells ##############################
C
1 1 -1 1 -2 3 -4 5 -6                imp:n 1 imp:p 0      $ water tank
2 3 -2.329    -7                     imp:n 1 imp:p 0      $ sensor A
3 4 -2.53     -8                     imp:n 1 imp:p 0      $ LiF film
4 3 -2.329    -9                     imp:n 1 imp:p 0      $ sensor B
5 2 -1e-3 -10 #(-7) #(-8) #(-9)      imp:n 1 imp:p 0      $ air box
6 5 -2.7 -11  10                     imp:n 1 imp:p 0      $ Al box
7 6 -11.35 -12                       imp:n 1 imp:p 0      $ Lead shield
8 7 -0.93 -13 : -14 : -15 : -16      imp:n 1 imp:p 0      $ polythene
10 0 100                             imp:n 0 imp:p 0      $ outer world
20 2 -1e-3 -100 #(1 -2 3 -4 5 -6) #(-7) #(-8) #(-9) #(-11) #(-12)
     #(-13) #(-14) #(-15) #(-16)     imp:n 1 imp:p 0      $ inner world

C
C ################################ Define Surface ############################
C
1 px 0                                          $ surfaces define water tank
2 px 60
3 py 0
4 py 70
5 pz 104
6 pz 130
7 RPP 29.5 30.5 39.5 40.5 180 180.03            $ silicon sensor A
8 RPP 29.5 30.5 39.5 40.5 180.03 180.0307       $ LiF film
9 RPP 29.5 30.5 39.5 40.5 180.0607 180.0907     $ silicon sensor B
10 RPP 24 36 35 45 178.75 181.25                $ air box
11 RPP 23.75 36.25 34.75 45.25 177.95 182.25    $ AL box
12 RPP 12.5 47.5 34 46 167.5 172.5              $ lead shield from front
13 RPP 10.5 12.5 0 60 167.5 190                 $ polyethylene from right
14 RPP 12.5 47.5 0 60 188 190                   $ polyethylene from behind
15 RPP 47.5 49.5 0 60 167.5 190                 $ polyethylene from left
16 RPP 10.5 49.5 60 62 167.5 190                $ polyethylene from top
C 100 s 30 40 105 150                           $ outer world
100 RPP 0 60 0 70 104 195                       $ World

C
```

```
C ############################### Define Source ############################
C Source AM/Be energy definition. Point source. Isotopic.
sdef pos = 30 40 105 erg = d1 par = 1
mode n
si1 h 0 0.5 1 1.5 2 2.5 3 3.5 4 4.5 5 5.5 6 6.5 7 7.5 8 8.5
     9 9.5 10 10.5 11 11.5 12
sp1 d 0 0.15 0.08 0.09 0.06 0.100 0.15 0.107 0.101 0.11 0.102 0.15
     0.07 0.12 0.05 0.08 0.10 0.05 0.02 0.03 0.04 0.02 0 0 0
C
C ############################### Define Tallies ###########################
C
f14:n 3                      $Tally neutrons in cell 3
C cf14:n 7 8                 $ portion of flux caused by cell 7 and 8
e14  0.5e-6 1e-6 0.5e-5 1e-5 0.5e-4 1e-4 0.5e-3 1e-3
    0.5e-2 1e-2 0.5e-1 1e-1 0.5 1 5 10 50 100
C
C Interaction in detector
C
f24:n 3                      $ Tally neutrons in cell 3
e24  0.5e-6 1e-6 0.5e-5 1e-5 0.5e-4 1e-4 0.5e-3 1e-3
    0.5e-2 1e-2 0.5e-1 1e-1 0.5 1 5 10 50 100
C fm24 -1 4 207              $ simulate total alpha production
fm24 -1 4 205                $ simulate total tritum production
C f2:n 7.5                   $ flux across surface LiF
C e2   0.5e-6 1e-6 0.5e-5 1e-5 0.5e-4 1e-4 0.5e-3 1e-3
C       0.5e-2 1e-2 0.5e-1 1e-1 0.5 1 5 10 50 100
C
C ############################### Define Materials #########################
C
m1 1001.35C 0.67 8016.60C 0.33                $ water
m2 8016.60c 0.21 7014.60c 0.79                $ air
m3 14000.21c 1                                $ silicon
m4 3006.50c 0.228 3007.60c 0.012 9019.42c 0.76  $ LiF
m5 13027.42c 1                                $ Aluminum
m6 82000.42c 1                                $ Natural Lead
m7 6000.60c 0.333338 1001.35c 0.666662        $ polyethelene
mt1 lwtr.01t                                  $ thermal treatment water card
mt7 poly.01t                                  $ thermal treatment polyethene card
C
C ############################### Define run time ##########################
C
nps 1500000000
```

D.3 Right neutron flux

```
The “HDPE” experimental layout (Right flux)
C
C material densities
C 1 = H2O (-1), 2 = air (1e-3), 3 = silicon (-2.329), 4 = LiF (-2.53), 5 = Al (-2.7)
C 6 = pb (-11.35), 7 = polyethylene (-0.93)
C -ve => g/cm3    +ve => atom/barn-cm
C ############################### Define Cells ############################
C
1 1 -1 -1                                   imp:n 1      $ water tank
2 3 -2.329    -7                            imp:n 1      $ silicon-1
3 4 -2.53     -8                            imp:n 1      $ LiF-7um
4 3 -2.329    -9                            imp:n 1      $ silicon-2
5 2 -1e-3 -10 #(-7) #(-8) #(-9)             imp:n 1      $ air box
6 5 -2.7 -11  10                            imp:n 1      $ Al box
7 6 -11.35 -12                              imp:n 1      $ Lead shield front
8 7 -0.93 -13 : -14 : -15 : -16             imp:n 1      $ polyethene all surfaces
10 0 100                    imp:n 0                      $ outer world
20 2 -1e-3 -100 #(-1) #(-7) #(-8) #(-9) #(-11) #(-12)
     #(-13) #(-14) #(-15) #(-16)            imp:n 1      $ inner world

C
C ############################### Define Surface ############################
C
1 RPP -45 -20 0 70 150.03 210.03            $ surfaces define water tank
7 RPP 29.5 30.5 39.5 40.5 180 180.03        $ detector-1-silicon
8 RPP 29.5 30.5 39.5 40.5 180.06 180.0607   $ detector-2-LiF 7um
9 RPP 29.5 30.5 39.5 40.5 180.0607 180.0907 $ detector-3-silicon
10 RPP 24 36 35 45 178.75 181.25            $ air box
11 RPP 23.75 36.25 34.75 45.25 177.95 182.25 $ aluminum box
12 RPP 12.5 47.5 34 46 167.5 172.5          $ lead shield from front L1
13 RPP 10.5 12.5 0 60 167.5 190             $ polyethylene from right P1
14 RPP 12.5 47.5 0 60 188 190               $ polyethylene from behind P2
15 RPP 47.5 49.5 0 60 167.5 190             $ polyethylene from left P3
16 RPP 10.5 49.5 60 62 167.5 190            $ polyethylene from top P4
100 RPP -46 50 0 70 150 212.06              $ World

C
C ############################### Define Source ############################
C Source AM/Be energy definition. Point source. Isotopic.
sdef pos= -44 40 180.03 erg = d1 par = 1
mode n
si1 h 0 0.5 1 1.5 2 2.5 3 3.5 4 4.5 5 5.5 6 6.5 7 7.5 8 8.5
```

```
     9 9.5 10 10.5 11 11.5 12
sp1 d 0 0.15 0.08 0.09 0.06 0.100 0.15 0.107 0.101 0.11 0.102 0.15
     0.07 0.12 0.05 0.08 0.10 0.05 0.02 0.03 0.04 0.02 0 0 0
C
C ################################ Define Tallies ##########################
C
f14:n 3                          $ Tally neutrons in cell 3
cf14:n 7 8                       $ portion of flux caused by cell 7 and 8
e14  0.5e-6 1e-6 0.5e-5 1e-5 0.5e-4 1e-4 0.5e-3 1e-3
    0.5e-2 1e-2 0.5e-1 1e-1 0.5 1 5 10 50 100
C Interaction in detector
C
C f24:n 3                        $ Tally neotrons in cell 3
C e24  0.5e-6 1e-6 0.5e-5 1e-5 0.5e-4 1e-4 0.5e-3 1e-3
C     0.5e-2 1e-2 0.5e-1 1e-1 0.5 1 5 10 50 100
C fm24 -1 4 207                  $ simulate total alpha production
C fm24 -1 4 205                  $ simulate total tritum production
C
C ################################ Define Materials ########################
C
m1 1001.35C 0.67 8016.60C 0.33                  $ water
m2 8016.60c 0.21 7014.60c 0.79                  $ air
m3 14000.21c 1                                  $ silicon
m4 3006.50c 0.228 3007.60c 0.012 9019.42c 0.76  $ LiF
m5 13027.42c 1                                  $ Aluminum
m6 82000.42c 1                                  $ Natural Lead
m7 6000.60c 0.333338 1001.35c 0.666662          $ polyethylene
mt1 lwtr.01t                                    $ thermal treatment water card
mt7 poly.01t                                    $ thermal treatment polyethene card
C
C ################################ Define run time ##########################
C
nps 1500000000
```

D.4 Back neutron flux

```
The "HDPE" experimental layout (Back flux)
C
C material densities
C 1 = H2O (-1), 2 = air (1e-3), 3 = silicon (-2.329), 4 = LiF (-2.53), 5 = Al (-2.7)
C 6 = pb (-11.35), 7 = polyethylene (-0.93)
C -ve => g/cm3    +ve => atom/barn-cm
C ############################### Define Cells ############################
C
1 1 -1 -1                                   imp:n 1      $ water tank
2 3 -2.329    -7                            imp:n 1      $ silicon-1
3 4 -2.53     -8                            imp:n 1      $ LiF-7um
4 3 -2.329    -9                            imp:n 1      $ silicon-2
5 2 -1e-3 -10 #(-7) #(-8) #(-9)             imp:n 1      $ air box
6 5 -2.7 -11  10                            imp:n 1      $ Al box
7 6 -11.35 -12                              imp:n 1      $ Lead shield front
8 7 -0.93 -13 : -14 : -15 : -16             imp:n 1      $ polyethene all surfaces
10 0 100                    imp:n 0                      $ outer world
20 2 -1e-3 -100 #(-1) #(-7) #(-8) #(-9) #(-11) #(-12)
     #(-13) #(-14) #(-15) #(-16)            imp:n 1      $ inner world

C
C ############################### Define Surface ##########################
C
1 RPP -45 -20 0 70 150.03 210.03                $ surfaces define water tank
7 RPP 29.5 30.5 39.5 40.5 180 180.03            $ detector-1-silicon
8 RPP 29.5 30.5 39.5 40.5 180.06 180.0607       $ detector-2-LiF 7um
9 RPP 29.5 30.5 39.5 40.5 180.0607 180.0907     $ detector-3-silicon
10 RPP 24 36 35 45 178.75 181.25                $ air box
11 RPP 23.75 36.25 34.75 45.25 177.95 182.25    $ aluminum box
12 RPP 12.5 47.5 34 46 185 190                  $ lead shield from front L1
13 RPP 10.5 12.5 0 60 167.5 190                 $ polyethylene from right P1
14 RPP 12.5 47.5 0 60 167.5 169.5               $ polyethylene from behind P2
15 RPP 47.5 49.5 0 60 167.5 190                 $ polyethylene from left P3
16 RPP 10.5 49.5 60 62 167.5 190                $ polyethylene from top P4
100 RPP -46 50 0 70 150 212.06                  $ World

C
C ############################### Define Source ###########################
C Source AM/Be energy definition. Point source. Isotopic.
sdef pos=30 40 105 erg = d1 par = 1
mode n
si1 h 0 0.5 1 1.5 2 2.5 3 3.5 4 4.5 5 5.5 6 6.5 7 7.5 8 8.5
     9 9.5 10 10.5 11 11.5 12
```

```
sp1 d 0 0.15 0.08 0.09 0.06 0.100 0.15 0.107 0.101 0.11 0.102 0.15
    0.07 0.12 0.05 0.08 0.10 0.05 0.02 0.03 0.04 0.02 0 0 0
C
C ############################### Define Tallies ##########################
C
f14:n 3                          $ Tally neutrons in cell 3
cf14:n 7 8                       $ portion of flux caused by cell 7 and 8
e14  0.5e-6 1e-6 0.5e-5 1e-5 0.5e-4 1e-4 0.5e-3 1e-3
   0.5e-2 1e-2 0.5e-1 1e-1 0.5 1 5 10 50 100
C Interaction in detector
C
C f24:n 3                        $ Tally neotrons in cell 3
C e24  0.5e-6 1e-6 0.5e-5 1e-5 0.5e-4 1e-4 0.5e-3 1e-3
C    0.5e-2 1e-2 0.5e-1 1e-1 0.5 1 5 10 50 100
C fm24 -1 4 207                  $ simulate total alpha production
C fm24 -1 4 205                  $ simulate total tritum production
C
C ############################### Define Materials ########################
C
m1 1001.35C 0.67 8016.60C 0.33                $ water
m2 8016.60c 0.21 7014.60c 0.79                $ air
m3 14000.21c 1                                $ silicon
m4 3006.50c 0.228 3007.60c 0.012 9019.42c 0.76  $ LiF
m5 13027.42c 1                                $ Aluminum
m6 82000.42c 1                                $ Natural Lead
m7 6000.60c 0.333338 1001.35c 0.666662        $ polyethylene
mt1 lwtr.01t                                  $ thermal treatment water card
mt7 poly.01t                                  $ thermal treatment polyethene card
C
C ############################### Define run time #########################
C
nps 1500000000
```

D.5 Left neutron flux

```
The “HDPE” experimental layout (Left flux)
C
C material densities
C 1 = H2O (-1), 2 = air (1e-3), 3 = silicon (-2.329), 4 = LiF (-2.53), 5 = Al (-2.7)
C 6 = pb (-11.35), 7 = polyethylene (-0.93)
C -ve => g/cm3    +ve => atom/barn-cm
C ################################ Define Cells ############################
C
1 1 -1 -1                                   imp:n 1      $ water tank
2 3 -2.329    -7                            imp:n 1      $ silicon-1
3 4 -2.53     -8                            imp:n 1      $ LiF-7um
4 3 -2.329    -9                            imp:n 1      $ silicon-2
5 2 -1e-3 -10 #(-7) #(-8) #(-9)             imp:n 1      $ air box
6 5 -2.7 -11  10                            imp:n 1      $ Al box
7 6 -11.35 -12                              imp:n 1      $ Lead shield front
8 7 -0.93 -13 : -14 : -15 : -16             imp:n 1      $ polyethene all surfaces
10 0 100                    imp:n 0                      $ outer world
20 2 -1e-3 -100 #(-1) #(-7) #(-8) #(-9) #(-11) #(-12)
     #(-13) #(-14) #(-15) #(-16)            imp:n 1      $ inner world

C
C ################################ Define Surface ##########################
C
1 RPP -45 -20 0 70 150.03 210.03                $ surfaces define water tank
7 RPP 29.5 30.5 39.5 40.5 180 180.03            $ detector-1-silicon
8 RPP 29.5 30.5 39.5 40.5 180.06 180.0607       $ detector-2-LiF 7um
9 RPP 29.5 30.5 39.5 40.5 180.0607 180.0907     $ detector-3-silicon
10 RPP 24 36 35 45 178.75 181.25                $ air box
11 RPP 23.75 36.25 34.75 45.25 177.95 182.25    $ aluminum box
12 RPP 12.5 47.5 34 46 185 190                  $ lead shield from front L1
13 RPP 10.5 12.5 0 60 167.5 190                 $ polyethylene from right P1
14 RPP 12.5 47.5 0 60 167.5 169.5               $ polyethylene from behind P2
15 RPP 47.5 49.5 0 60 167.5 190                 $ polyethylene from left P3
16 RPP 10.5 49.5 60 62 167.5 190                $ polyethylene from top P4
100 RPP -46 50 0 70 150 212.06                  $ World

C
C ################################ Define Source ##########################
C Source AM/Be energy definition. Point source. Isotopic.
sdef pos= -44 40 180.03 erg = d1 par = 1
mode n
si1 h 0 0.5 1 1.5 2 2.5 3 3.5 4 4.5 5 5.5 6 6.5 7 7.5 8 8.5
     9 9.5 10 10.5 11 11.5 12
```

```
sp1 d 0 0.15 0.08 0.09 0.06 0.100 0.15 0.107 0.101 0.11 0.102 0.15
    0.07 0.12 0.05 0.08 0.10 0.05 0.02 0.03 0.04 0.02 0 0 0
C
C ############################### Define Tallies ##########################
C
f14:n 3                          $ Tally neutrons in cell 3
cf14:n 7 8                       $ portion of flux caused by cell 7 and 8
e14  0.5e-6 1e-6 0.5e-5 1e-5 0.5e-4 1e-4 0.5e-3 1e-3
   0.5e-2 1e-2 0.5e-1 1e-1 0.5 1 5 10 50 100
C Interaction in detector
C
C f24:n 3                        $ Tally neotrons in cell 3
C e24  0.5e-6 1e-6 0.5e-5 1e-5 0.5e-4 1e-4 0.5e-3 1e-3
C    0.5e-2 1e-2 0.5e-1 1e-1 0.5 1 5 10 50 100
C fm24 -1 4 207                  $ simulate total alpha production
C fm24 -1 4 205                  $ simulate total tritum production
C
C ############################### Define Materials ########################
C
m1 1001.35C 0.67 8016.60C 0.33                  $ water
m2 8016.60c 0.21 7014.60c 0.79                  $ air
m3 14000.21c 1                                  $ silicon
m4 3006.50c 0.228 3007.60c 0.012 9019.42c 0.76  $ LiF
m5 13027.42c 1                                  $ Aluminum
m6 82000.42c 1                                  $ Natural Lead
m7 6000.60c 0.333338 1001.35c 0.666662          $ polyethylene
mt1 lwtr.01t                                    $ thermal treatment water card
mt7 poly.01t                                    $ thermal treatment polyethene card
C
C ############################### Define run time #########################
C
nps 1500000000
```

D.6 Handheld detector configuration

```
Handheld detector configuration
C
C material densities
C 1 = H2O (-1), 2 = air (1e-3), 3 = silicon (-2.329), 4 = LiF (-2.53), 5 = Al (-2.7)
C 6 = pb (-11.35), 7 = polyethylene (-0.93)
C -ve => g/cm3    +ve => atom/barn-cm
C ############################### Define Cells ############################
C
1 1 -1 1 -2 3 -4 5 -6                                  imp:n 1 imp:p 0     $ water tank
2 3 -2.329    -7                                       imp:n 1 imp:p 0     $ silicon-1
3 4 -2.53     -8                                       imp:n 1 imp:p 0     $ LiF-12um
4 3 -2.329    -9                                       imp:n 1 imp:p 0     $ silicon-2
20 3 -2.329   -70                                      imp:n 1 imp:p 0     $ silicon-3
30 4 -2.53    -80                                      imp:n 1 imp:p 0     $ LiF-11um
40 3 -2.329   -90                                      imp:n 1 imp:p 0     $ silicon-4
5 2 -1e-3 -10 #(-7) #(-8) #(-9)
        #(-70) #(-80) #(-90)                           imp:n 1 imp:p 0     $ air box
6 5 -2.7 -11  10                                       imp:n 1 imp:p 0     $ Al box
7 6 -11.35 -12                                         imp:n 1 imp:p 0     $ Lead shield
8 7 -0.93 -13 : -14 : -15 : -16 : -17                  imp:n 1 imp:p 0     $ polythen
10 0 100                                               imp:n 0 imp:p 0     $ outer world
100 2 -1e-3 -100 #(1 -2 3 -4 5 -6) #(-7) #(-8) #(-9) #(-11) #(-12)
     #(-13) #(-14) #(-15) #(-16) #(-17)                imp:n 1 imp:p 0     $ inner world

C
C ############################### Define Surface ##########################
C
1 px 0                                                 $ surfaces define water tank
2 px 60
3 py 0
4 py 70
5 pz 104
6 pz 130
7 RPP 29.5 30.5 39.5 40.5 180 180.03                   $ sensor-1-silicon
8 RPP 29.5 30.5 39.5 40.5 180.03 180.0312              $ converter-1-LiF
9 RPP 29.5 30.5 39.5 40.5 180.0607 180.0907            $ sensor-2-silicon
70 RPP 29.5 30.5 39.5 40.5 179.5 179.53                $ sensor-3-silicon
80 RPP 29.5 30.5 39.5 40.5 179.53 179.5311             $ converter -2-LiF
90 RPP 29.5 30.5 39.5 40.5 179.57 179.6                $ sensor-4-silicon
10 RPP 25 35 35 45 178.2 182                           $ air box
11 RPP 24.75 35.25 34.75 45.25 177.95 182.25           $ aluminium box include air box
12 RPP 24.75 35.25 34.75 45.25 177.7 177.95            $ lead shield from front L1
13 RPP 22.75 24.75 34.75 45.25 177.7 182.25            $ polyethlene from right P1
14 RPP 22.75 37.25 34.75 45.25 182.25 184.25           $ polyethelene from behind P2
15 RPP 35.25 37.25 34.75 45.25 177.7 182.25            $ polyethylene from left P3
16 RPP 22.75 37.25 45.25 47.25 177.7 184.25            $ polyethylene from top P4
```

```
17 RPP 22.75 37.25 32.75 34.75 177.7 184.25      $ polyethylene from bottum P5
C 100 s 30 40 105 150                            $ outer world
100 RPP 0 60 0 70 104 195                        $ World

C
C ################################ Define Source ############################
C Source AM/Be energy definition. Point source. Isotopic.
sdef pos = 30 40 105 erg = d1 par = 1
mode n
si1 h 0 0.5 1 1.5 2 2.5 3 3.5 4 4.5 5 5.5 6 6.5 7 7.5 8 8.5
     9 9.5 10 10.5 11 11.5 12
sp1 d 0 0.15 0.08 0.09 0.06 0.100 0.15 0.107 0.101 0.11 0.102 0.15
     0.07 0.12 0.05 0.08 0.10 0.05 0.02 0.03 0.04 0.02 0 0 0
C
C ################################ Define Tallies ############################
C
C
f14:n 30 3 (30 3) T              $Tally neutrons in cell 3 30
e14  0.5e-6 1e-6 0.5e-5 1e-5 0.5e-4 1e-4 0.5e-3 1e-3
    0.5e-2 1e-2 0.5e-1 1e-1 0.5 1 5 10 50 100
C
C Interaction in detector
C
f24:n 30 3 (30 3) T              $Tally neotrons in cell 3 30
e24  0.5e-6 1e-6 0.5e-5 1e-5 0.5e-4 1e-4 0.5e-3 1e-3
    0.5e-2 1e-2 0.5e-1 1e-1 0.5 1 5 10 50 100
fm24 -1 4 207                    $simulate total alpha production
C fm24 -1 4 205                  $simulate total tritum production
C
C ############################## Define Materials ############################
C
m1 1001.35C 0.67 8016.60C 0.33                    $ water
m2 8016.60c 0.21 7014.60c 0.79                    $ air
m3 14000.21c 1                                    $ silicon
m4 3006.50c 0.228 3007.60c 0.012 9019.42c 0.76 $ LiF
m5 13027.42c 1                                    $ Aluminium
m6 82000.42c 1                                    $ Natural Lead
m7 6000.60c 0.333338 1001.35c 0.666662            $ polyethylene
mt1 lwtr.01t                                      $ thermal treatment water card
mt7 poly.01t                                      $ thermal treatment polyethylene card
C
C ############################## Define run time ############################
C
nps 1500000000
```

Bibliography

[1] Maria Kelley. *Terrorism and the growing threat of weapons of mass destruction: Al-Shabaab*. Anchor Academic Publishing (aap_verlag), 2014.

[2] Steve Fetter et al. "Detecting nuclear warheads". In: *Science & Global Security* 1.3-4 (1990), pp. 225–253.

[3] Kelly A Jordan and Tsahi Gozani. "Detection of 235 U in hydrogenous cargo with differential die-away analysis and optimized neutron detectors". In: *Nuclear Instruments and Methods in Physics Research Section A: Accelerators, Spectrometers, Detectors and Associated Equipment* 579.1 (2007), pp. 388–390.

[4] Ervin B Podgoršak. *Radiation physics for medical physicists*. Springer, 2006.

[5] Glenn F Knoll. *Radiation detection and measurement*. John Wiley & Sons, 2010.

[6] Gerhard Lutz et al. *Semiconductor radiation detectors*. Vol. 10. Springer, 1999.

[7] Bernard F Phlips et al. "Neutron detection using large area silicon detectors". In: *Nuclear Instruments and Methods in Physics Research Section A: Accelerators, Spectrometers, Detectors and Associated Equipment* 579.1 (2007), pp. 173–176.

[8] Consuelo Guardiola et al. "Ultra-thin 3D silicon sensors for neutron detection". In: *Journal of Instrumentation* 7.03 (2012), P03006.

[9] James Chadwick. "The existence of a neutron". In: *Proceedings of the Royal Society of London. Series A* 136.830 (1932), pp. 692–708.

[10] Claude Leroy. "Radiation interaction in matter and principles of detection". In: *AIP Conference Proceedings*. Vol. 958. 1. AIP. 2007, pp. 85–91.

[11] MA Gomaa, BA Henaish, and EM Ali. "Calculated neutron and gamma dose rates around a moderated Am-Be neutron source". In: *Applied Radiation and Isotopes* 44.3 (1993), pp. 638–640.

[12] II Auxier and John David. "The Development of Lithium Tetraborate Compounds for Thermal Neutron Detection". In: (2013).

[13] Claude Leroy and Pier-Giorgio Rancoita. *Principles of radiation interaction in matter and detection*. Vol. 2. World Scientific, 2009.

[14] David W Anderson. *Absorption of ionizing radiation*. University Park Press, 1984.

[15] Y Hosono, T Iguchi, M Nakazawa, et al. "Fast neutron detector using PIN-type silicon photodiode". In: *Nuclear Instruments and Methods in Physics Research Section A: Accelerators, Spectrometers, Detectors and Associated Equipment* 361.3 (1995), pp. 554–557.

[16] PL Reeder et al. "Detection of fast neutrons in a plastic scintillator using digital pulse processing to reject gammas". In: *Nuclear Instruments and Methods in Physics Research Section A: Accelerators, Spectrometers, Detectors and Associated Equipment* 422.1 (1999), pp. 84–88.

[17] Frank H Ruddy et al. "The fast neutron response of 4H silicon carbide semiconductor radiation detectors". In: *IEEE transactions on nuclear science* 53.3 (2006), pp. 1666–1670.

[18] Robert W Flammang, John G Seidel, and Frank H Ruddy. "Fast neutron detection with silicon carbide semiconductor radiation detectors". In: *Nuclear Instruments and Methods in Physics Research Section A: Accelerators, Spectrometers, Detectors and Associated Equipment* 579.1 (2007), pp. 177–179.

[19] J Uher et al. "Detection of fast neutrons with the Medipix-2 pixel detector". In: *Nuclear Instruments and Methods in Physics Research Section A: Accelerators, Spectrometers, Detectors and Associated Equipment* 591.1 (2008), pp. 71–74.

[20] GC Rich et al. "Fabrication and characterization of a lithium-glass-based composite neutron detector". In: *Nuclear Instruments and Methods in Physics Research Section A: Accelerators, Spectrometers, Detectors and Associated Equipment* 794 (2015), pp. 15–24.

[21] M Mayer et al. "Development and characterization of a neutron detector based on a lithium glass–polymer composite". In: *Nuclear Instruments and Methods in Physics Research Section A: Accelerators, Spectrometers, Detectors and Associated Equipment* 785 (2015), pp. 117–122.

[22] TW Crane and MP Baker. "Neutron detectors". In: *Passive Nondestructive Assay of Nuclear Materials* (1991), pp. 379–406.

[23] Stefaan Tavernier. *Experimental techniques in nuclear and particle physics*. Springer Science & Business Media, 2010.

[24] A Oed. "Detectors for thermal neutrons". In: *Nuclear Instruments and Methods in Physics Research Section A: Accelerators, Spectrometers, Detectors and Associated Equipment* 525.1 (2004), pp. 62–68.

[25] Richard Kouzes and Edward Siciliano. "Alternative neutron detection technology for homeland security". In: *APS Meeting Abstracts*. Vol. 1. 2009.

[26] Richard T Kouzes et al. *Alternative neutron detection testing summary*. Tech. rep. Pacific Northwest National Laboratory (PNNL), Richland, WA (US), 2010.

[27] Richard T Kouzes et al. "Neutron detection alternatives to 3He for national security applications". In: *Nuclear Instruments and Methods in Physics Research Section A: Accelerators, Spectrometers, Detectors and Associated Equipment* 623.3 (2010), pp. 1035–1045.

[28] Richard T Kouzes. *The 3He supply problem*. Tech. rep. Pacific Northwest National Laboratory (PNNL), Richland, WA (US), 2009.

[29] A Kreyssig, K Irmer, and U Hartung. "ZnS/6 Li scintillation material as an alternative to 6 Li-glass scintillators for neutron detection in time focusing geometry". In: *Nuclear Instruments and Methods in Physics Research Section A: Accelerators, Spectrometers, Detectors and Associated Equipment* 349.1 (1994), pp. 292–294.

[30] Anthony J Peurrung. "Recent developments in neutron detection". In: *Nuclear Instruments and Methods in Physics Research Section A: Accelerators, Spectrometers, Detectors and Associated Equipment* 443.2 (2000), pp. 400–415.

[31] CL Wang et al. "ZnS quantum dot based nanocomposite scintillators for thermal neutron detection". In: *Nuclear Instruments and Methods in Physics Research Section A: Accelerators, Spectrometers, Detectors and Associated Equipment* 622.1 (2010), pp. 186–190.

[32] J Li et al. "Hexagonal boron nitride epitaxial layers as neutron detector materials". In: *Nuclear Instruments and Methods in Physics Research Section A: Accelerators, Spectrometers, Detectors and Associated Equipment* 654.1 (2011), pp. 417–420.

[33] VA Nikolaev. "Solid-state track detectors in radiometry, isotope analysis, and radiography". In: *Radiochemistry* 54.1 (2012), pp. 1–17.

[34] Brian D Milbrath et al. "Radiation detector materials: An overview". In: *Journal of Materials Research* 23.10 (2008), pp. 2561–2581.

[35] WIKIPEDIA. *Scintillation counter*. URL: https://en.wikipedia.org/wiki/Scintillation_counter (visited on 03/12/2018).

[36] William R Leo. *Techniques for nuclear and particle physics experiments: a how-to approach*. Springer Science & Business Media, 2012.

[37] Anthony N Caruso. "The physics of solid-state neutron detector materials and geometries". In: *Journal of Physics: Condensed Matter* 22.44 (2010), p. 443201.

[38] David Emin and TL Aselage. "A proposed boron-carbide-based solid-state neutron detector". In: *Journal of applied physics* 97.1 (2005), p. 013529.

[39] Kevin Osberg et al. "A handheld neutron-detection sensor system utilizing a new class of boron carbide diode". In: *IEEE Sensors Journal* 6.6 (2006), pp. 1531–1538.

[40] AD Harken and Brian W Robertson. "Comparative modelling of performance limits of solid-state neutron detectors based on planar B-rich capture layers". In: *Journal of Physics D: Applied Physics* 39.23 (2006), p. 4961.

[41] C Lundstedt et al. "Modeling solid-state boron carbide low energy neutron detectors". In: *Nuclear Instruments and Methods in Physics Research Section A: Accelerators, Spectrometers, Detectors and Associated Equipment* 562.1 (2006), pp. 380–388.

[42] Troy C Unruh et al. "Design and operation of a 2-D thin-film semiconductor neutron detector array for use as a beamport monitor". In: *Nuclear Instruments and Methods in Physics Research Section A: Accelerators, Spectrometers, Detectors and Associated Equipment* 604.1 (2009), pp. 150–153.

[43] Douglas S McGregor and J Kenneth Shultis. "Reporting detection efficiency for semiconductor neutron detectors: A need for a standard". In: *Nuclear Instruments and Methods in Physics Research Section A: Accelerators, Spectrometers, Detectors and Associated Equipment* 632.1 (2011), pp. 167–174.

[44] Douglas S McGregor et al. "Thin-film-coated detectors for neutron detection". In: *Journal of the Korean Association for Radiation Protection* 26 (2001), pp. 167–175.

[45] John W Murphy et al. "Optimizing diode thickness for thin-film solid state thermal neutron detectors". In: *Applied Physics Letters* 101.14 (2012), p. 143506.

[46] V Dangendorf et al. "Thermal neutron imaging detectors combining novel composite foil convertors and gaseous electron multipiers". In: *Nuclear Instruments and Methods in Physics Research Section A: Accelerators, Spectrometers, Detectors and Associated Equipment* 350.3 (1994), pp. 503–510.

[47] CA Baker et al. "Development of solid-state silicon devices as ultra cold neutron detectors". In: *Nuclear Instruments and Methods in Physics Research Section A: Accelerators, Spectrometers, Detectors and Associated Equipment* 487.3 (2002), pp. 511–520.

[48] M Voytchev et al. "Neutron detection with a silicon PIN photodiode and 6 LiF converter". In: *Nuclear Instruments and Methods in Physics Research Section A: Accelerators, Spectrometers, Detectors and Associated Equipment* 512.3 (2003), pp. 546–552.

[49] Gabriel M Veith and Nancy J Dudney. "Preparation of thin-film neutron converter foils for imaging detectors". In: *IEEE Transactions on Nuclear Science* 51.3 (2004), pp. 1034–1038.

[50] Mark J Selwood and Stephen David Monk. "Development of a portable isotropic neutron spectrometer". In: *Applied Radiation and Isotopes* 70.7 (2012), pp. 1145–1149.

[51] Sanjoy Mukhopadhyay et al. "Review of current neutron detection systems for emergency response". In: *SPIE Optical Engineering+ Applications*. International Society for Optics and Photonics. 2014, 92130T–92130T.

[52] R Mendicino et al. "Semiconductor neutron detectors". In: *Proceedings of the 24th International Workshop on Vertex Detectors (VERTEX2015). 1-5 June 2015. Santa Fe, New Mexico, USA. http://pos. sissa. it/cgi-bin/reader/conf. cgi? confid= 254, id. 27.* 2015.

[53] Alan Munter. "NIST Center for Neutron Research". In: *Neutron News* 3 (1992), pp. 29–37.

[54] AA Harms and G McCormack. "Isotopic conversion in gadolinium-exposure neutron imaging". In: *Nuclear Instruments and Methods* 118.2 (1974), pp. 583–587.

[55] Alan Paul Jeavons et al. "A new position-sensitive detector for thermal and epithermal neutrons". In: *Nuclear Instruments and Methods* 148.1 (1978), pp. 29–33.

[56] Takahiko Aoyama et al. "A neutron detector using silicon PIN photodiodes for personal neutron dosimetry". In: *Nuclear Instruments and Methods in Physics Research Section A: Accelerators, Spectrometers, Detectors and Associated Equipment* 314.3 (1992), pp. 590–594.

[57] A Mireshghi et al. "Amorphous silicon position sensitive neutron detector". In: *IEEE transactions on nuclear science* 39.4 (1992), pp. 635–640.

[58] D Sueva et al. "Silicon detectors for neutron detection in the presence of high γ-background". In: *Applied Physics A* 71.2 (2000), pp. 211–214.

[59] H Kitaguchi et al. "Silicon semiconductor detectors for various nuclear radiations". In: *IEEE Transactions on Nuclear Science* 43.3 (1996), pp. 1846–1850.

[60] Douglas S McGregor and J Kenneth Shultis. "Spectral identification of thin-film-coated and solid-form semiconductor neutron detectors". In: *Nuclear Instruments and Methods in Physics Research Section A: Accelerators, Spectrometers, Detectors and Associated Equipment* 517.1 (2004), pp. 180–188.

[61] Massimo Barbagallo et al. "Thermal neutron detection using a silicon pad detector and 6LiF removable converters". In: *Review of Scientific Instruments* 84.3 (2013), p. 033503.

[62] A Pappalardo et al. "Characterization of the silicon + ^{6}LiF thermal neutron detection technique". In: *Nuclear Instruments and Methods in Physics Research Section A: Accelerators, Spectrometers, Detectors and Associated Equipment* 810 (2016), pp. 6–13.

[63] Kiril D Ianakiev et al. "6 Li foil scintillation sandwich thermal neutron detector". In: *Nuclear Instruments and Methods in Physics Research Section A: Accelerators, Spectrometers, Detectors and Associated Equipment* 652.1 (2011), pp. 417–420.

[64] Kyle A Nelson et al. “Investigation of a lithium foil multi-wire proportional counter for potential 3 He replacement”. In: *Nuclear Instruments and Methods in Physics Research Section A: Accelerators, Spectrometers, Detectors and Associated Equipment* 669 (2012), pp. 79–84.

[65] Douglas S McGregor et al. “Thin-film-coated bulk GaAs detectors for thermal and fast neutron measurements”. In: *Nuclear Instruments and Methods in Physics Research Section A: Accelerators, Spectrometers, Detectors and Associated Equipment* 466.1 (2001), pp. 126–141.

[66] R Engels et al. “Thermal neutron detection with lithium-6 converters”. In: 1 (2007), pp. 593–596.

[67] Bernd Ross. *Neutron detecting solid state device or the like*. US Patent 3,227,876. Jan. 1966.

[68] H Rauch, F Grass, and B Feigl. “Ein neuartiger detektor für langsame neutronen”. In: *Nuclear instruments and methods* 46.1 (1967), pp. 153–156.

[69] B Feigl and H Rauch. “Der Gd-Neutronenzähler”. In: *Nuclear Instruments and Methods* 61.3 (1968), pp. 349–356.

[70] H Bluhm and D Stegemann. “Theoretical and experimental investigations for an improved application of the 6 Li-semiconductor sandwich spectrometer”. In: *Nuclear Instruments and Methods* 70.2 (1969), pp. 141–150.

[71] Stanislav Pospisil et al. “Si diode as a small detector of slow neutrons”. In: *Radiation Protection Dosimetry* 46.2 (1993), pp. 115–118.

[72] C Petrillo et al. “Solid state neutron detectors”. In: *Nuclear Instruments and Methods in Physics Research Section A: Accelerators, Spectrometers, Detectors and Associated Equipment* 378.3 (1996), pp. 541–551.

[73] Stanislav Pospisil and Carlos Granja. “Neutrons and their Detection with Silicon Diodes”. In: *AIP Conference Proceedings*. Vol. 1204. 1. AIP. 2010, pp. 12–16.

[74] J Schelten et al. “A new neutron detector development based on silicon semiconductor and 6 LiF converter”. In: *Physica B: Condensed Matter* 234 (1997), pp. 1084–1086.

[75] Douglas S McGregor et al. “Designs for thin-film-coated semiconductor thermal neutron detectors”. In: *Nuclear Science Symposium Conference Record (2001 IEEE)*. Vol. 4. 2001, pp. 2454–2458.

[76] Zhehui Wang and Christopher L Morris. "Multi-layer boron thin-film detectors for neutrons". In: *Nuclear Instruments and Methods in Physics Research Section A: Accelerators, Spectrometers, Detectors and Associated Equipment* 652.1 (2011), pp. 323–325.

[77] Douglas S McGregor et al. "Design considerations for thin film coated semiconductor thermal neutron detectors—I: basics regarding alpha particle emitting neutron reactive films". In: *Nuclear Instruments and Methods in Physics Research Section A: Accelerators, Spectrometers, Detectors and Associated Equipment* 500.1 (2003), pp. 272–308.

[78] Doug Reilly et al. *Passive nondestructive assay of nuclear materials*. Tech. rep. Nuclear Regulatory Commission, Washington, DC (United States). Office of Nuclear Regulatory Research; Los Alamos National Lab., NM (United States), 1991.

[79] M Campbell et al. "A readout chip for a 64/spl times/64 pixel matrix with 15-bit single photon counting". In: *IEEE Transactions on Nuclear Science* 45.3 (1998), pp. 751–753.

[80] X Llopart et al. "Medipix2, a 64k pixel read out chip with 55/spl mu/m square elements working in single photon counting mode". In: *Nuclear Science Symposium Conference Record, 2001 IEEE*. Vol. 3. IEEE. 2001, pp. 1484–1488.

[81] J Jakubek et al. "Spatial resolution of Medipix-2 device as neutron pixel detector". In: *Nuclear Instruments and Methods in Physics Research Section A: Accelerators, Spectrometers, Detectors and Associated Equipment* 546.1 (2005), pp. 164–169.

[82] J Uher et al. "Performance of a pixel detector suited for slow neutrons". In: *Nuclear Instruments and Methods in Physics Research Section A: Accelerators, Spectrometers, Detectors and Associated Equipment* 542.1 (2005), pp. 283–287.

[83] Jan Jakbek et al. "Properties of the single neutron pixel detector based on the Medipix-1 device". In: *Nuclear Instruments and Methods in Physics Research Section A: Accelerators, Spectrometers, Detectors and Associated Equipment* 531.1 (2004), pp. 276–284.

[84] J Jakubek et al. "Neutron imaging with Medipix-2 chip and a coated sensor". In: *Nuclear Instruments and Methods in Physics Research Section A: Accelerators, Spectrometers, Detectors and Associated Equipment* 560.1 (2006), pp. 143–147.

[85] J Uher et al. "Characterization of 3D thermal neutron semiconductor detectors". In: *Nuclear Instruments and Methods in Physics Research Section A: Accelerators, Spectrometers, Detectors and Associated Equipment* 576.1 (2007), pp. 32–37.

[86] RA Muminov and LD Tsvang. "High-efficiency semiconductor theramal-neutron detectors". In: *Soviet Atomic Energy* 62.4 (1987), pp. 316–319.

[87] SL Bellinger et al. "Characteristics of the stacked microstructured solid state neutron detector". In: *SPIE Optical Engineering+ Applications*. International Society for Optics and Photonics. 2010, 78050N–78050N.

[88] SL Bellinger et al. "Enhanced variant designs and characteristics of the microstructured solid-state neutron detector". In: *Nuclear Instruments and Methods in Physics Research Section A: Accelerators, Spectrometers, Detectors and Associated Equipment* 652.1 (2011), pp. 387–391.

[89] Steven L Bellinger et al. "High-efficiency microstructured semiconductor neutron detectors that are arrayed, dual-integrated, and stacked". In: *Applied Radiation and Isotopes* 70.7 (2012), pp. 1121–1124.

[90] Ryan G Fronk et al. "High-efficiency microstructured semiconductor neutron detectors for direct 3 He replacement". In: *Nuclear Instruments and Methods in Physics Research Section A: Accelerators, Spectrometers, Detectors and Associated Equipment* 779 (2015), pp. 25–32.

[91] J Kenneth Shultis and Douglas S McGregor. "Efficiencies of coated and perforated semiconductor neutron detectors". In: *Nuclear Science Symposium Conference Record, 2004 IEEE*. Vol. 7. IEEE. 2004, pp. 4569–4574.

[92] Q Jahan et al. "Neutron dosimeters employing high-efficiency perforated semiconductor detectors". In: *Nuclear Instruments and Methods in Physics Research Section B: Beam Interactions with Materials and Atoms* 263.1 (2007), pp. 183–185.

[93] RJ Nikolić et al. "Roadmap for high efficiency solid-state neutron detectors". In: *Optoelectronic Devices: Physics, Fabrication, and Application II*. Vol. 6013. International Society for Optics and Photonics. 2005, p. 601305.

[94] Ryan G Fronk et al. "Dual-sided microstructured semiconductor neutron detectors (DSMSNDs)". In: *Nuclear Instruments and Methods in Physics Research Section A: Accelerators, Spectrometers, Detectors and Associated Equipment* 804 (2015), pp. 201–206.

[95] Daniel Moses. "Efficient scalable solid-state neutron detector". In: *Review of Scientific Instruments* 86.6 (2015), p. 065103.

[96] James E Turner. *Atoms, radiation, and radiation protection*. John Wiley & Sons, 2008.

[97] Richard T Kouzes et al. "Neutron detector gamma insensitivity criteria". In: *PNNL–18903, Pacific Northwest National Laboratory, Washington* (2009).

[98] Richard T Kouzes et al. "Neutron detection gamma ray sensitivity criteria". In: *Nuclear Instruments and Methods in Physics Research Section A: Accelerators, Spectrometers, Detectors and Associated Equipment* 654.1 (2011), pp. 412–416.

[99] Nicholas Metropolis and Stanislaw Ulam. "The monte carlo method". In: *Journal of the American statistical association* 44.247 (1949), pp. 335–341.

[100] Ivan Lux and László Koblinger. *Monte Carlo particle transport methods: neutron and photon calculations*. Vol. 102. CRC press Boca Raton, Florida, 1991.

[101] Judith F Briesmeister et al. "MCNPTM-A general Monte Carlo N-particle transport code". In: *Version 4C, LA-13709-M, Los Alamos National Laboratory* (2000), p. 2.

[102] Milan Tesinsky. "MCNPX Simulations for Neutron Cross Section Measurements". In: (2010).

[103] Sea Agostinelli et al. "Geant4—a simulation toolkit". In: *Nuclear instruments and methods in physics research section A: Accelerators, Spectrometers, Detectors and Associated Equipment* 506.3 (2003), pp. 250–303.

[104] J. Allison et al. "Geant4 developments and applications". In: *IEEE Transactions on Nuclear Science* 53.1 (Feb. 2006), pp. 270–278. ISSN: 0018-9499.

[105] Douglas S McGregor et al. "Semi-insulating bulk GaAs thermal neutron imaging arrays". In: *IEEE Transactions on Nuclear Science* 43.3 (1996), pp. 1357–1364.

[106] Samichi Srivastava, Rabinber Henry, and Anita Topka. "Characterization Of Pin Diode Silicon Radiation Detector". In: *Journal on Intelligent Electronic Systems* 1.1 (2007), p. 48.

[107] Nicholas Mascarenhas et al. "Directional Neutron Detectors For Use with 14 MeV Neutrons". In: (2005).

[108] Justin Peel et al. "Development of a directional scintillating fiber detector for 14MeV neutrons". In: *Nuclear Instruments and Methods in Physics Research Section A: Accelerators, Spectrometers, Detectors and Associated Equipment* 556.1 (2006), pp. 287–290.

[109] S Singkarat et al. "Development of an encapsulated scintillating fiber detector as a 14-MeV neutron sensor". In: *Nuclear Instruments and Methods in Physics Research Section A: Accelerators, Spectrometers, Detectors and Associated Equipment* 384.2 (1997), pp. 463–470.

[110] GA Wurden et al. "Scintillating-fiber 14 MeV neutron detector on TFTR during DT operation". In: *Review of scientific instruments* 66.1 (1995), pp. 901–903.

[111] Richard S Miller et al. "SONTRAC: An imaging spectrometer for MeV neutrons". In: *Nuclear Instruments and Methods in Physics Research Section A: Accelerators, Spectrometers, Detectors and Associated Equipment* 505.1 (2003), pp. 36–40.

[112] RT Klann, G Perret, and J Sanders. *Coated gallium arsenide neutron detectors: results of characterizationmeasurements.* Tech. rep. ANL, 2006.

[113] RL Schulte and M Kesselman. "Development of a portable directional thermal neutron detection system for nuclear monitoring". In: *Nuclear Instruments and Methods in Physics Research Section A: Accelerators, Spectrometers, Detectors and Associated Equipment* 422.1 (1999), pp. 852–857.

[114] Helmuth Spieler. *Semiconductor detector systems.* Vol. 12. Oxford university press, 2005.

[115] Hong Xiao. "Introduction to semiconductor manufacturing technology, 2001". In: *p515-516* 9 (2001).

[116] Dennis V Perepelitsa. "Johnson noise and shot noise". In: (2006).

[117] Gordon Gilmore. *Practical gamma-ray spectroscopy.* John Wiley & Sons, 2011.